OPTICAL NANOANTENNAS AS CAVITIES: NANOSCALE CONTROL OF COUPLING STRENGTH AND SINGLE PHOTON EMISSION

ANSHUMAN SINGH

ICFO - The Institute of Photonic Sciences
Universitat Politècnica de Catalunya

Castelldefels (Barcelona), Spain
November 2016

Thesis committee:

Prof. Dr. Femius Koenderink (FOM Institute AMOLF, The Netherlands)
Prof. Dr. Mario Agio (University of Siegen, Germany)
Prof. Dr. Javier G. de Abajo (ICFO - The Institute of Photonic Sciences)

OPTICAL NANOANTENNAS AS CAVITIES: NANOSCALE CONTROL OF COUPLING STRENGTH AND SINGLE PHOTON EMISSION

ANSHUMAN SINGH

under the supervision of

Prof. Dr. Niek F. van Hulst

submitted this thesis in partial fulfillment

of the requirements for the degree of

Doctor

by the

Universitat Politècnica de Catalunya

Castelldefels (Barcelona), Spain
November 2016

Dedicated to

My family.

ABSTRACT

Optical nanoantennas confine light on the nanoscale, enabling strong light-matter interactions with potential for ultra-compact optical devices. Apart from the direct applications in optical nanoscopy and sensing, nanoantennas can strongly enhance the spontaneous emission rate of single photon emitters. A nanoantenna, acting as a nanocavity, enables high photon output due to its high radiative losses associated with plasmonic resonances and thus pave the way for compact, bright, and pure single photon sources with applications in quantum technologies. The sub-wavelength field localization at the nanoantenna causes a vectorial field distribution with non-zero field components in all dimensions. The efficiency of coupling between an emitter such as single molecule and nanoantenna will thus strongly depend on the spatial overlap of the emitter's dipole with the nanoantenna field. In order to achieve such coupling, careful nanopositioning of the emitter, in its location as well as the orientation, within the nanocavity field is required. Therefore, the full vectorial characterization of the emitter-nanoantenna is crucial to maximize the coupling strength. This thesis addresses the aforementioned issues and studies the controlled nanoscale interaction of a single molecule with a resonant nanoantenna.

To this end we first fabricate nanoantennas on the vertex of a fiber tip using focused-ion-beam milling and use a near-field technique for the nanopositioning control. In the first experiment, we investigate the excitation properties of a resonant dipole nanoantenna by mapping its vectorial near-field distribution with molecular resolution. The nanoantenna tip is scanned over specifically selected single molecules to map x-, y-, and z-field components. In addition to characterization of the vectorial field, we show the apparent position of the molecule shifts up to 20 nm depending on their orientation with important implications for localization microscopy.

Next, our unprecedented experimental approach allows us to examine an often overlooked, but important near-field concept of nanoantennas, local interference. The highly structured vectorial amplitude and phase distribution of the nanoantenna overlaps with the exciting far-field to create this local interference. We perform a detailed study through direct observation and show an example of exploiting this local interference to shape and control the near-field of the nanoantenna.

Lastly, we quantify the vectorial interaction of a molecule-nanoantenna cavity system by mapping the coupling strength g with 5 nm spatial resolution. We show that for a molecule's optimal position at the nanoantenna, the coupling rate reaches up to g_{max} = 206 GHz, much higher than for any conventional cavities. Such a large coupling provides ideal conditions for fast and pure non-classical photon emission, enabling a single photon source with an emission rate above 1 GHz at room-temperature.

CONTENTS

1 INTRODUCTION

Optical cavities enhance light-matter interaction either by storing or confining optical fields. Optical nanoantennas strongly confine light and thus act as nanocavities with sub-wavelength mode volumes. This thesis explores the interaction of optical nanoantennas as nanocavities with single photon emitters and how to tune this interaction to produce pure, triggered, and ultrafast single photon sources. Here, we fully characterize nanoantenna cavities and quantify its interaction with a single photon emitter on the nanoscale. We perform both qualitative and quantitative study of the near-field properties including excitation enhancement and coupling strength of the resonant nanoantenna using single fluorescent molecules as nanometer sized probes.

In this introduction, we first discuss single photon sources and their applications. We then briefly discuss optical cavities and their role in the modification of the spontaneous emission of single photon emitters. Next, we introduce the concept of nanocavities in the context of optical nanoantennas and discuss their advantages over traditional microcavities. We then introduce the vectorial near-field of a nanoantenna and its importance in realizing applications. Lastly, we discuss nanoscale position and orientation control of an emitter relative to a nanoantenna and its effect on the interaction.

1.1 SINGLE PHOTON SOURCES

Photons are the fundamental particle of light with unique properties such as zero rest mass, no charge, and finite electromagnetic energy at a fixed frequency. These characteristics enable photons a key role as information carrier in quantum technologies. Single photons are relatively free of noise and quantum information can be easily encoded in several degrees of freedom such as polarization, wavelength, timing, and path. The specific significance of single photons lies in all optical computing, particularly since the feasibility of nondeterminstic interactions in simple linear optical circuits, using single photon sources and detectors, was recognized [1]. Moreover, such sources and detectors are scalable for integration into larger scale circuits. Thus, there is a strong motivation to develop compact and efficient single photon sources with applications in quantum information process-

ing, quantum cryptography, detection of weak signals through squeezing of light, and quantum frequency conversion [2–6]. For these schemes to be effective, the single photon source should be rather ideal: triggered, pure, emit into a spatio-temporal mode, frequency-bandwidth limited and especially with a high repetition rate.

In the past, weak laser pulses with very low average photon number n have been used to obtain single photons [7]. However, the probability to obtain pulses with no photons is very high at small n values, which severely affects the bit rate of the source. Spontaneous parametric down-conversion (SPDC) is another widely used technique to create single photon states [8]. In SPDC, the photon pairs are generated by the nonlinear interaction of an intense pump laser with a non-centrosymmetric crystal, where a high frequency photon converts into two lower frequency photons. This is an improbable process, and thus require a very high pump power to generate photon pairs, which limits the single photon generation at specific time. Moreover, there may be multiple photons created at a given time, which is not ideal for applications such as quantum cryptography.

An ideal single photon source is a device which emits only one photon at a time when triggered i.e. producing single photons on demand. A two level quantum system, upon excitation, spontaneously emits a single photon from the first excited electronic state to the ground state, and thus perfectly qualifies as a pure single photon source. Over the years, a variety of single photon emitters such as semiconductor quantum dots [9], organic molecules [2], atoms [10], and nitrogen vacancies in diamond [11] have been explored for use in single photon sources and thoroughly investigated [4]. These emitters are nanosized objects with weak oscillator strength and interact poorly with optical fields, and therefore do not efficiently absorb nor emit photons. Techniques are required to increase the absorption cross-section to efficiently excite emitters together with enhancing and controlling the spontaneous emission of the photon emitters to facilitate their use in applications.

1.2 OPTICAL NANOANTENNA: A NANOCAVITY

The spontaneous emission rate is not an intrinsic property of an emitter but depends on the environment in which it's placed. The effect was first identified by E. M. Purcell for magnetic transitions at radio frequencies in an electrical resonator [12]. He showed that the rate of the transition i.e. the spontaneous emission rate could be enhanced compared to the free-space

rate. The enhancement in the spontaneous emission rate is known as Purcell factor and given by:

$$F_p = \frac{3\lambda_f^3}{4\pi^2}\frac{Q}{V_m}, \tag{1.1}$$

where λ_f is the transition wavelength, Q is quality factor of the resonator, and V_m is the volume. At optical frequencies, Goy *et al.* were first to demonstrate the spontaneous emission enhancement of Na-atoms in a high Q Fabry-Perot type microcavity at cryogenic temperatures [13]. This exploration led to an entire new field of research in quantum optics known as cavity quantum electrodynamics (cavity QED) [14]. The quality factor Q of a cavity is an important figure of merit, which is a measure of the storage time of a photon in the cavity. The ability of microcavities to keep light confined for long times results in very high Q values (see Figure 1.1a). Traditionally microcavities [15] based on Fabry-Perot or whispering gallery modes have focused on achieving high Q to boost emitter-cavity interaction quantified in the coupling strength g [16]. The coupling strength corresponds to the rate of energy transfer between an emitter with dipole moment $\mathbf{p}$ and a cavity with field $\mathbf{E}_s$, and is defined as:

$$g = -\frac{\mathbf{p}.\mathbf{E}_s(\omega_f, \mathbf{r})}{\hbar}, \tag{1.2}$$

where ω_f is the emission frequency of the emitter and $\mathbf{r}$ is the position of the emitter in the cavity. A cavity with high Q can produce a large coupling strength, and thus enhance the spontaneous emission rate of the emitter (Equation 1.1). However, the high Q cavities slow down the photon emission rate and pose limitations on the brightness (no. of photons/sec) of a single photon source. To achieve high Q values and minimize thermal losses, microcavities are generally operated at low temperatures [17]. As a result, microcavities are extremely spectral sensitive, which imposes stringent restrictions on the emitter selection and makes them susceptible to external conditions such as vibrations and temperature drift [18].

Another solution for obtaining the large coupling strengths g and still maintaining high photon throughput, is to use cavities with very small mode volume V_m combined with low Q. Evident from Equation 1.1, the spontaneous emission rate can be enhanced by reducing V_m, which in turn increases the field density, resulting the large coupling strength (Equation 1.2). Thus, to preserve high photon output and rapid response it is advantageous to strive for highly localized EM fields in lossy nanocavities.

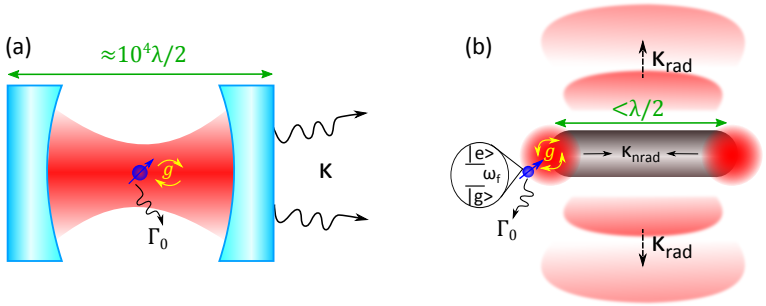

Figure 1.1: Comparison of cavities. (a) A Fabry-Perot microcavity formed using two highly reflecting mirrors. The microcavity exhibits high quality factor Q due to low cavity emission losses κ, therefore it can store photons for long time. Conversely, (b) a nanocavity such as a metallic optical nanoantenna has low Q values mainly due to high radiation losses κ_{rad} and small ohmic losses κ_{nrad}. The high radiative losses results in ultrafast photon emission from the nanocavity. In addition, the nanoantenna has a mode volume well below the diffraction limit, and thus is able to attain large coupling strengths g between a single photon emitter such as single molecule (in blue) and a electromagnetic mode of the nanoantenna. The large coupling strength enables a strong enhancement of the free-space spontaneous emission rate (Γ_0) of a molecule coupled to the nanoantenna cavity. The physical size of the nanoantenna can be smaller than $\lambda/2$, ideal for the chip based single photon sources.

Optical metallic nanoantennas are ideal candidates for such types of nanocavity (see Figure 1.1b), combining low quality factors with deeply localized mode volumes [19], while still displaying large g, provided the emitter is positioned correctly withing the nanoscale mode volume [20]. Moreover, the physical size of a nanoantenna can be smaller than $\lambda/2$, making nanoantennas very useful for the chip based single photon sources at room temperature. Thus, nanoantennas present a unique alternative for cavity QED combining strong coupling with bad cavities and ultrafast photon response [18, 21, 22].

However, there are certain crucial requirements which need to be addressed to realize single photon sources based on nanoantenna cavities. These requirements can be divided into three broad categories: (1) Fabrication of resonant nanoantennas with characteristic lengths <200 nm. (2) Full knowledge of the local near-field distribution inside the mode volume i.e. imaging of the nanoantenna mode patterns. (3) Nanoscale position and orientation control of a single emitter within the mode volume to find the position of an optimum coupling for the emitter into a nanoantenna mode. This can be achieved through mapping of the coupling strength g between single photon emitter and resonant nanoantenna with nanometer precision. The nanopositioning is crucial as the fluorescence enhancement of the emitter can be quenched in the close proximity of the nanoantenna, and thus can increase the non-radiative rate [23–25].

The aim of this thesis is to treat each of these issues separately and perform a full characterization of a single photon emitter-nanoantenna cavity system. We use single fluorescent molecules as single photon emitters which act as local probes to study the nanoantenna. Single molecules are attractive due to their dipolar character, ~1 nm size, and ability to operate at room-temperature [26]. These properties give molecules an edge over other single photon emitters such as atoms, which require low temperature conditions and quantum dots which are relatively big and lack dipolar character.

1.3 OPTICAL NANOANTENNA: LOCAL FIELD DISTRIBUTION

Radio wave antennas have transformed the way we communicate information and play a pivotal role in modern telecommunication devices [27]. Optical waves have frequencies six orders of magnitude higher than radio waves and consequently have much shorter wavelengths; therefore antennas at optical frequencies need to be far smaller than their radio equivalents [28]. Important developments in nanofabrication have brought the ability to shape materials to the nanoscale range required for these antennas. This allows the creation of devices that confine freely propagating light to nanoscale structures known as optical (nano)antennas [29–31].

An optical nanoantenna, a metallic nanostructure, acts as a transducer, which reversibly and efficiently converts free propagating optical radiation into localized energy. The manifestation of a resonant electromagnetic (EM) mode in the metal, known as a localized surface plasmons, facilitate this energy conversion [32]. The ability of nanoantennas to strongly confined, and scatter incident EM radiation has enabled a wide variety of applications. The field localization at sub-wavelength volumes at the nanoantenna has a direct application in super-resolution microscopy [33–39]. In addition to high resolution imaging, nanoantennas provide high optical throughput. This allows them to used in applications such as to enhance weak Raman scattering [40–42] and nonlinear processes [43–45]. Other applications include use of nanoantennas in efficient photodetectors [46], spectroscopy [47, 48], and bio-sensing and-imaging [49–51].

A nanoantenna upon far-field excitation confines or focuses light at sub-wavelength volumes inside which EM field becomes highly structured. The field has a 3D structure in space with highly position dependent strength i.e. a vectorial field distribution. Due to this vectorial field nature, the positioning of a single photon emitter such as a molecule close to the nanoantenna becomes critical to achieve optimum coupling (see Equation 1.2). Similarly, the interaction efficiency for the excitation rate strongly depends on the

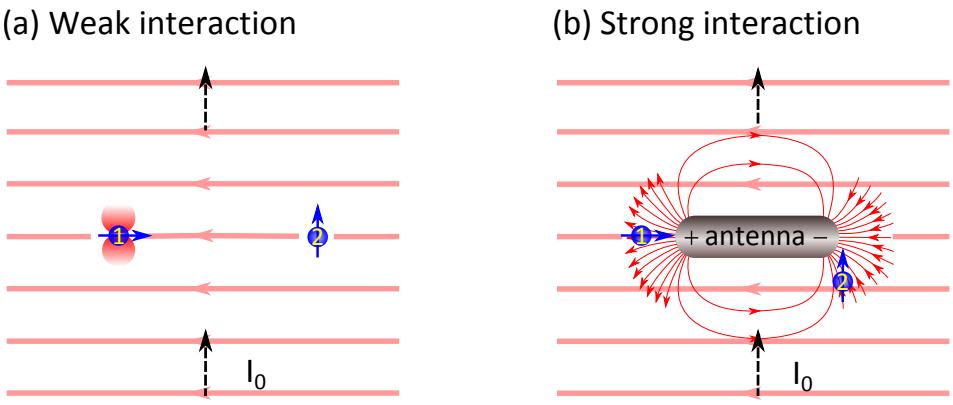

Figure 1.2: Nanoantenna mediated strong light-matter interaction. (a) Two orthogonally oriented molecules (1 and 2) in a linearly polarized optical field with intensity I_0, which weakly excites the molecule 1. However, the molecule 2 does not interact at all due to its orientation relative to the incident field polarization. (b) A nanoantenna has a vectorial field distribution, which can excite both the molecules given that they are at the right positions at the nanoantenna. Dashed arrows represent the direction of the propagating plane wave.

overlap of the molecule's absorption dipole moment with the interacting optical field. Under the dipole approximation, the excitation rate (Γ_{exc}) is directly proportional to the square of the exciting electric field along the direction of the molecule's absorption dipole moment **p** as:

$$\Gamma_{exc} \propto |\mathbf{p}.\mathrm{E}(\omega_0, \mathbf{r})|^2, \tag{1.3}$$

where ω_0 is the excitation frequency and **r** is the position of the molecule in space. As previously mentioned, molecules interact weakly with optical fields and this interaction can further reduce if the molecule is not perfectly oriented relative to the polarization of the excitation light. The vectorial field of the nanoantenna can circumvent this problem by allowing the efficient excitation of all molecule orientations given they are positioned correctly at the nanoantenna. Figure 1.2a shows two orthogonally oriented molecules (1 and 2) in a linearly polarized plane wave (incident) field. Only the molecule 1 can interact with the incident field while the molecule 2 is not excited as it is oriented perpendicular to the incident field polarization. The rod shaped nanoantenna behaves like an oscillating dipole that coherently scatters the incident radiation. At a fixed time, charge distribution and field lines illustrate the dipole character, as shown in Figure 1.2b. This vectorial arrangement of the field lines permits excitation of both the molecules.

A molecule only absorbs a fraction of the illuminated light, leading to its excitation (see Figure 1.2). This fraction usually quantified using the absorption cross-section, corresponding to an effective area (m^2) of the

molecule absorbing a flux of photons from the illumination intensity (photons $m^{-2}s^{-1}$). The absorption cross-section σ_{abs} of the molecule is defined as [52]:

$$\sigma_{abs} = \frac{\Gamma_{exc}}{I_0}. \tag{1.4}$$

In addition to the vectorial field distribution, the local enhancement brought by the nanoantenna can strongly increase the excitation rate of the molecule. Thus, the molecule sitting in close vicinity of the nanoantenna shows an effective absorption cross-section that is increased compare to free-space case (Equation 1.4), resulting in an enhanced light-matter interaction and more efficient system.

In conclusion, to fully exploit the field localization ability and attain high coupling rate require an accurate positioning of an emitter at the nanoantenna. Such confined localization of light has non-zero field components in all three directions (x, y, and z), making the coupling strength sensitive to the orientation of the emitter relative to the nanoantenna.

1.4 NANOPOSITIONING CONTROL: A MOLECULE -NANOANTENNA SYSTEM

The characteristic length of a nanoantenna is <200 nm and the field localizes at even smaller length-scales [19]. Thus, careful positioning of an emitter with nanometer accuracy is needed to fully exploit the near-field properties of the nanoantenna. Conventionally, arrays of nanoantennas are fabricated on a planar substrate, which allows us to systematically study the length and width dependent resonances [44, 53, 54]. In a direct approach, molecules are randomly drop-casted on the nanoantennas array, thus a little or no control over the molecule's position, orientation, and number of molecules at the nanoantenna [55–57]. Several lithography techniques have been explored to gain further control over emitter's position at the nanoantenna, however reproducibility is still an issue with these techniques [58, 59]. In addition, once fabricated the position of the emitter is fixed on the nanoantenna and can not be changed. Using these techniques, various nanoantenna designs and their interaction with single emitters have been investigated. Geometries such as a simple nanorod, two nanorods accompanied by a nanogap, bow-tie shaped, a nanogap between nanocubes and a metal film have been demonstrated [55, 57, 60, 61]. Despite achieving large excitation and emission enhancements, the lack of position and orientation

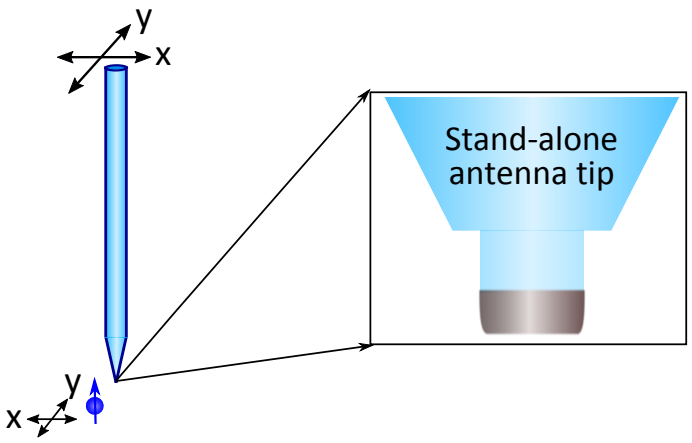

Figure 1.3: Single molecule-single nanoantenna system. A fiber tip with a nanoantenna can be placed in the close vicinity of a single molecule using a near-field technique. The nanoantenna sits at the apex of an optical fiber as a stand-alone structure and can locally access the molecule with nanometer position accuracy.

control of molecules prevent access to the full control over the coupling strength.

Scanning nanoantenna tips with the near-field microscope approach circumvent the positioning issues and provide full position control on the nanoscale [62]. The nanoantenna is fabricated directly at the apex of a glass fiber that can be positioned over an emitter with nanometer accuracy (see Figure 1.3). Plasmonic nanospheres attached to scanning tips have been applied to investigate distance dependent excitation and emission rate for a specific molecule orientation [23, 63]. A monopole antenna at the end of an aperture tip has been shown to produce polarization controlled emission of single molecules [64]. Although the scanning tip method poses fabrication challenge and relies on sophisticated near-field techniques, it provides unprecedented position control and by far the best technique to study nanoscale light-matter interaction in the controlled way [65]. In a reverse approach, an emitter can also be attached to a sharp tip and positioned over the nanoantenna, however rapid bleaching of the emitter becomes an issue [66, 67].

In the experiments shown in thesis, we use the scanning tip approach, where the apex of an optical fiber holds a nanoantenna, see Figure 1.3. The nanoantenna is an isolated and stand-alone construction, which can be brought within few nanometers of a molecule using a near-field technique. By scanning either the tip or the molecule, we can achieve the full position and orientation control on the nanoscale. We choose a nanorod shaped antenna in our experiments to study the near-field interaction with a molecule. The nanorod is the simplest antenna geometry, mimicking a

Herzitan dipole. Moreover, the asymmetric shape of the nanorod antenna is an advantage as its preferential direction of excitation and emission gives an extra criterion to study the interaction.

1.5 THESIS ORGANIZATION

In addition to this introduction, the thesis has four key chapters and is organized as follow:

Chapter 2

Fabrication has a very important role in the development of this work. Chapter 2 discusses the techniques, procedures, and steps involved in the fabrication with images of various fabricated nanoantennas. We briefly discuss the design strategy for nanoantennas, which is an important step before fabrication and provides information about the nanoantenna resonance depending on its shape and size. Lastly, we elaborate the experimental setup used for the nanoscale positioning and orientation control of single emitters relative to single nanoantenna, and to study the interaction between the two.

Chapter 3

This chapter focuses on the vectorial near-field mapping of nanoantennas. We use single molecules with specific orientations as local probes to measure the vectorial field components of a resonant dipole nanoantenna mode. This allows us to quantify the strength of the field components and map their spatial distribution with nanometer resolution. We discuss the orientation dependent shifting of molecule's position at the nanoantenna. We use polarization resolved measurements to show the emission control of single molecules by the nanoantenna.

Chapter 4

This chapter discusses an important effect of interference in the near-field of a nanoantenna. We present a direct observation of the local interference and discuss in detail the factors contributing to this local effect. The vectorial nature of the nanoantenna field allows us to shape and control the near-field distribution around the nanoantenna. We exploit the local interference

to demonstrate the polarization-controlled shifting of the hotspot positions at the nanoantenna.

Chapter 5

This chapter concentrates on the emission properties of a molecule coupled to a resonant nanoantenna. We model nanoantenna as nanocavities and explore their use in cavity QED. We quantify the interaction between the molecule and nanocavity by mapping the coupling strength g with 5 nm resolution. We show the nanopositioning control by deterministically placing the molecule at the nanoantenna to enhance the spontaneous emission rate, essential for realizing super-bright and pure single photon sources.

2

NANOANTENNAS FABRICATION AND EXPERIMENTAL METHODS

In the experiments described in this thesis we study controlled interactions between resonant nanoantennas and individual fluorescent emitters. This involves a combination of experimental and computational techniques. Experimentally, this requires fabrication of nanoantennas in a reproducible way. Once fabricated, the nanoantennas have to be placed in the close vicinity of an emitter with full control of the relative distance with nanometer precision. An optical microscope is then used to observe the emitter-nanoantenna interaction using various types of detection. We perform numerical simulations to obtain the correct nanoantenna dimensions for a given geometry and to verify the experimental findings. In this chapter, firstly we describe in detail the steps involved in the fabrication process for different nanoantenna designs followed by a description of the numerical calculations. After briefly mentioning the preparation of the sample containing the emitters, we elaborate on the experimental setup and the different measurement techniques used to study the molecule-nanoantenna interaction.

2.1 FABRICATION OF NANOANTENNAS

For all the experiments presented in this thesis, we use rod shaped nanoantennas fabricated at the tip of an optical fiber. As discussed in Chapter 1, a nanoantenna at the fiber tip gives us the unique possibility of studing an isolated single emitter-nanoantenna system on the nanoscale using the near-field technique.

2.1.1 *A Dipole nanoantenna*

A dipole antenna is the simplest and one of the first types of radio antenna, invented by H. Hertz., therefore also known as a Hertzian dipole. The dipole antenna is a metal wire or rod which upon excitation produces a two-lobed radiation pattern and has a length exactly equal to half of the wavelength ($\lambda/2$) at resonance. A similar concept can also be applied at optical frequencies, where a metal nanorod of a fixed length can behave as a

dipole nanoantenna when appropriately excited [32]. However, the length of the dipole nanoantenna is shorter than $\lambda/2$ due to modified metal properties at optical frequencies [28]. Plasmon resonances, a collective motion of electrons in metals coupled to light, allow the dipole nanoantenna to confine light at two ends known as hotspots [29, 68].

All the measurements shown in this thesis are performed on aluminum nanorod (dipole) antennas. The nanorod antenna is a simple planar geometry and can be easily adapted for any wavelength by simply changing the length of the nanorod. In comparison to the nanosphere, the nanorod has a preferential axis, which allows selective excitation and introduces an extra parameter (e.g. polarization) to investigate the nanoantenna's interaction with an emitter.

We choose aluminum in our experiments due to its superior plasmonic properties within the visible spectrum [44, 69]. Aluminum is a more perfect conductor (more negative permittivity) as compared to other noble materials such as gold and silver. Aluminum has the shortest skin depth in the optical regime, which is superior for localizing optical fields. In addition, aluminum rapidly forms a thin (2-3 nm) layer of oxide on its surface that protects the underlying metal from further oxidation [70].

2.1.2 *Fabrication technique*

For the nanoantenna fabrication, we use a Zeiss-AURIGA cross-beam focused ion beam (FIB) milling machine. The FIB system applies a strongly focused beam of gallium ions onto a sample to mill the structure with nanometer precision [71]. The ions in the beam are accelerated in an electric field of 30 KeV, which allows them to hit the sample surface with very high momentum, resulting in efficient removal of atoms from the surface. The beam diameter, and, hence spatial resolution, can be adjusted by changing the beam current. The current has a nonlinear relation with the beam diameter and varies from 2 pA (7 nm) to 20 nA (1100 nm). The FIB system employs a separate electron source to simultaneously image the milling process. A lithography software called nano pattering visualization engine (NPVE) is incorporated into the FIB system, which permits the design and fabrication of arbitrary nanostructures. Additionally, the fabricated nanostructures can be imaged using three different detectors, which provide information about different materials and topography of the structure.

An optical fiber with outer diameter of 125 µm is almost three orders of magnitude bigger than a nanoantenna of typical length of <200 nm. Therefore, firstly, the fiber is tapered by heat pulling using a micropipette puller

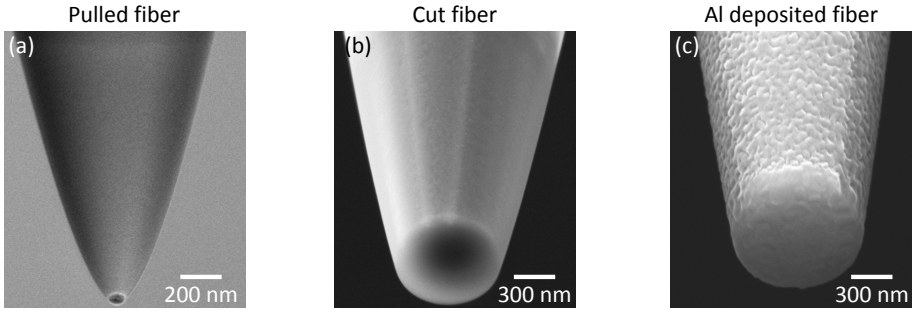

Figure 2.1: Scanning electron microscope images of the three phases of the fiber in preparation for a nanoantenna tip. (a) A heat pulled fiber with tapered end with typical diameter of <100 nm. (b) The tapered end of the fiber is cut using the FIB to make a regular flat base for the nanoantenna fabrication. (c) The end face is coated with a thin layer (50-60 nm) of metal (aluminum) using thermal deposition.

(Sutter P2000) to bring its diameter down to <100 nm. Next, the tapered end is cut flat using FIB to prepare a base for the nanoantenna with typical diameter between 300-500 nm. Afterwards, the end face of the fiber is coated with a thin adhesion layer of Titanium (3 nm) followed by a coating of 50-60 nm of the metal of interest. Figure 2.1a-c show scanning electron microscope (SEM) images of the fiber in the three aforementioned steps involved in the preparation of the nanoantenna tip.

The nanoantenna is subsequently milled into the metal film of the tip using FIB. The milling process is illustrated in Figure 2.2a, which depicts a top view of the metal coated fiber where the inner circle represents the tapered end. Using NPVE software, we construct a nanorod shape on the fiber end by combining four rectangles (in green) as shown in Figure 2.2a. The direction of milling for each rectangle, indicated by arrows in Figure 2.2a, is selected in such a way that it mills towards the structure to minimize redeposition of the milled material onto the nanoantenna. Figure 2.2b shows the nanorod shaped antenna sitting at the fiber apex after the milling procedure. Before fabricating the nanoantenna on the fiber tip, several calibrations are performed on a metal coated cover-slip of the same material and thickness. This is required to find the correct geometry and dose (amount of charge per unit area) of ions in the beam at a given beam current to obtain the desired length and width of the nanoantenna. Most of the nanoantennas used in this thesis are fabricated at a 2 pA beam current (7 nm beam diameter) using these milling parameters: [Dose = 0.106 nC/μm^2, Dwell time = 650 μs, Repeat = 1], where Dwell time is the time per pixel, and Repeat defines the number of times the beam is scanned over the rectangle.

Figure 2.2c,d show two examples of aluminum (Al) and gold (Au) nanorod shaped (dipole) antennas fabricated on the apex of a tip. A clear contrast

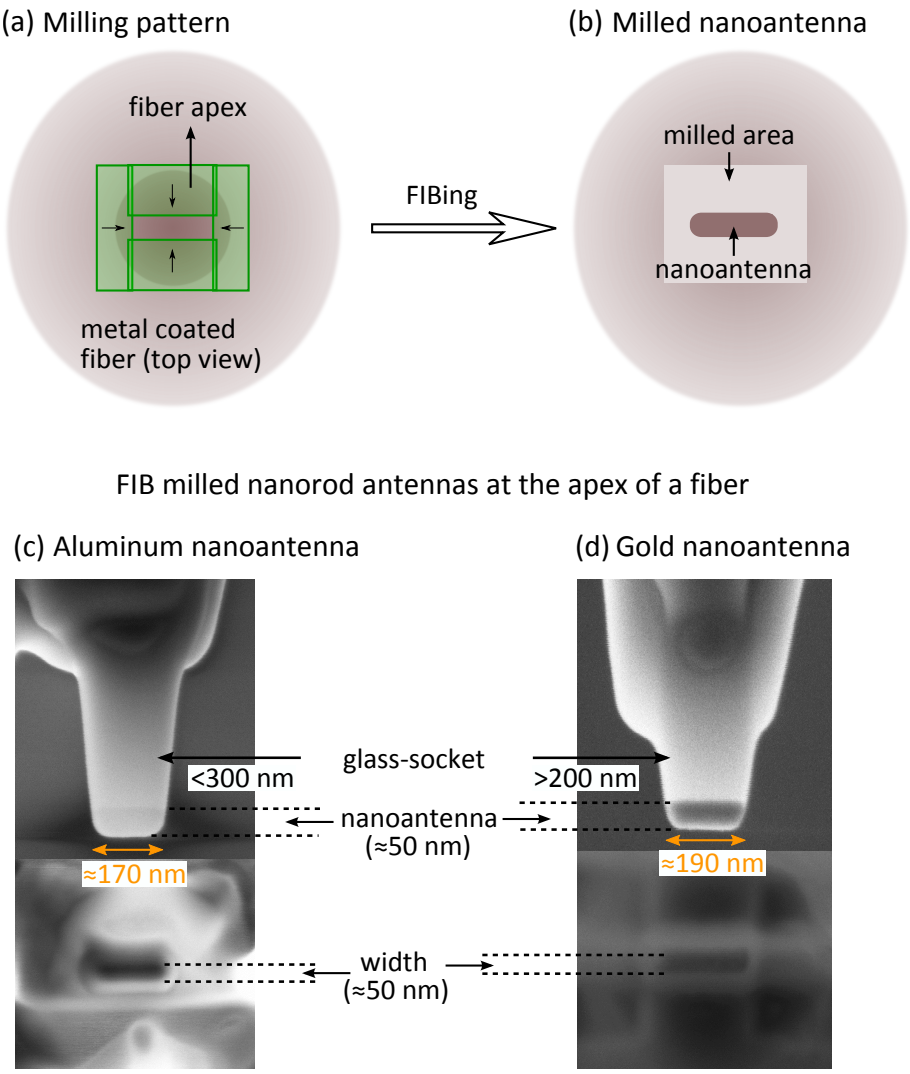

Figure 2.2: Milling technique and fabricated nanoantennas (a) A schematic showing the top view of a metal coated fiber with the inner circle representing the apex of the fiber. A rectangular geometry is used and placed around the coated fiber such that it removes the metal from all the directions, which results in the shape of a nanorod. (b) Fiber after the milling process, where the remaining metal forms a nanorod shape. SEM images (both side and top view) of the FIB milled (c) Aluminum nanoantenna, length=170 nm, width=50 nm, height=50 nm, and (d) Gold nanoantenna, length=190 nm, width=50 nm, height=50 nm. The nanoantenna is sitting at the end of a glass-socket (200-300 nm long), which prevents unwanted interactions between the rest of the tip and investigated emitter.

between the gold film and glass can be seen (Figure 2.2d) due to the larger mismatch in their refractive index than in the case of aluminum and glass, where the contrast is low (Figure 2.2c). In both cases, the nanoantenna is a free standing structure positioned on top of a glass-socket of nearly 200-300 nm length (see Figure 2.2c,d). The glass-socket is a by-product of the FIB milling as the ion beam mill through the fiber (glass), leaving the nanoan-

tenna as a stand-alone structure. This is an advantage as the glass-socket decouples the nanoantenna from the rest of the coated fiber. In this way, when the nanoantenna tip is brought close to an emitter (e.g. a molecule), we only need to consider the interaction between the nanoantenna and molecule, without taking into account the role of the tip. Thus, the proximity of the nanoantenna can be clearly observed and easily interpreted. Moreover, this stand-alone nanoantenna can be directly excited with far-field laser radiation without the need of other excitation mechanisms such as guiding light through the fiber [72, 73].

2.1.3 *Fabrication of other nanoantenna designs*

Similar to radio antennas, different designs of optical nanoantennas are possible, that address specific applications. Examples of different designs that have been theoretically proposed and some fabricated on a planar substrate include: (i) A nanogap antenna, where two nanorods are accompanied by a small gap. The nanogap antennas can further enhance the local field at the gap position and are useful for applications such as local nonlinear processes and Raman enhancement [29, 43, 74]. (ii) A split-ring-resonator for directional light emission and enhancing magnetic transitions [75, 76]. (iii) L-shaped structures, which give a single hotspot while retaining nanoantenna resonances in a separate plane, useful for high-resolution imaging and also display unique non-linear properties [77].

Fabricating these nanostructures at the end of fiber tips would enormously enhance the level of control of single emitters, however this poses fabrication challenges and tests the current limits of nanofabrication. We succeeded in the fabrication of some of these nanostructures and performed some preliminary measurements. These investigations, however are not part of this thesis. SEM images of gap, SRR and L-shaped nanoantennas fabricated on a fiber tip are shown in Figure 2.3.

2.2 METHOD FOR DESIGNING NANOANTENNAS

As we discussed (in Chapter 1), a nanoantenna can enhance both the excitation and emission rate of an emitter coupled to it. Since in general, maximum of the emission wavelength is Stokes shifted with respect to the excitation (absorption) maximum of a fluorescent emitter e.g for a single molecule, the nanoantenna resonance can be tuned to be resonant with either the excitation or emission wavelength. In order to find the correct dimensions of a specific nanoantenna design for a desired resonance condition, we per-

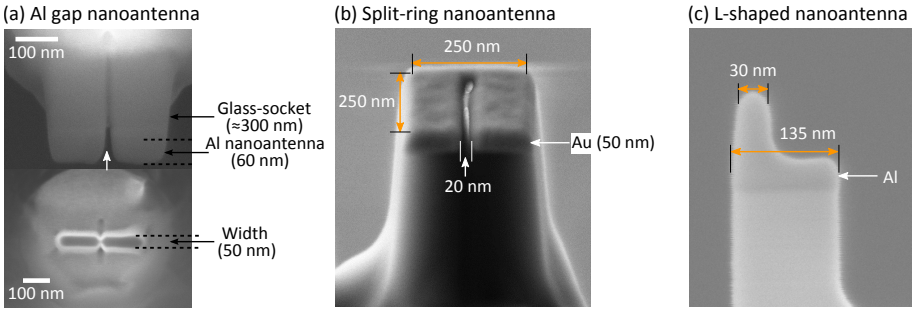

Figure 2.3: Other nanoantenna designs. SEM images of FIB milled nanoantennas at the apex of a fiber tip. (a) A gap nanoantenna milled on Al (60 nm). (b) A split-ring-resonator nanoantenna milled on 50 nm Au. (c) An L-shaped Al nanoantenna.

form finite-difference time-domain (FDTD) simulations using a FDTD tool, Lumerical. This method of designing nanoantennas has previously been verified experimentally in our group [78].

The FDTD simulation is performed such that the designed nanoantenna and simulation area closely represents the fabricated nanoantenna and experimental conditions, respectively. The schematic of a simulation scheme for designing a resonance dipole nanoantenna is shown in Figure 2.4a. The simulated area contains the Al nanoantenna at the end of a glass-socket connected to the fiber tip (glass). We include a thin (3 nm) adhesion layer of titanium between the nanoantenna and the glass-socket. A piece of glass representing the molecule sample (a cover-slip) is placed 10 nm below the nanoantenna. A 2D monitor that records the near-field of the nanoantenna in the xy-plane is positioned 15 nm below the nanoantenna inside the glass sample, which is the approximate position of a molecule on the cover-slip in the experiment. Other monitor types (for example an xz-plane monitor) can also be used.

An incident field, polarized along the x-axis and propagating along the z-axis, excites the nanoantenna from below. The incident field has unity magnitude, thus the field recorded by the monitor directly gives the enhancement of the nanoantenna (Figure 2.4a). Since the monitor is below the incident field source, it records a superposition of both the scattered field of the nanoantenna and the incident field, similarly to a molecule is a real experiment. In the simulation, we can separately calculate only the contribution of the scattered field by adopting the design shown in Figure 2.4b, where the source is moved above the monitor. This configuration will later be used in Chapter 4 for describing the interference effect in the near-field of the nanoantenna

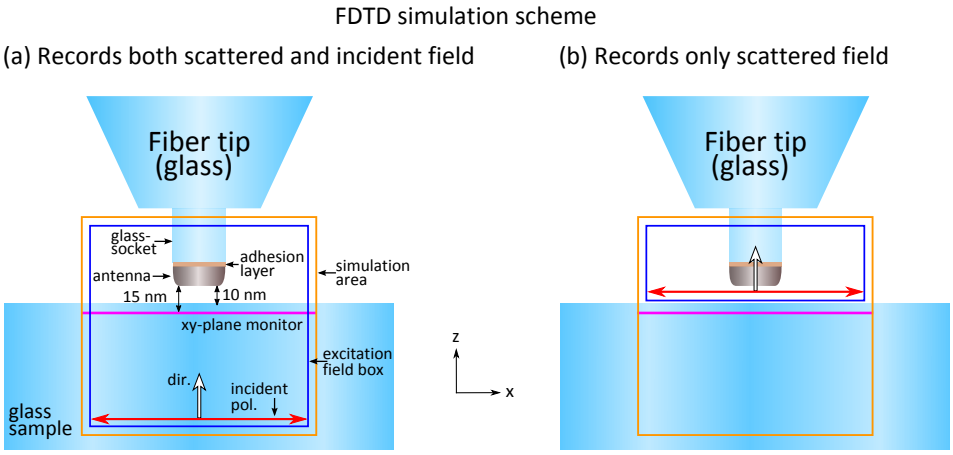

Figure 2.4: A FDTD simulation scheme for designing nanoantennas. (a) The simulation area contains a nanoantenna scanning tip and a glass sample 10 nm from the nanoantenna. A linearly polarized incident field propagating along the z-axis excites the nanoantenna and the scattered field is collected by a monitor placed 15 nm below the nanoantenna. In this configuration, the monitor records a superposition of the scattered and incident field. This configuration is similar to our experimental scheme, where a molecule is excited by the resultant field. (b) The incident field is moved above the monitor such that it excites only the nanoantenna. Thus, we obtain only the scattered field of the nanoantenna directly at the monitor.

Resonance condition

The simulations show that the first-order dipole mode of an Al nanoantenna with length=170 nm, width=60 nm, height=60 nm has a broad resonance (spectral width>100 nm) with a maximum around 647 nm. We use these dimensions in Chapter 3 when probing the excitation enhancement and vectorial field property of a dipole nanoantenna. In Chapter 5, the resonance of the dipole antenna is tuned to the emission wavelength of single molecules ($\approx$ 680 nm). In this case, the resonant dimension for the first-order mode of an Al nanoantenna is found to be length=180 nm, width=50 nm, height=50 nm. However, on fabrication the actual dimensions and sharpness of nanoantennas slightly differ from the calculated ones, mainly due to FIB processing.

2.3 FLUORESCENT EMITTERS

We use two different types of fluorescent emitters according to the specific nanoantenna interaction we want to study. In the experiments, we use single fluorescent molecules and polystyrene fluorescent nanobeads. For our experiments, we have extensively used terrylene diimide (TDI) molecules due to their high quantum efficiency ($\sim$ 90%) and good photostability [79,

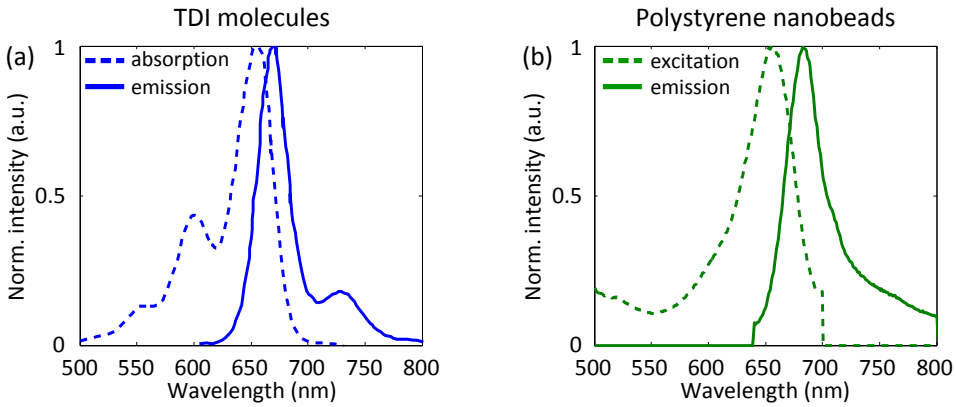

Figure 2.5: Spectra of molecules and nanobeads. (a) Absorption (dashed line) and emission (solid line) spectra of TDI molecules. (b) Excitation (dashed line) and emission (solid line) spectra of polystyrene nanobeads.

80]. The TDI molecules have an emission peak around 680 nm whereas the excitation spectrum has a maximum around 650 nm in toluene solution (see Figure 2.5a) [79]. For the experiments, we prepare a solution with 10^{-8} M concentration of molecules in 1% w/w of poly methyl methacrylate (PMMA) in toluene. A 70 µL of the solution is spin-coated on a cleaned glass cover-slip to obtain single molecules dispersed in a ≈20 nm thin layer of PMMA.

A fluorescent nanobead is a polystyrene sphere of diameter around 20 nm (Invitrogen FluoSpheres 8783) containing a few hundred single fluorophores. The excitation and emission wavelength peaks of the nanobeads we used one at 660 and 680 nm, respectively (see Figure 2.5b). Polystyrene beads are dispersed in aqueous 2% w/w polyvinyl alcohol (PVA) solution at a concentration of 10^{-6} M and spin-coated onto a cleaned glass cover-slip to provide a 60 nm thin layer of dispersed beads.

For both the emitter samples, we use a glass cover-slip of thickness 170 µm, which is thoroughly cleaned using sonication in acetone and water and exposed to UV. The spin coating is done at a speed of 6000 rounds/min with a ramp of 2.5 seconds for 60 seconds.

2.4 MEASUREMENT TECHNIQUES

A nanoantenna localizes the optical fields at sub-wavelength scales, which decays rapidly within $\approx \lambda/10$ nm [81], therefore the positioning of an emitter in the near-field of the nanoantenna becomes crucial. Here, we use an adapted near-field scanning optical microscope (NSOM) setup for position control of both optical nanoantennas and fluorescent emitters. The schematic of the NSOM setup based on an inverted type confocal micro-

scope is shown in Figure 2.6. For illumination, we use different types of laser sources depending on the application. The setup is equipped with a continuous wave (cw) laser at 647 nm (Coherent Innova 70C spectrum) , a diode pulsed laser (PicoQuant LDH-P) at 633 nm, and a supercontinuum white light pulsed laser (SuperK Extreme, NKT Photonics), which provides a wide range of wavelengths. The laser light is filtered spatially (passing through a pinhole) and spectrally (using a narrow bandpass filter) and collimated before coupling it into the microscope. The laser radiation is focused onto a sample by an oil immersion high numerical aperture objective (NA = 1.3). The sample containing single molecules (or fluorescent beads) is placed on a three dimensional piezo driven stage (Nano-PDQ 350, MCL Inc.). The fluorescence is collected by the same objective and spectrally separated from the incident laser radiation by a dichroic beam splitter and a long pass/band pass fluorescence filter.

NSOM head and scanning modes

A scanning tripod (NSOM head) accesses the molecule sample from above. The tripod holds another three dimensional piezoelectric scanner on which the scanning tip with nanoantenna is placed. A shear-force feedback system controls the vertical axis of the scanner and keeps the scanning nanoantenna tip in the near-field of the molecules on the sample surface at $\approx$10 nm distance [82]. Thus, in total we have five independent axes, which allow us to scan both the molecule and scanning tip with respect to the optical axis of the microscope. It is clearly an advantage over other configurations, as we can perform two different operations with a nanoantenna: the mapping of the nanoantenna modes i.e. *Mode mapping* configuration or the sub-wavelength imaging of single molecules i.e. *Nanoimaging* configuration (see Figure 2.7). In the mode mapping configuration, we select a specific molecule and move it into the focus (optical axis). The nanoantenna tip is scanned across this fixed molecule to map the nanoantenna modes (Figure 2.7a). Here, the molecular fluorescence at positions away from the nanoantenna provide a direct reference for the enhancement produced by the nanoantenna at the hotspots. In the nanoimaging configuration, the nanoantenna tip stays in the optical focus under continuous illumination, and the molecule sample is raster scanned (Figure 2.7b). This way, we obtain the nanoantenna response from every molecule crossing the nanoantenna, and can perform a scan over a large area. Thus, this configuration is used for nanoscale imaging of a single molecule sample with the nanoantenna confining the excitation field.

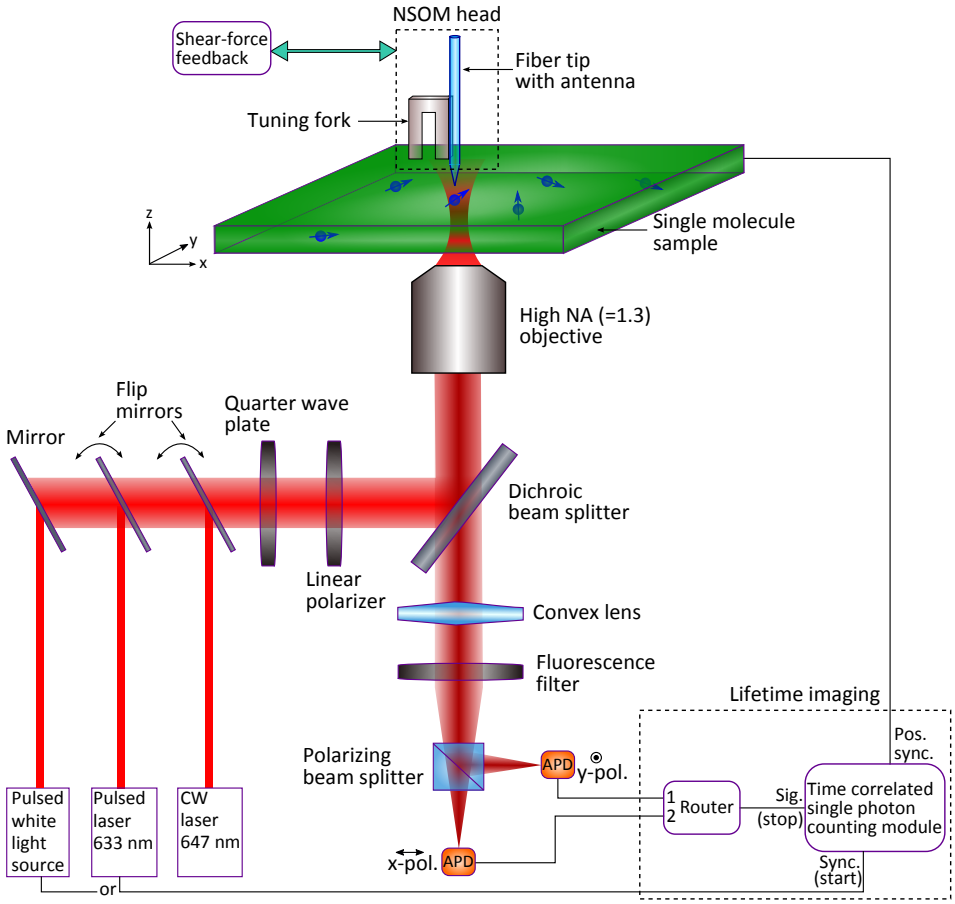

Figure 2.6: A near-field scanning optical microscope (NSOM) based on an inverted confocal microscope. A laser light is focused onto a molecule sample by an oil immersion objective (NA = 1.3), and the same objective collects the fluorescence signal. The setup is equipped with three different laser sources, two pulsed and one cw, each can be coupled into the microscope using flip mirrors. A set of dichroic beam splitter and fluorescence filterso (long or band pass) is used to separate the fluorescence from the incident laser. The fluorescence is further split into two orthogonal polarizations (along x- and y-axes) using a polarizing beam splitter (or into two equal parts by a 50:50 beam splitter) and each focused onto two different avalanche photo diodes (APDs). For lifetime time imaging, the timing output of the two APDs are connected to one input (stop signal) of time-correlated single photon counting (TCSPC) module via a router whereas the TCSPC is synced (start signal) by an excitation pulsed laser. A fiber tip with a nanoantenna glued onto a tuning fork is placed on a three dimensional piezo stage and fixed to a tripod (NSOM head). The NSOM head access the molecule sample (also on a three dimensional piezo stage) from the top and the tip is brought in a close vicinity (≈10 nm) of the sample using a feedback system based on Shear-force.

Apart from the intensity measurements, in our experiments, we can further analyze the fluorescence signal in polarization and measure its time dynamics and photon statistics. The description of the two parts is as follow:

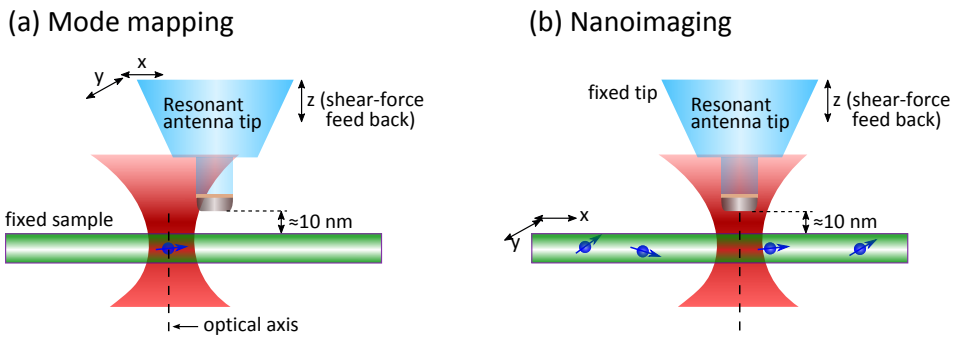

Figure 2.7: NSOM scanning configurations. The setup can be operated in two different scanning modes. (a) Mode mapping, where the nanoantenna tip is raster scanned over a excited molecules to map the plasmonic modes of the nanoantenna. The map produced this way has the contribution of the molecule with or without the nanoantenna.(b) Nanoimaging: The stationary nanoantenna tip is under continuously illumination, and the molecular sample is raster scanned. It allows us to obtain a large area scan of a molecular sample with sub-wavelength resolution.

Polarization resolved intensity measurement

A polarizing beam splitter divides the fluorescence signal into two orthogonal polarizations, each focused onto two different avalanche photo diodes (APDs), for x-polarized and y-polarized fluorescence. As we will see in Chapter 3, this is essential to measure background-free field components of a dipole nanoantenna. Moreover, this polarization resolved measurement can provide direct access to the emission properties of an emitter when coupled to a nanoantenna. This is realized through the *degree of linear polarization* (DOLP) value. The DOLP is an intensity independent parameter, which quantifies the emission polarization and defined as:

$$\mathrm{DOLP} = \frac{I_x - I_y}{I_x + I_y}, \tag{2.1}$$

where I_x and I_y are the collected fluorescence intensities for x and y polarizations, respectively [44]. For the x-polarized and y-polarized fluorescence signal, the DOLP = 1 and -1, respectively.

Lifetime imaging and antibunching measurement

The fluorescence lifetime of a molecule is the time it spends in the excited state before decaying to the ground state by emitting a photon. The fluorescence of a molecule is often observed between the first excited state and the ground state and occurs on the time scale of $10^{-9} - 10^{-8}$ s. Using a time-

correlated single photon counting (TCSPC) module, the arrival time of a emitted photon relative to the excitation pulse can be measured accurately. In the experimental setup (Figure 2.6), we have employed such a TCSPC module (PicoHarp 300, PicoQuant) and fast APDs with time resolution of $\simeq$40 ps (PDM series 50 µm, Micro Photon Devices). Both the detectors are directly connected to a router (PHR 800, PicoQuant) to perform simultaneous two channel time-resolved measurements. The router feeds the TCSPC module with the photon arrival information of each detector. We operate the TCSPC in time-tagged-time-resolved (T3) mode in which it stores the start-stop time difference between the laser excitation (synchronization signal) and the detected photon (stop signal) and arrival time of the event pair relative to the overall experiment time scale i.e. time tagging the event. In order to obtain a 2D lifetime image, an extra information regarding the photons emitted from each pixel needs to be recorded. To synchronize the piezo scanner position, external line markers are recorded to sort out the photon numbers attributed to the different pixels. Moreover, the option of storing channel information for the polarization sensitive detection is incorporated as well. This way, we obtain the full information of the photon dynamics in the form of a T3 file.

Photon correlation statistics measurements are performed by replacing the polarizing beam splitter with a 50:50 beam splitter. We use the TCSPC in histogramming mode which allows us to record number of coincidences i.e. when the two APDs have one detection each. In this configuration, both the APDs are plugged directly into the TSCPC module with one APD providing the start and other the stop signal. Further detail on the antibunching measurements and setup will follow in Chapter 5.

3

VECTORIAL MAPPING OF NANOANTENNA FIELDS

The ability of optical nanoantennas to localize light on sub-wavelength volumes allows strong light-matter interactions and are promising candidates for novel applications. Such confined nanovolumes of light have non-zero field components in all directions (x, y, and z). Unfortunately mapping of the actual nanoscale field vectors has so far remained elusive, though the nanoantenna hotspots have been explored by several techniques. In this chapter, we present a novel method to probe all 3 components of the local nanoantenna field. To realize this, a resonant dipole nanoantenna is deterministically scanned in close proximity to single fluorescent molecules, whose fixed excitation dipole moment reads out the local field vector. With nanometer molecular resolution, we distinctly map x-, y-, and z-field components of the dipole nanoantenna i.e. a full vectorial mode map and show good agreement with full 3D FDTD simulations. Moreover, the fluorescence polarization maps the localized coupling, with emission through the longitudinal nanoantenna mode. Finally, we use the nanoantenna as probe for single molecule imaging with 40 nm FWHM response function. The total fluorescence enhancement is 7.6 times, while out-of-plane molecules, almost undetectable in far-field, are made visible by the strong z-field of the nanoantenna with fluorescence enhancement up to 100 times. Interestingly, the apparent position of molecules shifts up to 20 nm depending on their orientation. The capability to resolve orientational information on the single molecule level makes the scanning resonant nanoantenna an ideal tool for extreme resolution bio-imaging.

3.1 INTRODUCTION

Optical nanoantennas are opening doors to control and optimize light-matter interaction on nanometer scale, as much as radio antennas have made revolutionary changes in the field of communication and modern day technology. Although nanoantennas are truly promising for imaging and sensing at the single molecule level, the molecules need to be controlled accurately both in nanoscale position and in orientation to profit on the potential advantages. Therefore, it is essential to take into account the full vectorial nanoantenna field and control both the position and orientation of the

molecule with respect to the nanoantenna. In this chapter, we demonstrate the full vectorial near-field mode mapping of a resonant dipole nanoantenna with deterministic position control of the molecules. Furthermore, we show a direct application of the nanoantenna in fluorescence enhanced super-resolution single molecule imaging.

Over the years, a large variety of microscopic techniques have been employed to map the local fields of the plasmonic nanostructures. Two-photon photoluminescence (TPPL) has proven useful to investigate the plasmonic modes of gold nanorods [29, 68]. However, being a far-field method, the resolution of TPPL is diffraction limited to ≈200 nm. A nanorod (dipole) antenna operating at visible frequencies has typically a length less than 200 nm and requires a near-field technique to resolve its plasmonic modes. The widely adapted approach is to use "apertureless" near-field scanning optical microscopy (aNSOM). The near-field of the nanostructure is converted into propagating far-field by scattering through a pointed nanotip (semiconductor or metal), whose apex radius determines the lateral resolution [83]. Dorfmüller *et al.* have demonstrated amplitude and phase images of modes of gold nanorods of different lengths in a aNSOM type experiment using an atomic force microscope (AFM) tip [53]. Using the same method operating at mid-IR wavelength, Schnell *et al.* have shown amplitude and phase resolved mapping of a gold rod, disk and triangle nanoantenna [84, 85]. Unfortunately, the AFM tip largely couples to the out-of-plane field component of the nanoantenna, while in-plane components remain mostly unaddressed. Alternatively, scanning electron microscopy has proven very powerful to study the plasmonic modes of a nanostructure. Coenen *et al.* and Knight *et al.* have mapped the modes of gold and aluminum nanorods using e-beam induced cathodoluminescence [69, 86], while electron energy-loss spectroscopy (EELS) has been applied, e.g. to image modes of a silver nanotriangle [87]. Electron microscopy provides wide spectral range from UV to infrared, however due to the direction of the incident e-beam, perpendicular to the sample surface, one maps only the out-of-plane field component of the nanostructures. Thus, no vectorial field map is obtained. Also, it should be noted that all techniques mentioned are merely characterization methods, applicable to nanoantennas fabricated on a planar substrate. Thus, after the characterization, the nanoantennas can not easily be manipulated with respect to photon emitters for applications in optical nanoscopy and spectroscopy.

Here, we present a different technique to map the near-field modes of the optical nanoantenna using single fluorescent molecules as vectorial point probes. The molecular probes offer a number of advantages over the previ-

ously mentioned approaches. First of all, the resolution of such molecular probes is determined by the size of the absorption cross-section, typically in the order of 1 nm. Second, and most importantly, single molecules have a well-defined absorption dipole moment, which interacts preferentially with certain nanoantenna field components and permits to separately image different field components enabling the vectorial mapping of the nanoantenna field [88, 89]. Finally, the detection of the fluorescent signal of a molecule coupled to the nanoantenna provides virtually background free images, as the detected fluorescence is spectrally Stokes shifted compared to the incident wavelength. The evanescent nature of the confined field and the nanometer scale of the nanoantenna both require a high control on the positioning of the molecular probe relative to the structure under investigation. We rely on proven scanning probe techniques, which allow us to bring the nanoantenna and molecule in the near-field interaction and to scan one respect to the other with nanometric accuracy in order to map the interaction with high resolution [33, 34, 73].

Experiments using single emitters as sources for microscopy have so far been limited [66, 90–92]. In a recent experiment by Frimmer *et al.*, a fluorescent bead attached to a tip was used to scan the bead through the near-field of a gold nanowire [67]. However, due to bleaching a large bead (≈100 nm) with many fluorophores was needed, thus compromising the optical resolution and averaging over all field directions. Here, we have inverted the approach by fabricating the nanoantenna directly at the apex of a fiber, while single molecules probing the local field are spin-coated on a flat cover-slip [34, 73]. The scanning fiber tip, containing the nanoantenna, is brought in the close vicinity of the molecule sample and scanned deterministically over these molecules. Discrete bleaching of the molecules is not a limit as there is a large number of molecules available on the cover-slip. Using proposed technique, we experimentally demonstrate the vectorial mode mapping of a resonant dipole nanoantenna. Firstly, we map the total near-field intensity of the resonant dipole nanoantenna. Next, we use the nanoantenna as a probe for nanoimaging of single molecules with enhanced fluorescence. We determine the enhancement and orientational distribution of the molecules from such nanoimages and select specific molecules to map all the three field components (x, y, and z) of the nanoantenna separately. We present FDTD simulation results, which show good agreement for the x-, y-, and z-fields. Finally, the fluorescence polarization of the molecule changes by the reversible coupling to the nanoantenna mode and provides a direct nanoscale map of the local coupling. .

3.2 NANOANTENNA: TOTAL NEAR-FIELD MAPPING

Under a weak excitation field (below saturation), detected fluorescence I from an emitter is proportional to the excitation rate Γ_{exc} and the quantum efficiency of the emission η_a i.e. $I \propto \Gamma_{exc}\eta_a$. Here, we use fluorescent beads and single molecules with high quantum efficiency, and maintain a separation >5 nm between the emitter and nanoantenna to avoid any quenching in the fluorescence [23, 24]. Thus, the variation in η_a is negligible compared to Γ_{exc}. Therefore, the detected fluorescent intensity I depends chiefly on the excitation field **E**. The excitation field **E** is localized in modal hotspots of ≈40 nm in size, still larger than the dimensions of the molecular electronic orbitals, therefore the field **E** is constant over the size of the emitter and within the dipole approximation we can take the transition dipole moment **p** to write the fluorescence intensity I as the vector-product $|\mathbf{p}.\mathbf{E}|^2$ [23, 63]. By scanning the emitter through the excitation field of the nanoantenna, the fluorescent intensity thus maps a vector component of the enhanced excited near-field of the nanoantenna. In this way, the results obtained using the mode mapping technique can be directly compared with FDTD calculated field maps.

Figure 3.1a shows the calculated total near-field intensity distribution (I_{total}) of a resonant dipole nanoantenna for a plane wave excitation, polarized along the long axis of the nanoantenna. The two localized spots correspond to the field maxima of the first-order resonance of the dipole nanoantenna. A measured mode map of a resonant dipole nanoantenna is shown in Figure 3.1b using a 20 nm nanobead as probe in mode mapping configuration (Figure 2.7a). A nanobead is an ensemble of a few hundred randomly oriented fluorescent molecules i.e. a collection of many different dipoles (**p**). Thus, probing the nanoantenna near-field by a bead produces the sum of all possible field components (**E**) that results in I_{total}. First, we imaged a sample containing nanobeads confocally and subsequently selected a nanobead to map the total field intensity of the dipole nanoantenna. The nanoantenna was resonantly driven by linearly polarized far-field laser radiation (λ =647 nm) along its long axis. The resulting plasmon mode localizes at both ends of the nanoantenna for the first-order dipole resonance. This localized field strongly excites the nanobead, and thus enhances its emitted fluorescence. By scanning the nanoantenna over an isolated nanobead, we make sure that the nanoantenna interacts with that specific nanobead only, thus avoiding any contribution from neighboring nanobeads. In the image, the signal outside the bright spots zone is fluorescence of the continuously illuminated nanobead i.e. non-enhanced fluorescence. The increase in the excitation is

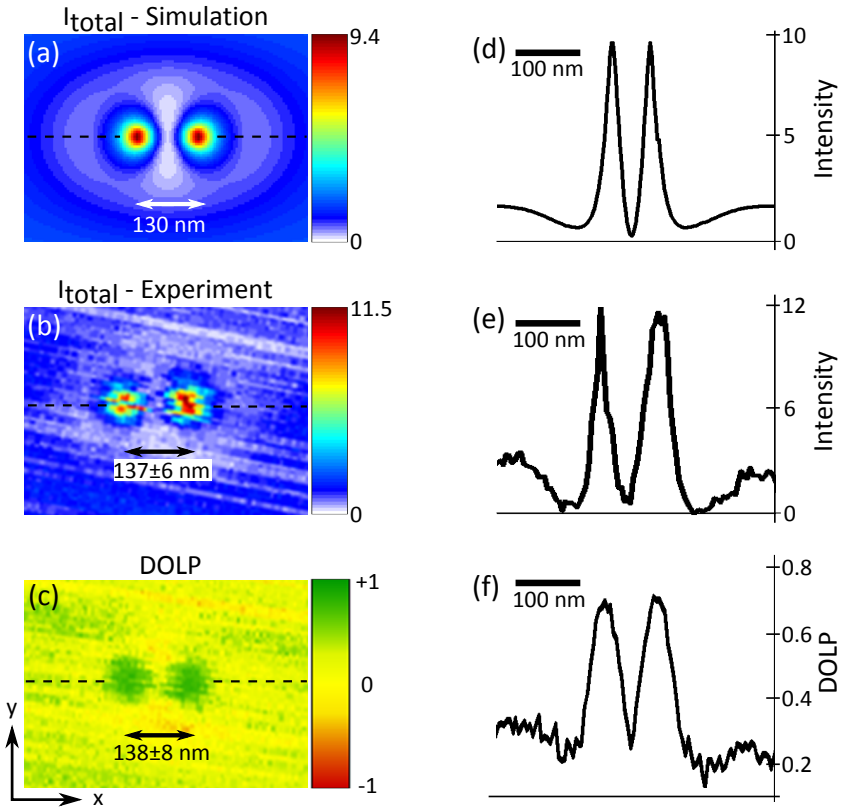

Figure 3.1: (a) FDTD calculation, and (b) Measurement (using a nanobead) of the total near-field intensity of the first-order resonance mode of an aluminum dipole nanoantenna (length=170 nm, width=60 nm, height=60 nm) for a linearly polarized excitation. (d,e) Line profiles along the dashed lines for both the maps show the sharp (≈50 nm) nanoantenna hotspots and the modulation in the field intensity due to the interference between the near-field of the nanoantenna and the excitation (incident) field. Color scales represent the intensity enhancement of the nanoantenna with respect to, respectively, the excitation intensity in the calculation, and the non-enhanced fluorescent signal of the nanobead in the experiment. (c) The measured degree of linear polarization (DOLP) map. (f) Line profile along the dashed line in the DOLP map shows the change of DOLP towards +1 at the hotspots, i.e. linear x-polarization along the long axis of the nanoantenna.

evident as the fluorescent signals from the two spots are much brighter than the non-enhanced fluorescence. Each spot is a convolution of the bead with the extent of the total field at the nanoantenna ends. The typical FWHM of the measured spot size is around 50 nm, which corresponds the field confinement of ≈45 nm convoluted with the 20 nm of the nanobead at the nanoantenna .

The enhanced fluorescence at the hotspots is strongly polarized along the long axis of the dipole nanoantenna. To quantify the emission polarization, we plot intensity independent DOLP (degree of linear polarization) map as defined in Chapter 2 (Equation 2.1). Figure 3.1c shows the DOLP map for the nanobead-nanoantenna system. In the color scale, green denotes

the emission polarized fully along the nanoantenna axis (DOLP = +1), and red the perpendicular polarization (DOLP = -1). The DOLP map clearly shows the distance dependent coupling of the nanobead to the nanoantenna. Away from the nanoantenna the emission is only slightly polarized (DOLP ≈0.2-0.3) due to the far-field excitation with x-polarized light. Approaching the hotspot the emission becomes increasingly x-polarized, with the DOLP reaching up to 0.8, which confirms the coupling of the emission to the nanoantenna mode [60, 64]. Interestingly at the center of the nanoantenna, right in between the two hotspots, the polarization retakes the value of the uncoupled situation, see the line profile in Figure 3.1f.

Both the calculated and measured mode maps in Figure 3.1a,b exhibit a variation in the non-enhanced fluorescence around the localized spots. The fluorescent intensity changes radially outwards from the axis of the dipole (x-axis). This variation can be clearly seen in the line profiles in Figure 3.1d,e, which are cut along the dashed lines in the mode maps. The line profiles show modulation in the intensity going from minimum at the center to maximum at the end of the nanoantenna. The intensity decays away from the nanoantenna and increases again to reach the non-enhanced fluorescence signal level. The reason for this behavior is attributed to interference between the near-field of the nanoantenna and the far-field excitation. The detailed explanation will follow in Chapter 4, where we discuss the interference in the near-field of a nanoantenna.

The constant non-enhanced fluorescence around the nanoantenna hotspots provides a reference to calculate the enhancement caused by the nanoantenna. The two quantities are comparable because both the nanobead and nanoantenna are excited with the same linearly polarized light and excitation power. In order to quantify the enhancement, we scan the nanoantenna over several nanobeads maintaining the same scanning condition, and compare the mean value of the non-enhanced fluorescence with maximum fluorescence collected. The maximum enhancement varies from a minimum value of 3.2 to a maximum of 15.2 with a mean value of 7.6. The measured maximum enhancement range is in good agreement with the calculated maximum enhancement of 9.4 for a distance of 15 nm from the nanoantenna. The measured distance between the two hotspots is ≈ 137 nm, which matches well with the simulation value of 130 nm. It should be noted that the value is less than the physical length 170 nm of the base of the nanoantenna. This difference is due to different vectorial field components, which we address in the following section.

3.3 NANOIMAGING OF SINGLE MOLECULES

Next, we use the resonant nanoantenna to image single fluorescent molecules in the nanoimaging configuration (Figure 2.7b). As a reference first a molecule sample was imaged in confocal mode with circular polarized excitation (λ =647 nm) to obtain diffraction limited fluorescent spots as shown in Figure 3.2a. A near-field image using the nanoantenna probe is shown in Figure 3.2b for the same area as the confocal scan. In Figure 3.2a,b, we plot the total fluorescence signal collected in both x-and y-polarized channels. Highly localized bright spots are clearly visible in the near-field image. We observe the two hotspots corresponding to the first-order resonance mode of the nanoantenna similar to Figure 3.1b. In most of the cases, the width of a fluorescent spot along the long axis of the nanoantenna in the near-field image is ≈40 nm, which is determined by the field localization and thus defines the spatial resolution of the image. Remarkably, we observe some single molecules appear in the near-field scan, which can not be detected in the confocal image (for example those marked with a circle in Figure 3.2a,b). Certain molecules with weak or negligible fluorescent signal in the confocal produce high signal when interacting with the nanoantenna in contrast to some other molecules with strong signal in the confocal and comparable hotspot signal with the nanoantenna. These differences are a clear indication of the interaction of the nanoantenna with molecules of different orientations.

To investigate the effect of orientation on enhancement, we perform a statistical analysis and plot an intensity correlation of the single molecules, as shown in Figure 3.2c. Here, we compare the confocal and near-field images by plotting the near-field intensity caused by the nanoantenna ($I_{antenna}$) against the corresponding confocal intensity ($I_{confocal}$), for each molecule. We have taken the maximum intensity for each fluorescent spot in the confocal image and the maximum out of two localized hotspots in the near-field image. The correlation plot includes close to 150 molecules from different confocal and near-field image-pairs, all with same experimental condition. One can appreciate the distribution of the molecules represented by roughly a triangle area in Figure 3.2c. Fluorescence enhancement lines of 1x, 10x, 100x are indicated (ratio of molecule fluorescence with and without the nanoantenna, respectively) as a reference. There are many molecules with negligible confocal intensities ($I_{confocal}$ < 20 counts/10 ms), which produce strongly enhanced $I_{antenna}$ more than 1000 counts/10 ms, corresponding to an enhancement of 10-100 times. The lower limit of the distribution is given by the 1x enhancement line, which means that some molecules

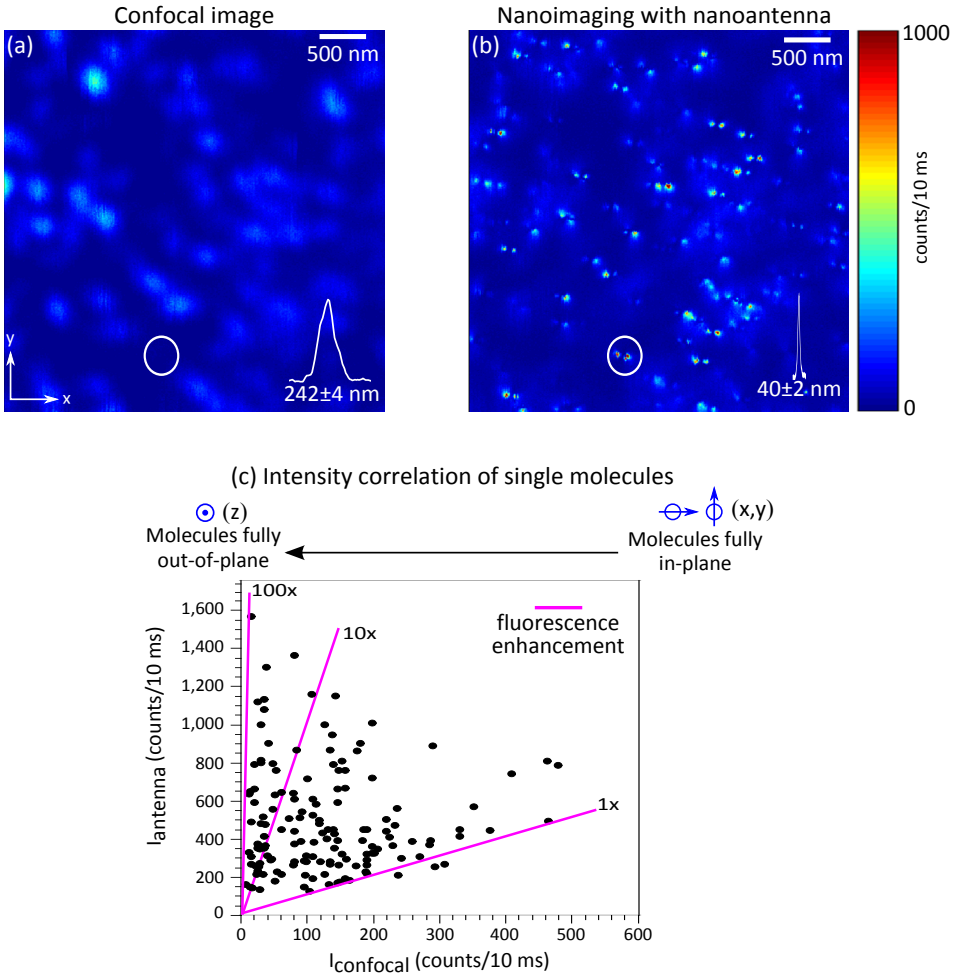

Figure 3.2: Nanoimaging of single molecules using a resonant dipole nanoantenna. (a) Confocal image of single molecules, showing mainly in-plane (x, y) oriented molecules. (b) The near-field scan of same area as in (a) with the nanoantenna probe in nanoimaging configuration. All the molecules including oriented in the z-direction are clearly visible. The image resolution is roughly 40 nm. (c) Intensity correlation between single molecule fluorescence intensity enhanced by nanoantenna and confocal mode. The triangular shaped distribution allows to distinguish molecules with different orientations, as indicated on top of the plot. The enhancement of molecule fluorescence ranges from a lower value of 1 to a upper limit of 100.

hardly interact with the nanoantenna. Also, the absence of molecules below the unity line indicates that the proximity of the aluminum nanoantenna does not introduce quenching.

In the confocal case, the in-plane circularly polarized incoming excitation field mostly interacts with in-plane projections of the absorption dipole of the molecules and can not excite molecules oriented completely out-of-plane. So, only molecules oriented in-plane reach to high $I_{confocal}$ count rate. Thus, going from right to left represents a change in the orientation of the molecules from the in-plane (x- and y-axes) to out-of-plane (z-axis) as

shown on top in Figure 3.2c. The nanoantenna displays x-, y- and z-oriented near-fields, which can excite molecules with any orientation in space. The molecules with negligible $I_{confocal}$ i.e. mostly out-of-plane dipoles orientation, only appear in the near-field image due to an interaction with the z-field component of the nanoantenna. Looking at the maximum $I_{antenna}$ going from in-plane to out-of-plane shows an increasing interaction of the nanoantenna with the enhancement increasing from 1x to 10x and almost 100x for singular out-of-plane cases. Finally, the evanescent nature of the nanoantenna near-field critically effects the excitation, making $I_{antenna}$ to depend on the molecule-nanoantenna distance. Taking into account the varying depth of molecules in the PMMA film, the upper limit of the fluorescence enhancement is found for molecules closest to the nanoantenna for different orientation.

3.4 NANOANTENNA: VECTORIAL NEAR-FIELD MAPPING

Next, we will use the capacity to identify single molecules with different dipole directions to image different near-field components (x, y, and z) of the dipole nanoantenna i.e. vectorial mode mapping. Each single molecule is a dipole with fixed orientation in space and can probe a specific near-field direction of the nanoantenna. The fluorescent intensity I of a single molecule coupled to a nanoantenna for a weak excitation field can be written as the sum of the vectorial contributions $I \propto \sum_i |\mathbf{p}_i.E_i|^2$, where i = x, y, z and $\mathbf{p}_i$ is the absorption dipole moment of the molecule and E_i is the local electric field of the nanoantenna projected on i-axis at the position of the molecule [23, 63]. Consequently, a molecule oriented along the x-axis will only interact with E_x components and produce I_x. In the same way, the molecules oriented along the y- and z-axes will map I_y and I_z, respectively. The vectorial mapping provides direct information on the field intensity enhancement originating from the different field components and location of hotspots at the nanoantenna.

Using correlation plot Figure 3.2c, we select specific molecules oriented along the z-axis and in-plane (x-, y-axes), all of them located above the unity enhancement line. By comparing the confocal polarization channels, we chose distinct molecules oriented along the x-axis and y-axis. The selected molecule is positioned in the focus and the nanoantenna is scanned over the molecule in the mode mapping configuration (Figure 2.7a). In this case, we have chosen circular polarized light as it excites all in-plane molecules. The measured x-, y-, and z-field intensities of the dipole nanoantenna using the selected x-, y- and z-oriented molecules are shown in Figure 3.3d-f.

The simulations are presented in Figure 3.3a-c for the comparison. The long axis of the nanoantenna is along the x-axis for both the simulations and measurements. Both I_x and I_z maps show two hotspots for the first-order resonance mode. The measured x-field component is relatively weak in contrast to the enhanced z-field component as also seen in the calculated maps (Figure 3.3a and c).

Interestingly, the separation between the two hotspots in I_x is $\approx$ 160 nm (Figure 3.3d), while it is $\approx$ 125 nm for I_z (Figure 3.3f). These lengths fit well with the simulation, which gives 170 nm for I_x and 120 nm for I_z. The nanometer molecular resolution of the vectorial mode maps allow us to experimentally quantify these small difference in the distances. Another distinction between the x- and z-field components can be seen by comparing the non-enhanced signal, i.e. the fluorescence of the molecule probes. The non-enhanced fluorescence is almost zero (white) for the measured I_z, confirming that indeed it is an out-of-plane molecule along the z-axis. On the other hand, the measured I_x map shows a variable non-enhanced fluorescence in good agreement with the calculations. This is an in-plane molecule with stronger non-enhanced fluorescence due to the confocal excitation. However, the non-enhanced I_x fluorescence first decreases and then increases, radially outwards from the nanoantenna axis, which can be attributed to the local interference effect (see Chapter 4). The measured map in Figure 3.3d is quite consistent with the calculated map in Figure 3.3a. As the same x-field component of the circularly polarized light interacts with both the nanoantenna and molecule, we can determine the maximum enhancement with respect to interference free non-enhanced fluorescence. The measured maximum enhancement is found to be 2, well comparable to the calculated value.

We observed that all enhanced fluorescence is collected predominantly by the APD in the x-polarized channel (Figure 2.6), which corresponds to the signal polarized along the long axis of the nanoantenna. Figure 3.3g-i show DOLP maps for the x, y and z molecules, clearly showing the nanoantenna controlled emission of the molecules. All maps show high values of the DOLP (green color) exactly at the hotspots. For the x-oriented molecule, Figure 3.3g, the emission polarization becomes slightly more x-polarized, as both the nanoantenna and molecule are oriented along the x-axis. For the z-oriented molecule, Figure 3.3i, the far-field fluorescence is below the background and the DOLP non-defined (varying over full-scale), while the enhanced fluorescence at the hotspots is polarized along the nanoantenna axis with high DOLP. The y-oriented molecule, Figure 3.3h, shows DOLP $\approx$-0.8 (red color), confirming the y-polarized emission. Close to the nanoantenna

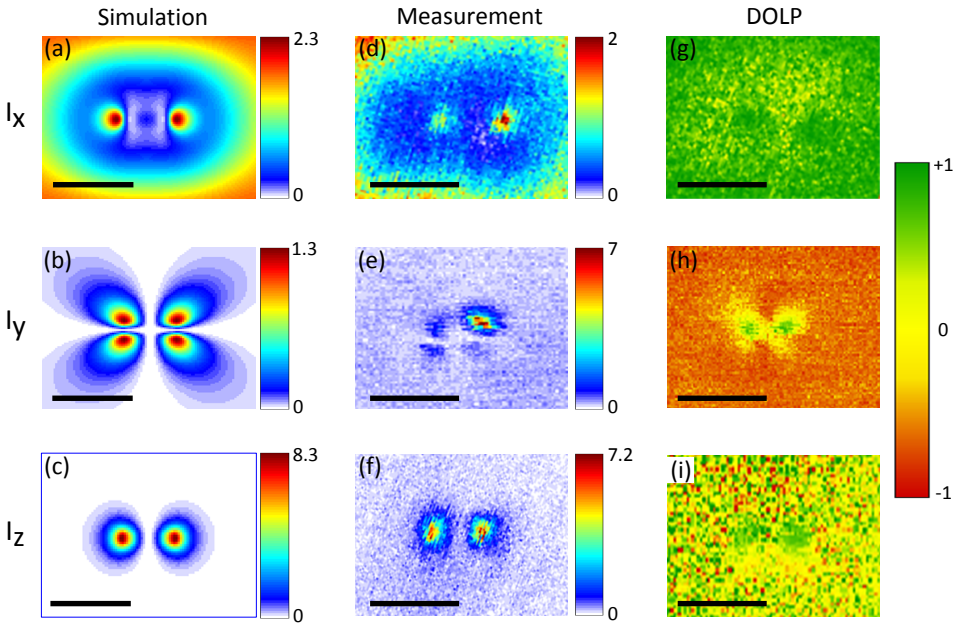

Figure 3.3: Vectorial mode mapping of a resonant dipole nanoantenna. (a-c) Simulated field intensity maps for the x-, y-, and z-field components, respectively. (d-f) Measured intensity maps for x, y, and z molecules showing x-, y-, and z-field components, respectively. (g-i) Measured polarization (DOLP) maps, corresponding to intensity maps (d-f). All the simulations and measurements are performed for the resonant dipole nanoantenna of length=170 nm, width=60 nm, height=60 nm. All scale bars are 200 nm.

the DOLP value changes dramatically from negative to positive (red to green), redirecting the emission into the x-polarized channel. We have taken advantage of this nanoantenna mediated emission for mapping the weak y-field component of the nanoantenna. As shown in Figure 3.3h, the y-field of the nanoantenna excites the molecule and the nanoantenna redirects the emission into the x-polarized channel. Thus, exciting with y-polarization while detecting the x-polarized emission, a background free I_y map is obtained. The mapped y-field intensity component is shown in Figure 3.3e, which is indeed free from the non-enhanced fluorescence of the molecule. The map shows four spots around the extremities of the nanoantenna, well supported by the calculated map in Figure 3.3b. As expected, the I_y field is very weak though we see a very bright spot at right-top corner. This is a cumulative effect of the local interference and the molecule orientation (see Chapter 4). The measured maximum enhancement from other three spots is only 1.1 (Figure 3.3e). Herein, the mean non-enhanced fluorescence was acquired from the y-polarized channel, which collects all the fluorescence of the molecule and is found essentially equal to the non-enhanced fluorescence of a molecule oriented along x-axis.

The intensity enhancement in case of I_z is harder to define as the non-enhanced fluorescence is almost negligible in the mode map. Typically I_z is enhanced up to 100 times. For a quantitative comparison of enhancement for all x, y, z vector components, it is more sensible to compare all signals to the same reference: a non-enhanced in-plane molecule. Therefore, to calculate maximum I_z, we have taken the non-enhanced fluorescence of one of the in-plane molecules, as a molecule along the z-axis will experience the same excitation power. Compared to the in-plane molecule, the nanoantenna enhancement of the z-field intensity is 7.2, a little less than the computed value of 8.3 but in agreement within experimental accuracy. Using the enhancement values of the three field intensity components I_x(=2), I_y(=1.1), and I_z(=7.2), the total field intensity enhancement is 7.5, which is similar to what we have measured with beads (=7.6). We do not observe any local interference effect for I_z as the incoming circular polarized excitation is orthogonal to the z-field of the nanoantenna. The z-field component is most enhanced and located slightly inside from the ends of the dipole nanoantenna, which also explains the distance between the two hotspots shorter than the physical length of the nanoantenna in case of I_{total} (Figure 3.1).

Hotspot positioning

The different distances between the nanoantenna hotspots, 160 nm for the x-molecule and 125 nm for the z-molecule, are caused by the outwards pointing nanoantenna field lines. This effect is clearly observed in Figure 3.4, which shows the field lines in the proximity of the nanoantenna in the xz-plane. The field lines in the x-direction are mainly concentrated at the extreme ends, while the field lines in the z-direction are more concentrated in the zone towards the straight edge. Thus, the hotspots related to the x-field are shifted almost 20 nm compared to the z-field hotspots. The interrelation between the apparent hotspot position and the molecular orientation has important consequences for super-resolution imaging. The presented 40 nm FWHM responses do represent high spatial resolution, in principle allowing a <1 nm localization accuracy. Yet, depending on molecular orientation the actual position can be shifted up to 20 nm. Thus, the presented vectorial mapping is important for correct quantitative interpretation of nanoantenna enhanced super-resolution images.

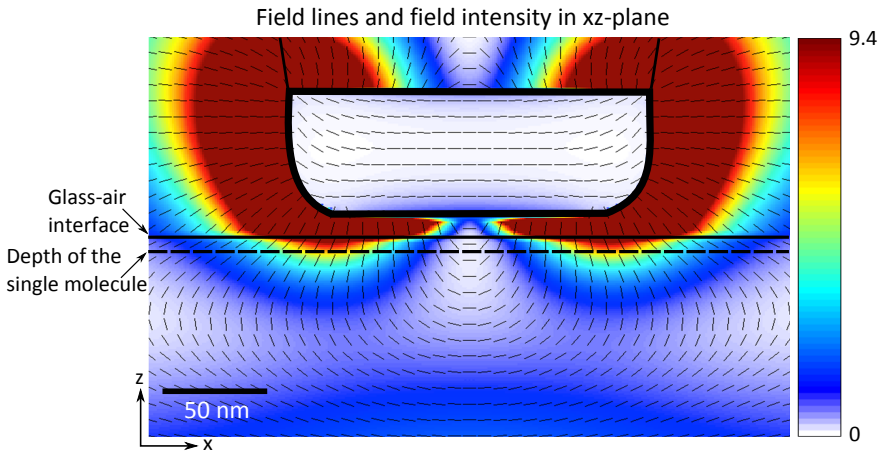

Figure 3.4: Calculated field intensity distribution of the dipole nanoantenna in the xz-plane centered on the nanoantenna. The solid black line shows the cross-section of the nanoantenna. The linear scale gives the intensity relative the incident field intensity. Field lines represent the orientation of the local electric field vector. The straight line under the nanoantenna indicates the glass-air interface, and the dashed line is the level of the molecule. The map clearly shows the evanescent nature of the nanoantenna field together with the bending of the field lines, which underlies the vectorial effect in the local enhancement.

3.5 CONCLUSION

We have measured the total field intensity of an optical resonant dipole nanoantenna, showing mode confinement as small as 45 nm and maximum enhancement of 7.6. Next, we applied the same nanoantenna as a probe to image single fluorescent molecules with a spatial resolution of 40 nm and demonstrated enhancement up to 100x in the molecular fluorescence. We observed that the nanoantenna interacts strongly with out-of-plane molecules, which are hard to detect in the confocal imaging. Intensity correlation statistics allowed us to classify in-plane and out-of-plane molecules and quantify the fluorescence enhancement. Subsequently by choosing molecules with specific orientations, we have shown the full vectorial mode map (x, y-, and z-field components) of the nanoantenna. Using molecular probe, we were able to measure relative strength of the three field components of the nanoantenna mode and separate them spatially with nanometer resolution. All the measurements are in good agreement with 3D FDTD simulations. Moreover, measuring the DOLP, we have mapped the position dependence of the emission control by the nanoantenna mode, for both single x, y, z molecules and fluorescent beads. This presented technique can readily be extended to study modes of the plasmonic nanoantenna with more complex designs, using different metals, and for both positive and negative types of the nanoantenna. The method allows us to de-

terministically place an emitter at the nanoantenna hotspots, exhibiting the usefulness of this kind of scanning nanoantennas to study single photon emitters, and control their excitation and radiative properties. Finally, the resonant nanoantenna allows fluorescence enhanced extreme resolution microscopy with sub-nanometer localization accuracy, when the nanoantenna field lines are taken into account.

4

SHAPING THE NEAR-FIELD OF NANOANTENNAS USING INTERFERENCE

Optical nanoantennas coherently scatter incident optical radiation, creating a localized electromagnetic near-field imprinted with a rapidly changing phase distribution. The nanostructuring of phase by the nanoantenna allows the scattered field to locally interfere with the incident far-field, whose phase lacks nanostructuring and depends only on wave propagation in time and space. Depending on the resonance conditions and material properties, the interference can strongly modify the resultant near-field intensity of the nanoantenna. Here, we present a detailed study, using both measurements and numerical calculations, of the local interference effect in the near-field of a resonant dipole nanoantenna. We use single fluorescent emitters as local detectors to map the field distribution of the nanoantenna with nanometer precision in presence of the incident field. Taking advantage of the vectorial field of the nanoantenna, we are able to retrieve the original orientation of the molecule in space. We experimentally demonstrate the polarization (of the incident field) dependent hotspot switching while keeping the emission of the emitter unchanged. Results shown in this chapter are important for the applications where the enhancement and hotspot position at the nanoantenna are crucial such as in high resolution fluorescence imaging. Moreover, the interference can be exploited to shape the nanoantenna near-field to produce a tailored optical response such as polarization-controlled hotspot switching, as will be demonstrated.

4.1 INTRODUCTION

The concept of interference is not new for propagating electromagnetic (EM) waves, where the superposition of two waves produces a resultant wave. The condition of constructive or destructive interference is set by a phase difference acquired through the propagation of waves in time and space. Similarly, matter confined EM waves such as surface plasmons can also interfere to modify the radiation and propagation properties of the plasmons [93, 94]. In the past, a few studies have observed the presence of interference in the near-field of non-resonant sharp metallic and dielectric nanotips in apertureless-NSOM type experiments [95–97]. In contrast to propagat-

ing waves, such local interference occurs between the incoming field and coherent near-field response of the tip.

The near-field around an illuminated nano-object presents an intrinsic complex 3D vector field distribution [98, 99]. Each spatial component of the field has amplitude and phase structures with sub-wavelength variation length [85, 100]. Thus, when interfering with the incoming excitation wave, the field distribution can be significantly modulated below the diffraction limit. The resulting local field can therefore be shaped and interesting indirect effects can emerge. Recently, local interference has been exploited to control the directionality of a guided mode on a gold film and photonic crystal waveguide [101, 102]. The near-field components of the mediating nanostructure interfere with the excitation field, allowing tunable directional propagation upon changing the excitation field polarization state. Interference effects can thus be used to tailor and control the local field of a nanostructure increasing its potential for applications. Direct experimental observation will allow us to characterize and gain insight into underlying mechanisms responsible for the local interference. To our knowledge, an explicit study of such local interference and control of the local field distribution have not yet been reported.

In this chapter, using direct experimental observations of the local interference together with numerical calculations, we present a detailed study of the interference in the near-field of a resonant dipole nanoantenna. Optical nanoantennas strongly confine the propagating EM field by exploiting non-propagating localized surface plasmon resonances [31, 32]. We use single fluorescent molecules as local nanosized probes to directly access the local interference. We show the effect of the vectorial field distribution of the nanoantenna on the interference by retrieving random 3D orientation of single molecules in space. The right combination of the incident polarization and nannoantenna design can be applied to symmetrically modify the near-field distribution and control the position of a hotspot at the nanoantenna.

4.2 LOCAL INTERFERENCE AT A NANOANTENNA

When illuminated by an incoming propagating wave at frequency ω_0, a nanostructure elastically scatters the incoming field. Any position in space $\mathbf{r}$ around the object experiences a total field $\mathbf{E}_{tot}(\mathbf{r})$, which is a superposition of both the incident field $\mathbf{E}_{in}(\mathbf{r})$, and scattered field $\mathbf{E}_s(\mathbf{r})$. The phenomena of the local interference can be understood by considering the near-field of the nanostructure, non-propagating part of the scattered field. The near-

field is generally characterized by a subwavelength confinement possessing a 3D vectorial distribution. The vectorial field can be decomposed along the three Cartesian axes (x, y, z). The total intensity at the position $\mathbf{r}$ is the time average of $\mathbf{E}_{tot}(\mathbf{r})$ over many optical cycles and is given by $I_{tot} = |\mathbf{E}_{tot}(\mathbf{r})|^2$. Therefore, I_{tot} can be expressed as:

$$I_{tot} = |\mathbf{E}_{in}(\mathbf{r}, \omega_0)|^2 + |\mathbf{E}_s(\mathbf{r}, \omega_0)|^2 + 2\sum_i |E^i_{in}(\mathbf{r}, \omega_0)||E^i_s(\mathbf{r}, \omega_0)|\cos(\Delta\phi_i) \tag{4.1}$$

where i = x, y, or z and $\Delta\phi$ is the phase difference between the ith component of $\mathbf{E}_{in}$ and $\mathbf{E}_s$. The last term of Equation 4.1 causes the field components to interfere and depends on the polarization state of the incoming wave. Each component of the vectorial field exhibits a spatial structure with a strong variation in the amplitude and phase [85, 99]. Based on the amplitude and phase relations with the incoming field components, the resulting intensity can be strongly modified, thus presenting a sub-wavelength interference pattern.

To illustrate this effect, we consider theoretically the simple near-field arrangement around a metallic nanorod antenna close to the dipolar mode resonance (Figure 4.1). With far-field excitation by a propagating wave along the z-direction and linearly polarized along the long axis of the nanoantenna (x-direction), the respective induced x-polarized near-field component will interfere with this incoming field. The near-field distribution of the nanoantenna is altered according to Equation 4.1. We specifically choose an aluminum nanoantenna with length=170 nm, width=50 nm, and height=50 nm to be resonant at a wavelength close to λ = 633 nm. As shown in the previous chapter (Chapter 3), using this dipole nanoantenna gives an advantage as it produces near unity enhancement for the in-plane x- and y-field components at the dipolar resonance, a necessary condition for efficient interference.

In Figure 4.2a-b, we present calculated intensity and phase distributions of the x-field component of the scattered near-field ($\mathbf{E}_s$) at the xy-plane 15 nm below the nanoantenna, matching experimental conditions. Here, the incoming excitation field ($\mathbf{E}_{in}$) is numerically subtracted (see Section 2.2b). For clarity, the intensity is normalized to the intensity of the excitation field and the phase is relative to the excitation field at the position where the field is monitored. We observe two sub-wavelength hotspots at the end of the nanorod (Figure 4.2a), characteristic of the first-order resonance mode of the nanoantenna (see Chapter 3). A third spot, weak in strength, can be

observed at the middle of the nanoantenna between the two hotspots. Here, the field enhancement is weak and the amplitude of E_s^x stays close to the incoming field E_{in}^x. The phase map shows a similar two-lobed pattern with an almost π-phase shift between the two hotspots and middle positions, see Figure 4.2b. According to Equation 4.1, the nanostructuring of the phase permits the field to locally interfere, constructively or destructively, relative to the constant phase of the incoming field. Figure 4.2c shows the resulting intensity (I_{tot}^x) for the x-field component considering both the incoming and scattered field. Due to the local interference, the intensity enhances at the hotspots and cancels at the middle. A characteristic hollow pattern with intensity modulation is created around the nanoantenna (Figure 4.2c).

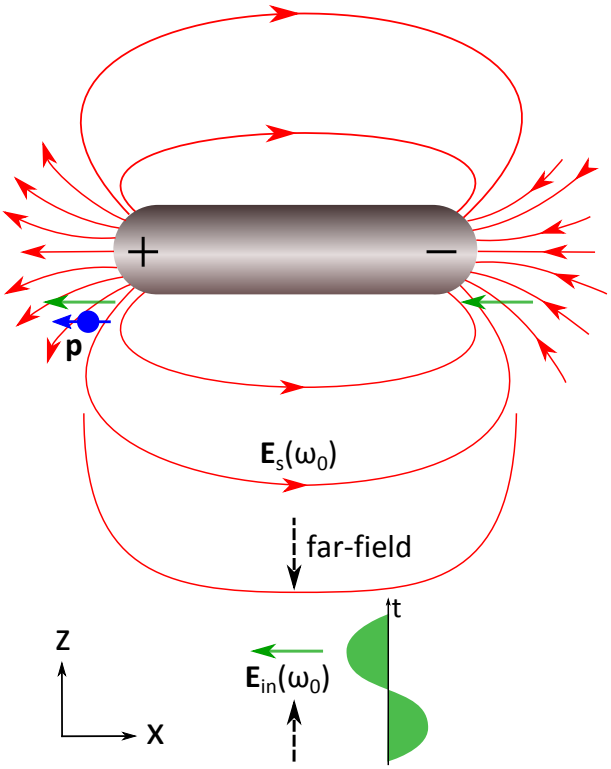

Figure 4.1: Local interference at a nanoantenna. Schematic of a dipole nanoantenna and its scattered field lines $\mathbf{E}_s$ (in red) excited by a linearly polarized incident field $\mathbf{E}_{in}$ (in green) at frequency ω_0. The figure represents a snap shot of the charge distribution and field lines at a fixed time. Since the nanoantenna elastically scatters the impinging radiation, the two fields can interfere at the detector's positions. A molecule (in blue) with dipole moment $\mathbf{p}$ acts as a local detector and sees a superposition of $\mathbf{E}_s$ and $\mathbf{E}_{in}$.

4.3 LOCAL INTERFERENCE PROBED BY SINGLE MOLECULES

Experimentally observation of such local effects remain a challenge. To be observable, the interference needs to occur at the position of a detector, which records the resultant field. Due to the fast decaying near-field of the nanoantenna, the detector must be placed within the decay length of the field. Here, we choose nanometer sized single fluorescent molecules as local nanoprobes (detector), with a fixed absorption dipole moment **p**. The intensity is recorded by scanning a resonant Al dipole nanoantenna over (≈10-15 nm) the single molecules in steps of 5 nm using the experimental setup described in Section 2.4. The nanoantenna is fabricated at the apex of a fiber tip with its long axis along x, and excited by circular polarized light

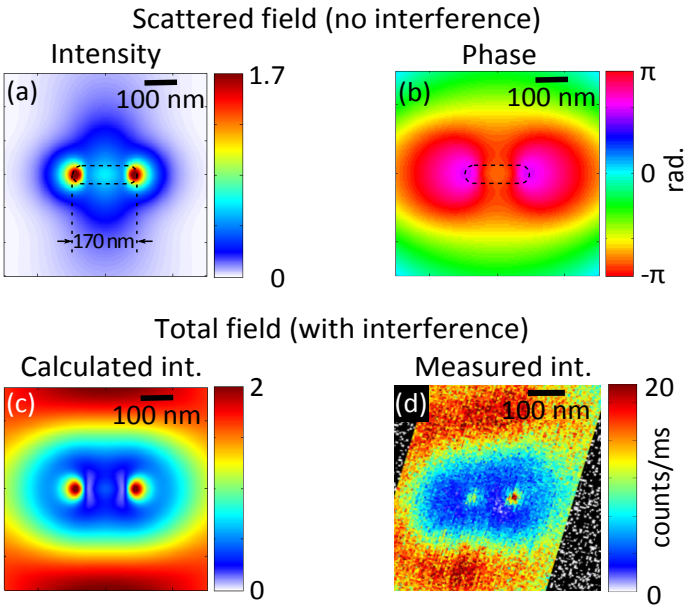

Figure 4.2: Effect of the amplitude and phase distributions on the local interference. The calculated (a) intensity and (b) phase maps of the x-field ($\mathbf{E}_s$) component of a resonant Al (dipole) nanoantenna (see Figure 4.1). The nanoantenna has dimension length=170 nm, width=50 nm, height=50 nm, and excited with linearly polarized light along its long axis at 633 nm. The field is calculated in a plane 15 nm below the nanoantenna. Two hotspots in (a) corresponds to the first-order resonance mode of the nanoantenna. The dashed outline represents the shape and size of the nanoantenna. (c) The calculated total field intensity of the same nanoantenna in the presence of the incoming field ($\mathbf{E}_{in}$), considering the interference. The maps clearly show the change in the field strength of the nanoantenna due to the interference. The destructive interference completely cancels the weak spot in the middle, which is present in (a). (d) The measured x-field map using a single fluorescent molecule, which includes the local interference effect shows the similar hollow pattern as in the calculated map (c). The black area (no fluorescence) in the image is due to the blocking of the excitation laser beam to protect the molecule from photo-bleaching. For the calculated maps, the intensity is normalized to the excitation field.

at 633 nm (see Section 2.1). In the experiments shown here, we use two different resonant dipole nanoantennas of the same dimension, length=170 nm, width=50 nm, height=50 nm.

A molecule ($\mathbf{p}$) placed at any position $\mathbf{r}$ close to the nanoantenna experiences the total field $\mathbf{E}_{tot}$ (Figure 4.1) and thus can access the interference. The resultant fluorescence signal is expressed as:

$$I_f \propto |\mathbf{p}.\mathbf{E}_{tot}(r)|^2 = \sum_i |p_i.E^i_{tot}|^2 \tag{4.2}$$

Selecting an orientation of the absorption dipole moment of the molecule allows probing a specific or a combination of field components [99]. On probing the x-field component using the right molecule orientation, we obtain a similar intensity pattern as in the simulation, two hotspots surrounded by the variable intensity pattern (see Figure 4.2d). The resultant intensity is modulated by the local interference due to a sharp change in the amplitude and phase distributions. Similar to the calculated intensity (Figure 4.2c), we observe a hollow pattern around the two hotspots in the measured intensity map (Figure 4.2d). Thus, the measurement confirms the presence of the local interference and its influence on the near-field distribution of the resonant nanoantenna.

4.4 EFFECT OF THE POLARIZATION ON THE LOCAL INTERFERENCE

According to Equation 4.1, different field components can contribute to the local interference due to the 3D vectorial nature of the near-field. This depends on the polarization state of the incoming field. A circular polarized wave is composed of x- and y-field components with equal amplitude and $\pi/2$ phase difference. On exciting the dipole nanoantenna, such an excitation field predominantly excites the dipolar mode while the interaction of the nanoantenna with the y-field remains weak. Nevertheless, considering Equation 4.1, both the x- and y-field components of the nanoantenna can be affected by the local interference. A molecule in close vicinity to the nanoantenna experiences this combination of fields, which strongly depends on the orientation of the molecule in space.

Figure 4.3a-e show measured intensity maps using the nanoantenna described before, excited with circular polarized light, for different molecule orientations. Depending on the molecule orientation, the maps exhibit large variation in intensity patterns showing different fluorescence background levels (fluorescence of the molecule alone), symmetric or asymmetric hotspots,

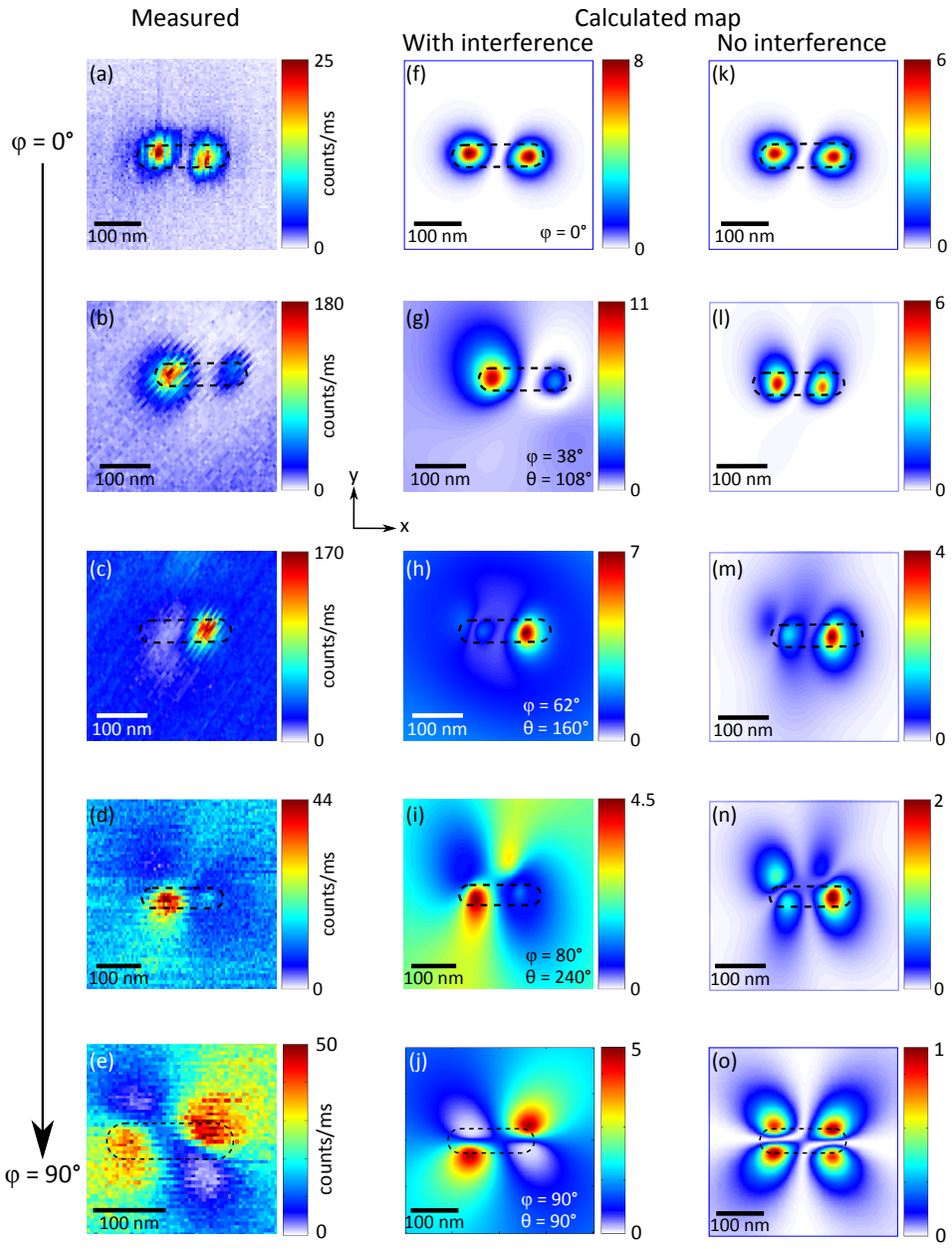

Figure 4.3: (a-e) Measured intensity patterns of the nanoantenna excited by circular polarized light at 633 nm and probed by five different molecules. The variation and asymmetry in the intensity patterns arise due to the local interference of $\mathbf{E}_{in}$ and $\mathbf{E}_s$, and the projection of the resultant field on the molecule's dipole. (f-j) The FDTD calculation of the intensity patterns at 15 nm below the nanoantenna when excited by circular polarized light same as in the experiments. The calculations are performed considering the interference effect, and approximate value of the angles φ and θ are retrieved based on Equation 4.2, which are shown in the figure. The calculated intensity maps match very well with the measured maps, which show the values of φ and θ closely describe the original orientation of the molecules in the measurements. (k-o) Calculated maps without taking interference into account. The asymmetry shown here is due to the orientation of the molecules.

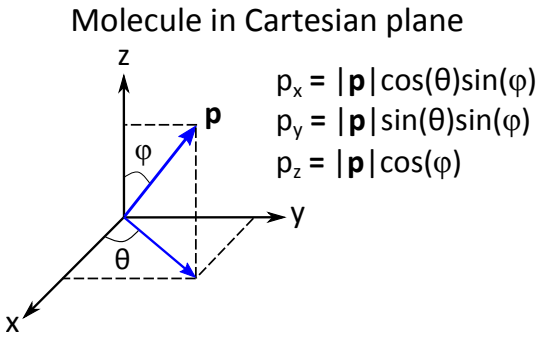

Figure 4.4: Schematic of an arbitrary oriented molecule dipole **p** in Cartesian plane (xyz). The **p** has the polar angle (from the z-axis) of φ and the azimuthal angle is θ. Projection of the dipole on each axis is defined as p_x, p_y, and p_z whose values can be written in form of the two angles as shown in the figure.

bright and dark spots as well as butterfly shaped distributions. Due to the circular polarization of the incoming field, molecules oriented along the xy-plane will be most effected by the local interference. On the other hand, molecules oriented principally along the z-axis will be less sensitive to the interference. Apart from the polarization of the excitation field, which is responsible for the local interference, we also need to take into account the orientation of the single molecules with respect to the nanoantenna while interpreting the intensity images. For an arbitrarily oriented single molecule in the xyz-plane, with polar angle of φ and azimuthal angle θ (see Figure 4.4), the measured field intensity can be given by Equation 4.2. The components of the total field ($\mathbf{E}_{tot}$) are known from the FDTD calculations using identical excitation conditions. By comparing the experimentally obtained intensity maps and calculated maps through Equation 4.2, the orientation of the molecule relative to the nanoantenna can be deduced.

Results of the simulations with deduced orientation of molecules are shown in Figure 4.3f-j. The retrieved orientations allow us to order molecules from fully out-of-plane (z-axis) to fully in-plane (xy-plane) configurations (see the arrow), the last one corresponding to a full y orientation (Figure 4.3e,j). The reconstructed intensity patterns match well with the measured maps, suggesting that calculated angles closely represent the original molecule orientation in the xyz-plane. To emphasis the interference effect, we also plot the intensity maps by subtracting the incoming field from the total field, see Figure 4.3k-o. We observe a non-modified characteristic dipolar two hotspots pattern for the fully z-oriented molecule (Figure 4.3a,f,k). The intensity pattern starts deviating from the typical pattern as the angle φ starts increasing. For a fully y in-plane molecule the pattern shows two diagonal bright and dark lobes (Figure 4.3e,j) instead of an expected four-lobed pattern (Figure 4.3o).

As discussed before, we observed that the more the molecule is oriented along the z-direction, the lower the background fluorescence is and the less it is affected by the interference. As expected, the in-plane oriented molecules produce a high background fluorescence. Thus, the in-plane molecules show high sensitivity to the local interference and exhibit strange patterns, which have major discrepancies compared to corresponding patterns where interference is not present (Figure 4.3i,n and j,o). In addition to the modification to the field distribution, significant enhancement in the near-field intensities can be produced by the interference. In these maps, we see how the combination of local interferences involving the two in-plane components can drastically alter the resultant intensity pattern.

4.5 LOCAL INTERFERENCE FOR HOTSPOT SWITCHING

As previously demonstrated, going from linear to circular polarization excitation allows local interference for the y-field, which in-turn modifies the effective local field. For the dipole nanoantenna, the local interference creates an asymmetric four-lobed pattern for the y-field component instead of the expected symmetric four-lobed pattern (Figure 4.5b,d). Indeed, it shows two-bright spots in one diagonal (point 1 and 3) and two-dark spots with almost no fields on the opposite diagonal (point 2 and 4). In the original (without the interference Figure 4.5b) map, the four lobes of the y-field component of the nanoantenna show almost equal amplitudes, however each lobe has a phase difference of π compared to its neighbors (Figure 4.5a). Thus, the amplitude and phase relations for the incoming y-field is such that it results in quasi-fully destructive interference for the two-dark spots while consequently the two-bright spots present constructive interference with 5-fold intensity enhancement (Figure 4.5d). The position of the bright and dark spots have their origin in the phase distribution, notably the phase difference between the lobes. Thus, by changing the polarization state of the incoming field from left to right circular polarization, we alter the situation. Indeed, the phase difference between the x- and y-field components of the incoming field is π-shifted, passing from $\pi/2$ to $-\pi/2$ (Figure 4.5c). Consequently, the constructive and destructive interference are interchanged leading to hotspot inversion. This way, external polarization control of the hotspots can be realized directly using the near-field of the nanoantenna.

We experimentally demonstrate this switching effect by using different y-oriented molecules as local nanoprobes (Figure 4.5f-i). All the measured maps clearly show two hotspots, which switch with high contrast on changing the incoming polarization state. The two maps for each polarization

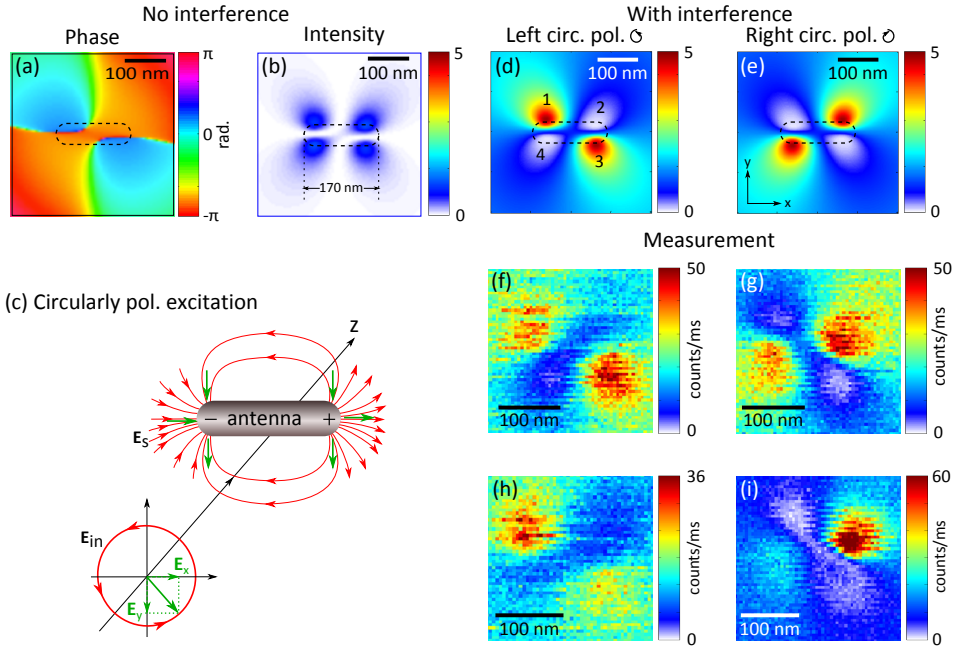

Figure 4.5: Controlling the hotspot position. (a) Phase and (b) intensity distribution of the y-field of the nanoantenna without the interference. The intensity map shows the typical four-lobed pattern and lobes exhibit a phase difference of π relative to each other. (c) A schematic of a dipole nanoantenna and its field lines in the xy-plane when excited by a circular polarized light propagating along the z-direction. Different colors for field components of the incident light and nanoantenna are chosen for the sake of clarity. The FDTD simulated y-field maps of the dipole nanoantenna for two different polarizations conditions. (d) The nanoantenna is excited with left circular polarized light. The mode pattern changes to a two-lobed pattern. The field intensity completely vanishes at positions 2 and 4 due to the destructive interference. More importantly, the constructive interference enhances the field by a factor of 5 at the hotspots, positions 1 and 3. (e) Right circular polarized light flips the hotspot positions by 90°. Dashed outline represents the nanoantenna. (f-i) Measured maps for the two polarization states using y-oriented single molecules.

state emphasize the reproducibility of the images and match very well to the calculated maps (Figure 4.5d,e). A small asymmetry in some maps, mainly in Figure 4.5i can be attributed to the imperfectness in the orientation of the molecule. Thus, the external control of the polarization state of the incoming wave allows the shaping of the near-field distribution of the dipole nanoantenna.

According to Equation 4.2, depending of the incoming polarization state, the local interference can differently modulate the total intensity pattern, which is the superposition of the modified x-, y-field components together with the z-field component. Simulations and experiments confirm this modification, revealing a small but notable effect (Figure 4.6). For experimental demonstration, we use fluorescent nanobeads as probes, sensitive to all components of the field (Section 3.2). Going from left to right circular polarized

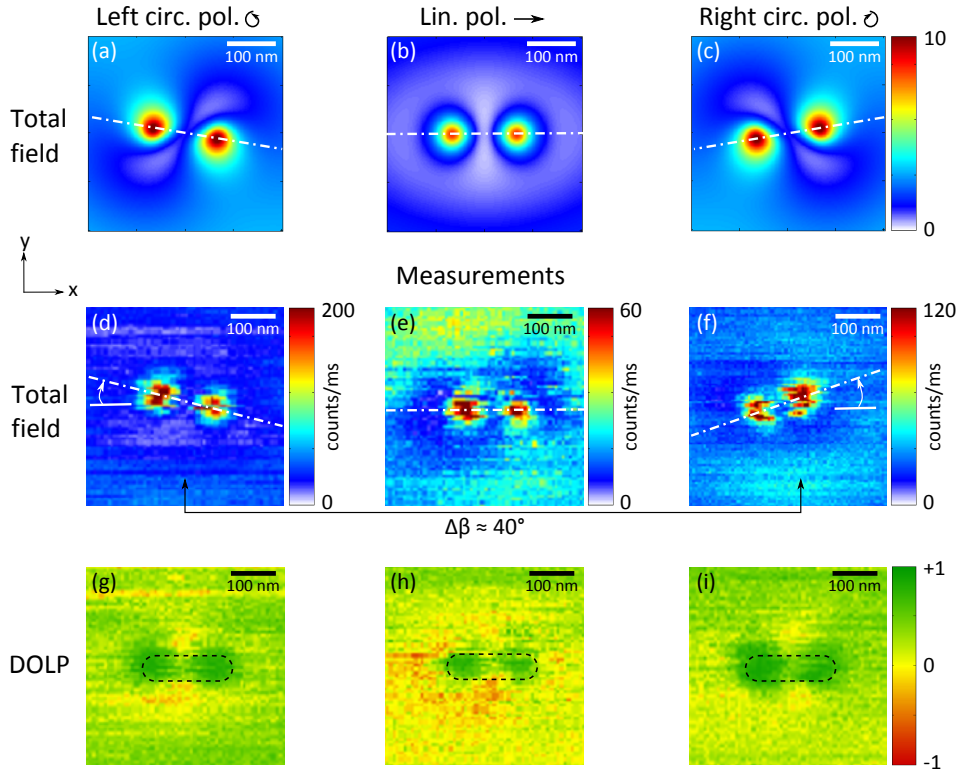

Figure 4.6: Interference effect on the total field. The calculated total field maps of the nanoantenna for three different excitation polarizations states. (a) Left circular, (b) Linearly, (c) Right circular polarized. The two hotspots are rotated in the opposite direction in case of left and right circular polarization, while the hotspots are on the horizontal line for the linear polarization, see the dashed-dotted line. (d-f) The measured total field intensity maps show the same effect as the calculations for the different polarization states. We use single fluorescent nanobeads to measure the total field of the nanoantenna. We measure the total rotation angle $\Delta\beta \approx 40°$ between the two cases (d,f). (g-i) DOLP maps, exhibiting emission polarization, confirm the main axis of the nanoantenna along x in all the three cases.

excitation slightly rotates the hotspot axis clockwise and anticlockwise direction, respectively (Figure 4.6d,f), while for the linearly polarized state, the two hotspots lie on a horizontal line Figure 4.6e. The experimental results match very well with the calculated maps.

To check that this slight hotspot rotation is not an artifact due to the wrong estimation of the nanoantenna orientation, we plot degree of linear polarization (DOLP) maps, which confirm the real physical orientation of the nanoantenna. The DOLP is an intensity (excitation) free parameter, which quantifies the polarization of the fluorescence emission (see Equation 2.1). It measures the change in the emission polarization of the nanobeads when coupling efficiently with the nanoantenna [64, 99]. The green spots positions are thus free from any interference effect and reveal the real orientation of the nanoantenna (Figure 4.6g-i). Thus, this confirms

that the rotation in the hotspots axis is driven by the change in polarization state of the excitation light and do not represent the real physical orientation of the nanoantenna. Externally setting the polarization state of the incoming field allows us to shape the near-field distribution and control hotspot positions.

4.6 CONCLUSION

In conclusion, we have studied in detail the important effect of interference in the near-field of an optical nanoantenna. The vectorial near-field distribution and the nanostructured phase of the nanoantenna allow us to observe this interference effect, which is the basis of several applications. We have experimentally demonstrated the local interference effect on a resonant Al dipole nanoantenna using single fluorescent molecules as local probes. We studied the role of the excitation polarization on the local interference and how it can modify the near-field distribution around the nanoantenna for a circular polarization. A significant change in the measured field distribution has been observed for different molecules. The in-plane nanoantenna field components modified the most due to the in-plane incident polarization, and the out-of-plane component remains largely unaffected. The 3D orientation of single molecule probes manifested in the near-field maps have been deduced taking using the numerical simulations. Exploiting the local interference, we have demonstrated the polarization control of hotspots at the nanoantenna. This polarization-controlled switching can be applied to change the direction of light flow in all optical nanocircuitry and using nanoantennas as a switch or splitter to control the optical near-field in an integrated plasmonic circuits [103, 104].

5

OPTICAL NANOANTENNAS AS CAVITIES

Optical cavities enhances light-matter interactions between photon emitters and optical fields, creating a wide variety of opportunities in sensing, quantum information, and energy capture technologies [105–107]. To boost the emitter-cavity interaction, i.e. the coupling strength g, ultrahigh quality cavities have been concocted yielding photon trapping times of μs to ms [108]. Yet with such strong coupling comes poor photon output which prevents the route to applications. To preserve high photon output and rapid response it is advantageous to strive for highly localized electric fields in lossy cavities. Plasmonic (optical) nanoantennas are ideal candidates combining low quality factors with deeply localized mode volumes, while still displaying large g, provided the emitter is positioned correctly within the nanoscale mode volume. In this chapter, with nanometer resolution, we map and optimize the coupling strength of an optical dipole nanoantenna to a single molecule at various orientations, obtaining g_{max}= 206 GHz. This provides ideal conditions for fast and pure non-classical photon emission, enabling a pulsed single photon source with an emission rate exceeding 1 GHz. Optical nanoantennas thus present a unique opportunity in single emitter cavity quantum electrodynamics (QED) to provide bright and ultrafast single photon sources at room-temperature for quantum technologies.

5.1 INTRODUCTION

Photons play a key role as efficient information carriers in quantum technologies. Single photons can encode and broadcast quantum information between distant computational nodes using several various degrees of freedom (polarization, wavelength, timing or path). Scalable quantum computing schemes require efficient coherent interaction between weak single photon fields and matter. To boost this interaction, optical cavities are normally used to tailor the optical field at the emitter. Such cavity QED schemes can achieve the desired coherent interactions, known as the strong coupling regime, provided the cavities show high quality factors and small mode-volumes (high photon density). Nevertheless, due to the large number of loss channels, coherence is notoriously difficult to maintain and prevents scalability to large quantum circuits at room temperature [109]. All-optical

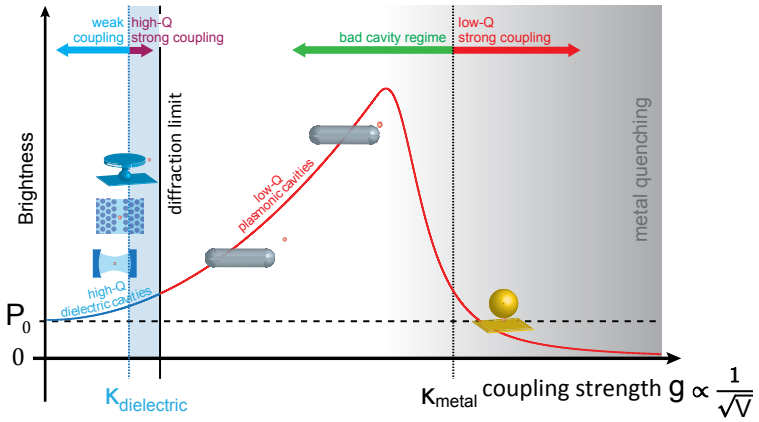

Figure 5.1: The optimal regime for strong coupling g and bright photon emission from the coupled emitter-cavity system. High quality factor Q (low losses $\kappa_{dielectric}$) prevent strong photo-emission rate in dielectric-type cavities as with increasing coupling strength, strong coupling is quickly reached despite the diffraction limit preventing further decrease of mode volume. Plasmonic nanocavities with low Q (high κ_{metal}) and sub-diffraction limited mode volumes, allow coupling to further increase while remaining below losses in the bad-cavity regime, allowing large increases in the photon emission rate. As coupling increases past the metal loss rate (κ_{metal}), into strong coupling, photon emission is inhibited by quenching to the metal surface, due to the exceptionally small mode volumes (<50 nm^3) required to overcome the low Q factor of plasmonic nanocavities.

schemes based on linear-optical quantum computing [1] or probabilistic entanglement [110, 111] are a promising alternative to remove most of the burden of maintaining matter coherence, allowing easier scalability [112]. Such all-optical systems rely principally on single photon sources with ideal characteristics: on-demand availability, frequency-bandwidth limited , emission into a defined spatio-temporal modes, and crucially high brightness corresponding to large photon output rate [113]. Here we present such a triggered, pure (must emit one and only one photon at a time [59, 114]), and potential ultrafast single photon source at room-temperature based on a single molecule emitter deterministically to a plasmonic nanocavity with high antenna efficiency, at the optimal nano-position for enhanced photon density.

Single photons are emitted upon transition from an excited state to the ground state of a single quantum system, such as a quantum dot, molecule, single atom or nitrogen vacancy (NVs) in diamond at a radiative rate Γ_0. Control of the emission is conventionally achieved by coupling the system to an optical cavity with high quality factor Q, such that the cavity mode emits at a rate $\kappa = \omega_a/Q$, where ω_a is cavity's resonance frequency. The coupling strength g of the quantum system to the cavity mode reaches the strong coupling limit when $g \gg \kappa, \Gamma_0$, meaning that the excited state en-

ergy oscillates many times between the photon emitter and cavity before decaying [20, 115–117]. Striving for such strong interactions, Fabry-Perot, whispering gallery and photonic crystal type cavities have been fabricated with high Q factors (up to 10^9), and mode volumes from macroscopic to wavelength dimensions [15, 108]. Yet the high Q implies long photon storage time, resulting in a low emission rate κ, i.e. slow photon emission (Figure 5.1). The second main regime is the weak coupling regime, where decay rates κ and Γ_0 dominate over the coupling strength, i.e. $g \ll \kappa, \Gamma_0$ [22, 118, 119]. In this regime, the energy transfer between the emitter and cavity mode is irreversible lost to the environment before any coherent exchange can take place.

For a fast single photon source, one should consider the emission rate of the combined emitter-cavity system, which is approximately $4g^2/\kappa$ at resonance (see Appendix). This rate can be far superior to the free-space radiative rate Γ_0, leading to a large Purcell factor: $F_p = 1 + 4g^2/(\kappa\Gamma_0)$ (see Equation A.5 in Appendix). The large Purcell factor F_p means that the photon is efficiently and rapidly emitted into the cavity mode. At the same time though, the cavity should radiate efficiently with high κ. Hence, the criteria for an efficient fast single photon source are: $g^2 \gg (\kappa\Gamma_0)$ and $\Gamma_0 \ll g \ll \kappa$. This is the intermediate coupling regime: the coupling is strong, yet in a "bad-cavity" with $\kappa > g$ [22, 120].

Plasmonic (optical) nanoantennas are exemplary cavities for coupling in the "bad-cavity" regime [18, 21, 22]. The light in plasmonic nanoantennas is coupled strongly to electron oscillations, leading to high radiative losses and low Q factors, meaning high photon output. Furthermore, the emission can be highly directed providing high nanoantenna gain and optimal usability of emitted photons [31]. More importantly the cavity mode volume V_m, is extremely sub-wavelength, orders of magnitude below $(\lambda/n)^3$, providing large spatial overlap of the quantum system with the cavity mode. Indeed strong Purcell enhancements of $10^2 - 10^3$ have been shown using plasmonic resonators [23, 57, 63]. Even recently, the strong coupling regime has been reached with plasmonic nanocavity systems with $Fp \sim 10^6$ at a 40 nm^3 volume [20]. Unfortunately, at these minute volumes, ohmic losses take over and direct quenching of the spontaneous emission means that the photon output (radiated power P) is severely limited (Figure 5.1). Thus, beyond creating a lossy plasmonic nanocavity with a nanoscale local mode volume, the main challenge is to situate a single photon emitter at the optimal position for highest coupling strength g, while preserving the high photon emission rate.

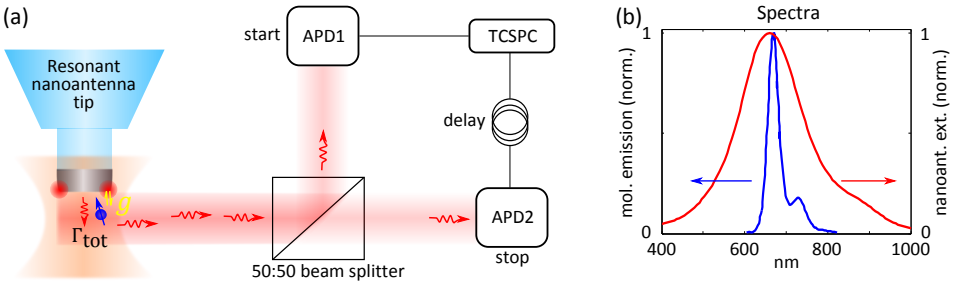

Figure 5.2: Scheme to measure the cavity QED parameters of a molecule-nanoantenna cavity system. (a) The interaction between the molecule dipole (in blue) and nanoantenna is given by the coupling strength g. By scanning the nanoantenna over the molecule, we measure the fluorescence intensity and lifetime map of the molecule at all nanoantenna positions. The lifetime map gives us access to the total decay rate Γ_{tot}, needed to extract g. At the same time, intensity correlation measurements using the Hanbury Brown-Twiss (HBT) setup allows us to measure the statistics of the emitted photons from the single molecule. The HBT setup includes a 50:50 beam splitter and two APDs, which are placed at two outputs of the beam splitter. A photon detection in APD1 starts the measurement and it stops with a photon detection in APD2. Both the APDs are connected to the TCSPC, which measures a difference between photons arrival time in the two APDs. This generates a coincidence histogram, where each count represents a coincidence i.e. a photon pair. A physical delay line (a wire) is added to APD2 to sweep the negative times. (b) The FDTD calculation of the extinction spectrum (red) of the resonant nanoantenna, producing Q factor of ≈5. The emission spectrum of the molecule is shown in blue, which perfectly overlaps with the maximum of the nanoantenna resonance.

Here we present deterministic positioning, with few nm accuracy, of a single molecule in the proximity of a plasmonic dipole nanoantenna, providing a nanoscale map of the coupling strength g, revealing strong Purcell coupling and a maximal g value of 206 GHz, strongly dependent on the nanoscale position and orientation of the molecule within the cavity mode. Optimizing the coupling, we show the nanoantenna-controlled speeding up of non-classical photon emission, enabling a bright and high-purity single photon source with emission frequency exceeding 10^9 sec^{-1}.

5.2 MAPPING OF THE COUPLING STRENGTH

Figure 5.2a shows a simplified schematic of the molecule-nanoantenna cavity system, highlighting the measurement strategy to obtain cavity QED parameters. An Al dipole nanoantenna is scanned over an excited single fluorescent molecule with a step of 5 nm in the mode mapping scanning configuration (Figure 2.7a). The nanoantenna has dimension length=175 nm, width=50 nm, height=50 nm and is resonant for the first-order mode at around 680 nm, which is the maximum of the molecule's emission wave-

length. The molecule is excited by a pulsed laser (pulse width < 100 ps) at 633 nm with circular polarization. We simultaneously record the intensity and lifetime maps of the molecule-nanoantenna coupled system. To construct the lifetime map, the arrival time of each photon is recorded using the TCSPC in T3 mode as described in Section 2.4. This way, we obtain the excited state lifetime of the molecule at all the positions of the nanoantenna. The lifetime map gives a direct access to the total rate Γ_{tot} at and the rate Γ_0 away from the nanoantenna.

Figure 5.3 shows the florescence intensity map and lifetime time measurements of the molecule-nanoantenna cavity. The intensity map (Figure 5.3a) exhibits the characteristic two-lobed pattern corresponding to the fundamental mode of the dipole nanoantenna. The spontaneous decay rate (1/lifetime) of the molecule at three different points of the intensity map is shown in Figure 5.3b. Away from the nanoantenna (point 1), the uncoupled molecule has a measured lifetime of τ_0 = 4.79 ns (= Γ_0^{-1}). A sharp decrease in the lifetime is seen at the hotspots, points 1 and 2 in Figure 5.3a. The lifetime decreases to τ_{tot} = 0.47 ns (= Γ_{tot}^{-1}) at point 2 and 0.76 ns at point 3. In our experiments, we maintain a molecule-nanoantenna distance >5 nm to prevent quenching and increase of the non-radiative rate (Γ_0^{nrad}) [23, 63]. Thus, the decrease in the lifetime is due to the increase in the radiative rate, confirming pure Purcell enhancement for our molecules with near unity quantum yield and resulting in 10x enhancement in the spontaneous emission.

Figure 5.3c shows the mode profile of the intensity and lifetime maps along the hotspots (see the dashed line in Figure 5.3a). The intensity enhancement (squares) and lifetime reduction (diamonds) show a mode width of ≈40 nm, which corresponds to a lateral mode confinement of $\approx 10^{-3}\lambda_f^2$, where λ_f is the molecule's emission wavelength. The average intensity enhancement is around 4 with 7-fold average reduction in the lifetime at the nanoantenna. The small difference between the two quantities can be attributed to the resonance of the nanoantenna, which is tuned for the emission wavelength. Moreover, the intensity pattern and its enhancement are affected by the local interference as discussed in Chapter 4. The asymmetry in the lifetime profile is mainly due to the orientation of the molecule relative to the nanoantenna, since no interference occurs at the emission wavelength.

At resonance, in this intermediate-coupling "bad-cavity" regime ($\Gamma_0 \ll g \ll \kappa$), the contribution of the nanoantenna to the total decay rate is $\Gamma_{ant} = 4g^2/\kappa$. The total emission rate of the molecule thus becomes $\Gamma_{tot} = \Gamma_{ant} + \Gamma_0^{rad} + \Gamma_0^{nrad} = \Gamma_{ant} + \Gamma_0$. We measure the total decay rate ($\Gamma_{tot} \propto 1/\tau_{tot}$) with and without the nanoantenna (Γ_0) in a single scan for one and the same

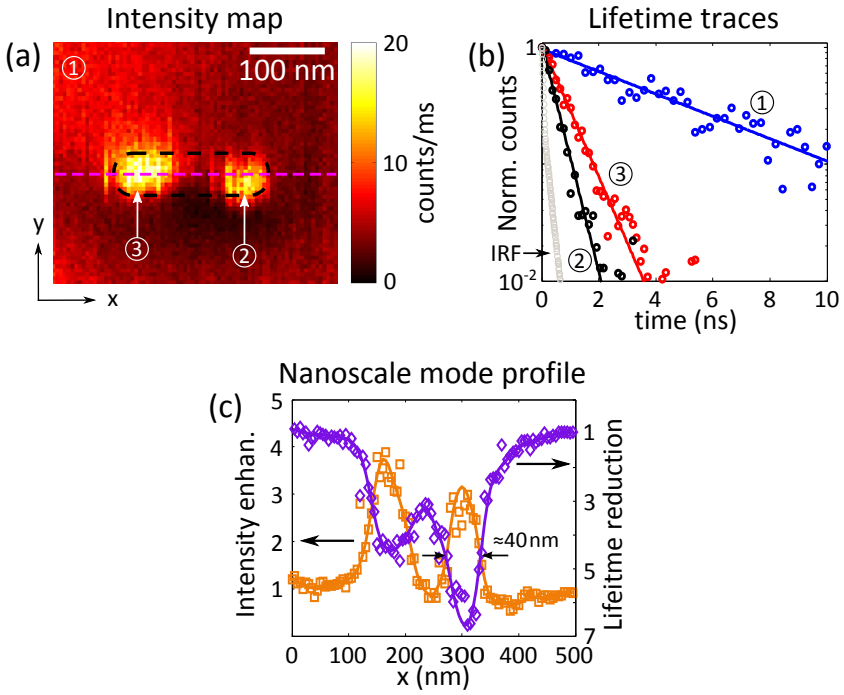

Figure 5.3: Intensity and lifetime measurements. (a) Intensity enhancement map of single molecular fluorescence as a resonant dipole nanoantenna cavity is scanned over the molecule, revealing the dipolar mode of the cavity. Dashed black outline represents the shape and geometry of the nanoantenna, which clearly shows the position of the hotspots at the nanoantenna. (b) Characteristic fluorescence decay traces (recorded during lifetime imaging) showing the molecule uncoupled (blue line) and coupled to the nanoantenna in the hotspots (red and black lines). The circles are data points and the solid lines are single exponential fits. Grey curve indicates the instrument response function (IRF) of the time-tagging detection system. (c) Line profiles along the hotspots (dashed magenta line in (a)) in the intensity and the corresponding lifetime maps show the reduction in the molecule's lifetime (purple diamonds) and the enhancement in fluorescence intensity (orange squares). The asymmetry between enhancement and intensity profiles are evident since the intensity is sensitive to the exact excitation conditions including near-field interference, while the lifetime is only sensitive to emission of the molecule through the enhanced local density of states. The solid lines are guide to the eye.

molecule and relate to the coupling strength g through (see Appendix for the derivation) [115]:

$$\frac{\Gamma_{tot}}{\Gamma_0} = \frac{4g^2}{\kappa\Gamma_0} + 1. \tag{5.1}$$

We have access to both the rates Γ_0 and Γ_{tot}, see Figure 5.3. We extract the cavity loss rate κ from the extinction spectrum of the nanoantenna (Figure 5.2b), giving $\kappa = 8.8\text{x}10^{13}$ Hz for a nanoantenna Q factor of ≈ 5 at the resonance wavelength λ_f = 680 nm. Thus, using Equation 5.1, we construct the coupling strength g-map of the molecule-nanoantenna cavity with

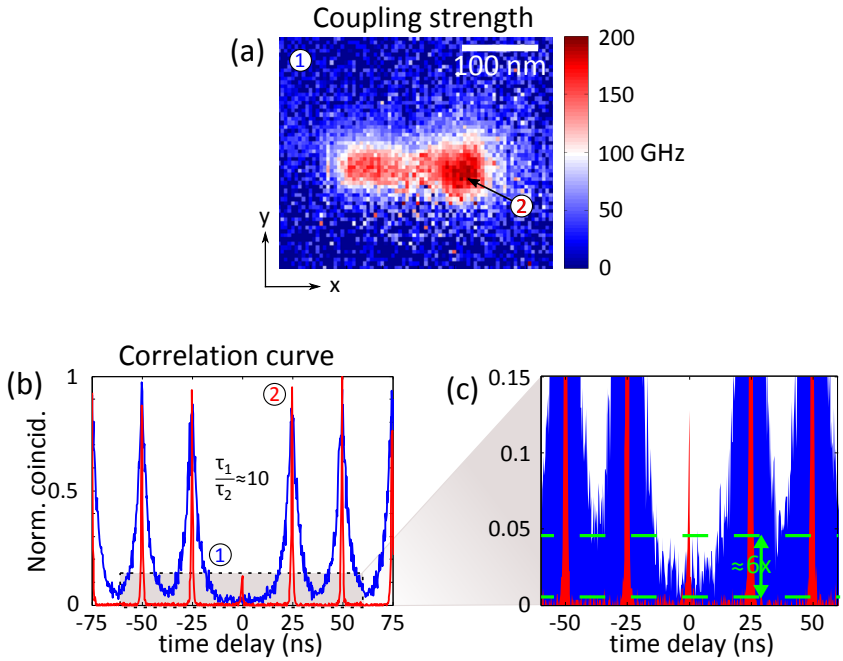

Figure 5.4: Coupling strength g-map for a single molecule in a resonant dipole nanoantenna cavity. (a) 5 nm resolution coupling strength g-map between a molecule-nanoantenna system (of Figure 5.3). The map shows $g = 0$ away from the nanoantenna cavity, and it reaches a maximum value in the hotspots of $g_{max} = 206$ GHz. The asymmetry in the g-map is a direct consequence of the angle between the molecule's dipole and nanoantenna field lines (b) Normalized second-order intensity correlations $g^2(T)$, where T is the inter-photon delay, showing antibunched photon character [$g^2(0) = 0.097 \pm 0.001$] of the single molecule (point 1, blue curve). When coupled to the nanoantenna (point 2, red curve) the molecule continues to show single photon character [$g^2(0) = 0.19 \pm 0.01$] but with a far reduced lifetime encoded in the sharper width of the correlation peaks. (c) A zoom-in into the shaded area in the correlation curve (b) shows at least 6x increase in photon separability between the two consecutive pulses, increasing the purity of the single photons. A small peak (≈10% of side peaks) appearing at zero delay for the coupled system is due to multiple excitation and emission of the molecule within an excitation pulse (see Section 5.4). For the antibunching measurement, we use 3.2 μW of laser power and an integration time of 100 s for the molecule alone and 20 s with the nanoantenna. The correlation curve is recorded with bin size of 64 ps and binned further to 256 ps.

nanometer-precision. The measured g-map between the same molecule and nanoantenna as in Figure 5.3 is shown in Figure 5.4a. The map shows value $g = 0$, where the molecule is completely de-coupled from the cavity (point 1). The value of g begins to increase as the molecule enters the mode volume of the cavity and sharply increases at the positions of maximum field density, i.e. at the hotspots. The coupling strength attains maximum value of $g_{max} = 206$ GHz, where $g \gg \Gamma_0$ (point 2).

We note that we are optimally positioned in the bad-cavity regime with high coupling strength g but with $g < \kappa$, allowing an efficient emission

of photons from the nanocavity. Since $g \gg \Gamma_0$ the statistics of the emitted photons is modified. The second-order intensity correlation function $G^2(T)$ quantifies the photon statistics, where T is delay between two consecutive photons detected from the molecule. We use the previously described HBT setup (Figure 5.2a) to record a coincidence histogram of the emitted photons, which is equivalent to $G^2(T)$ [121]. The normalized correlation function $g^2(T)$ of the molecule (alone) and molecule-nanoantenna is presented in Figure 5.4b. At zero time delay, we obtain the coincidence rate well below the classical limit $g^2(0) < 0.5$ (Figure 5.4b, blue curve 1), indicating antibunching photon arrival, proving single molecule detection. Scanning the same molecule into the hotspot of the nanoantenna (Figure 5.4a, point 2), we see a dramatic sharpening of its $g^2(T)$ statistics as it couples to the cavity, sharpest at the hotspot center (Figure 5.4b, red curve). The strong antibunching behavior is maintained in this case as well with $g^2(0)$ well below the classical limit.

This sharpening of $g^2(T)$ in the coupled case results from the 10-fold increase in the spontaneous decay rate, which generates the pulses of half-width <1 ns. This allows us to deduce that coupled single emitter-nanoantennas can be used to create bright true single photon sources with an emission rate> 1 GHz. Further details of the antibunching measurement are highlighted in Figure 5.4c, which is a zoom-in of the shaded area of Figure 5.4b. The nanoantenna induced squeezing of the pulses results in at least 6x improvement in photon separability between two consecutive pulses and therefore the system can deliver single photon per pulse with high purity at a very high repetition rate. Here, we observe a marginal peak at $T = 0$ i.e. $g^2(0)$ when the molecule is coupled to the nanoantenna. The origin of this peak attributed to multiple excitation and emission of the molecule within an excitation laser pulse due to the strong increase in its spontaneous decay rate. This creates two successive photons separated by the time less than the time resolution of the detection system, and therefore registers as a coincidence at $T = 0$. A detailed analysis of the peak at $g^2(0)$ will follow in Section 5.4.

5.2.1 *Vectorial mapping of coupling strength*

The coupling strength $g = \mathbf{p}.\mathbf{E}_s(\mathbf{r}, \omega_f)/\hbar$ depends both on position ($\mathbf{r}$) and orientation of the emitter dipole moment ($\mathbf{p}$) within the cavity mode EM field $\mathbf{E}_s(\mathbf{r}, \omega_f)$ at the emission frequency ω_f. This is evident in the asymmetry in the coupling strength between the two hotspots, where at the right spot in Figure 5.4a the molecule couples more effectively with the nanoan-

tenna due to better overlap with the dipolar mode field lines. From this we can accurately deduce the molecule's slightly off-axis orientation not possible based on solely the intensity map (Figure 5.3a), susceptible to excitation interference effects (Chapter 4). By using single molecules of two orthogonal dipole orientations with respect to the nanoantenna's long axis, we construct a vectorial picture of the coupling strength g (Figure 5.5). The vectorial nature of the dipolar mode pattern is evident especially in the case with the molecule perpendicular to the long axis and in the plane of the nanoantenna. A four-lobed g-map pattern emerges in this case, similar to the y-field intensity pattern of the resonant nanoantenna (Figure 3.3b,e). The measured g-map in Figure 5.5b exhibits an asymmetric character due to the precise molecular alignment. This is mirrored in the FDTD calculation of the g-map (Figure 5.5a), albeit showing the ideal case and thus with perfect symmetry. The out-of-plane molecule (along the z-axis) shows the more familiar dipolar two-hotspot pattern both for the measured and calculated g-maps, see Figure 5.5b,d. In this case the coupling effect is striking, as without the nanoantenna the molecular emission is barely detectable since circularly polarized light does not efficiently excite a molecule in this orientation.

The coupling is stronger in the out-of-plane than the in-plane case due to the precise nature of the cavity's orientation-dependent density of states [122]. The measured in-plane g-map has relatively higher coupling strength than the calculated one (Figure 5.5a,b) due to its mixed orientation. The estimated orientation of the molecule based on the intensity pattern (as discussed in Chapter 4) in Figure 5.5e indicates a small contribution from the out-of-plane component, which results in the higher coupling value. The measured out-of-plane g-map (Figure 5.5d) shows near-perfect symmetric pattern as the molecule oriented mainly along the z-axis, see Figure 5.5f. In this case, we use reference molecule rate 2x smaller than the perfect in-plane case to take into account the effect of the molecule's orientation on its spontaneous rate at the interface (glass-air) [123]. Based on our measurements on different molecules, the near perfect in-plane molecule rate is 0.34 GHz, therefore $\Gamma_0 = 0.5 * 0.34$ GHz is the rate of the out-of-plane molecule. The effect of the interface is taken into account for the FDTD calculations as well to provide the correct values of the coupling. The vectorial g-maps allow us to precisely optimize a single emitter's placement and its orientation to provide maximal radiative coupling to any given cavity.

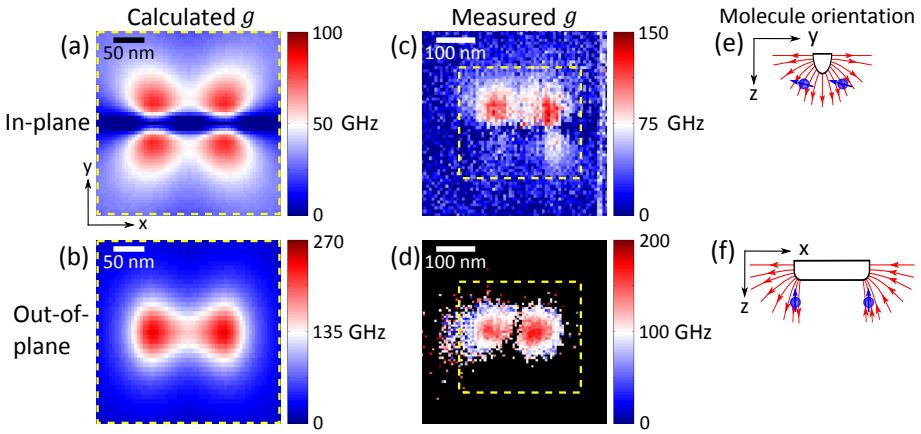

Figure 5.5: Vectorial mapping of the coupling strength. The coupling to the nanoantenna crucially depends on position as well as orientations of single molecules. FDTD calculation of g-maps with (a) the molecule's dipole aligned in the nanoantenna plane along the y-axis, perpendicular to the nanoantenna long axis. This creates a characteristic four-lobed pattern. (b) An orthogonal molecule with out-of-plane orientation (along the z-axis), showing the two-lobed dipolar pattern. The out-of-plane case exhibits higher coupling strength than in-plane case with a maximum strength goes up to 241 GHz. The coupling strength is based on the lifetime map, which is calculated at a plane 15 nm below the nanoantenna. (c, d) Measured g-maps for the in-plane and out-of-plane molecules, respectively. The g-value for the out-of-plane case is set to black (away from the nanoantenna) due to insufficient photon counts. (e, f) Orientations of the molecules (in blue) relative to the nanoantenna (solid black outline) in (c, d) respectively. A slight tilt in the molecule dipole towards (e) the z-axis is responsible for the asymmetric g-map pattern for the in-plane case as it couples more efficiently to the nanoantenna field lines (red lines with arrows) when it is on the right-hand side. The molecule is perfectly oriented along (f) the z-axis and shows a symmetric dipolar pattern (d). For the calculations, we only show the g-maps for the area of interest, marked by the dashed square (yellow).

Coupling strength vs Local density of states

The experimental determination of the coupling strength g involves both the spontaneous emission rate of the molecule and dissipation rate of the nanoantenna (see Equation 5.1). Since the nanoantenna loss rate κ is fixed once it's fabricated, change in the spontaneous rate determines the strength of the coupling. From the classical point of view, a nanoantenna when tuned to the emission frequency of an emitter can enhance the spontaneous emission rate, owing to modified local density of states (LDOS) around the emitter [63, 67, 91, 124–127]. In other words, the nanoantenna creates additional paths involving scattering from the surface which interferes with the emitter's field [128]. Quantum-mechanically all the different ways needs

to be added in which spontaneous emission may take place. Using Fermi's Golden rule, the spontaneous emission rate Γ is defined as [115, 128]:

$$\Gamma = \frac{2\pi}{\hbar^2} |\mathbf{p}.\mathbf{E}_s(\omega_f, \mathbf{r})|^2 \, D(\omega_f, \mathbf{r}) \cong g^2(\omega_f, \mathbf{r}) \, D(\omega_f, \mathbf{r}) \tag{5.2}$$

where $D(\omega_f, \mathbf{r})$ is position dependent LDOS at the transition frequency ω_f. On contrary to the common belief that the spontaneous emission rate is only depends on LDOS, the Γ is a function of both the coupling strength g and LDOS D (Equation 5.2) [23, 63, 67]. The question still remains what is the best physical description of the measurements based on modified spontaneous emission rate of the molecule when coupled to the nanoantenna. The LDOS provides the photonic states or number of probable ways in which a transition can occur between the excited and ground states. On the other hand, the coupling strength g is a physical quantity gives us the direct information about how strongly or weakly the molecule is coupled to the available LDOS. The LDOS mainly deals with the molecule alone and the change in its surroundings, whereas with g we have the complete information about the molecule-nanoantenna system. This knowledge of g quantifies the energy transfer rate between the molecule and nanoantenna, allowing us to compare different rates and predict how far is the system from reaching strong coupling ($g \gg \kappa, \Gamma_0$). In our case, the value of g is more than two orders of magnitude less than κ, which implies that a further reduction of at least four orders of magnitude in the mode volume is needed to enter into the strong coupling regime.

5.3 SINGLE PHOTONS ON DEMAND

We have seen the position and orientation dependence of the coupling strength g in for a molecule coupled to a nanoantenna. Here, we show control of the single photon emission rate depending on the molecule's position at the nanoantenna. We use a different nanoantenna scanning tip than used in the previous measurements. The intensity map of the coupled system is shown in Figure 5.6a, showing the standard two-hotspot pattern. The normalized intensity correlation curve at three different positions in the intensity map: at the two hotspots (left and right) and away from the nanoantenna (molecule alone) is shown in Figure 5.6b. A clear antibunching behavior is seen in all the three cases, proving the non-classical photon emission. The nanoantenna-induced increase in the spontaneous rate results in the pulse width shortening at the left spot (red curve) in the corre-

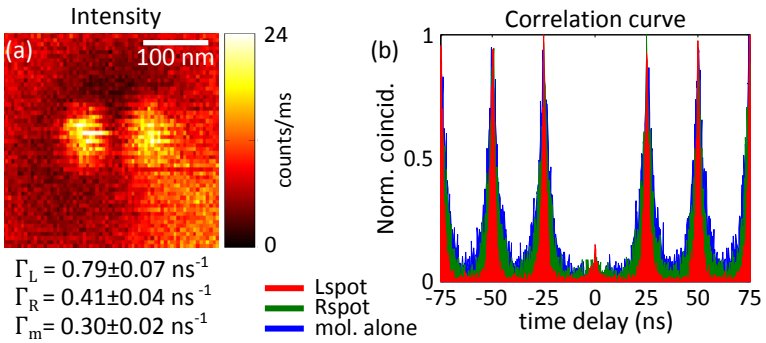

Figure 5.6: Nanoscale control of single photon rate. (a) Intensity map of a molecule-nanoantenna system, showing the typical two hotspots pattern. (b) The measured intensity correlation statistics using the HBT setup at the two hotspots, left spot (red curve) and right spot (green). The molecule shows strong antibunching behavior at the hotspots with increased spontaneous rate compared to the molecule alone (away the nanoantenna) case (blue curve). The decay rates at the three positions are Γ_L (left spot), Γ_R (right spot), and Γ_m (molecule alone). The integration time used are 300 s for Lspot, 400 s for Rspot and 700 s for the molecule alone. The correlation curves are recorded with bin size of 16 ps and binned further to 256 ps.

lation measurement (Figure 5.6b). The photons decay with slower rate when the molecule is positioned at the right hotspot, resulting in twice as broad pulse width (green curve) as at the left spot. Away from the nanoantenna, the molecule is completely uncoupled and emits single photons with a reduced rate (blue curve). By deterministically positioning of the molecule at the nanoantenna, we can tune the single photon emission rate and thus create on-demand single-photon source with a tunable rate. The orientation-dependent coupling and nanopositioning of the molecule at the nanoantenna allow us to control the single photon rates. Similar to the antibunching measurement in Figure 5.4b, we observe a small peak at the delay $\tau = 0$ for the measurement with the nanoantenna at the left hotspot. A full analysis and discussion about the origin of this central peak is performed in the following section (Section 5.4).

5.4 ANTIBUNCHING ANALYSIS OF A MOLECULE-NANOANTENNA SYSTEM

To investigate the origin of the central peak appearing at zero time delay in the normalized coincidence histograms $g^2(\tau)$ (Figure 5.4b, Figure 5.6b), we performed more experiments and theoretical simulations. The results are divided in two categories, experimental and theoretical and are as discussed below.

EXPERIMENTAL

We further analyze the antibunching measurement of the molecule-nanoantenna system (Figure 5.4) in order to determine the origin of the central peak i.e. peak at zero time delay ($T = 0$), which has an amplitude of 10-20 % with respect to the side peaks at other delays. Photoluminescence of the metal (aluminum) nanoantenna can be one of the possible reasons as the luminescence photons have extremely short lifetimes with sub-picosecond time dynamics and do not show antibunching behavior, which seems to be the characteristics of the central peak [129]. In order to verify this, we performed antibunching measurement on a similar resonant nanoantenna alone without any molecule using the same excitation wavelength and input power (λ=633 nm at 3.2 μW) we used in Figure 5.4b. The recorded coincidence histogram of the nanoantenna is shown in Figure 5.7b, and has negligible coincidences even for higher integration time. This is in striking contrast with the molecule-nanoantenna system (Figure 5.7a), where the central peak has around 30 coincidences for 20 seconds integration time.

To obtain any substantial coincidences, we excite the nanoantenna with 100x more power (300 μW) at 532 nm. The comparison of the normalized coincidence histogram at $T = 0$, i.e. $g^2(0)$ of the two systems is shown in Figure 5.7c. The nanoantenna luminescence has a much narrower peak width (limited by the instrument response function) than the molecule-nanoantenna system. Moreover, the central peak of the system has the same width as its peak at other delay time (e.g. at $T = 25$ ns in Figure 5.7c), which shows the central peak exhibits molecular decay dynamics. Thus, we can conclude that the small peak at $g^2(0)$ (Figure 5.7a) is not due the luminescence of the nanoantenna and comes from the molecule itself when coupled to the nanoantenna.

We performed the correlation measurements on 20 different molecules when coupled to the resonant nanoantenna. We plot the measured $g^2(0)$ as a function of the lifetime obtained from the correlation curves, see Figure 5.8. The values of $g^2(0)$ is obtained with respect to the mean of all the side peaks. Similarly, the lifetime values are extracted by fitting the correlation curves and taking the mean lifetime values of all the peaks excluding the peak at zero. As seen in Figure 5.8, a sharp rise in $g^2(0)$ is accompanied by a decrease in the mean lifetime. This behavior implies that the probability of detecting two photons simultaneously increases on coupling to the nanoantenna. These two emitted photons are separated by a time less than the resolution of our detection system (30-40 ps) and therefore the two APDs register photons at the same time to give coincidences at time zero.

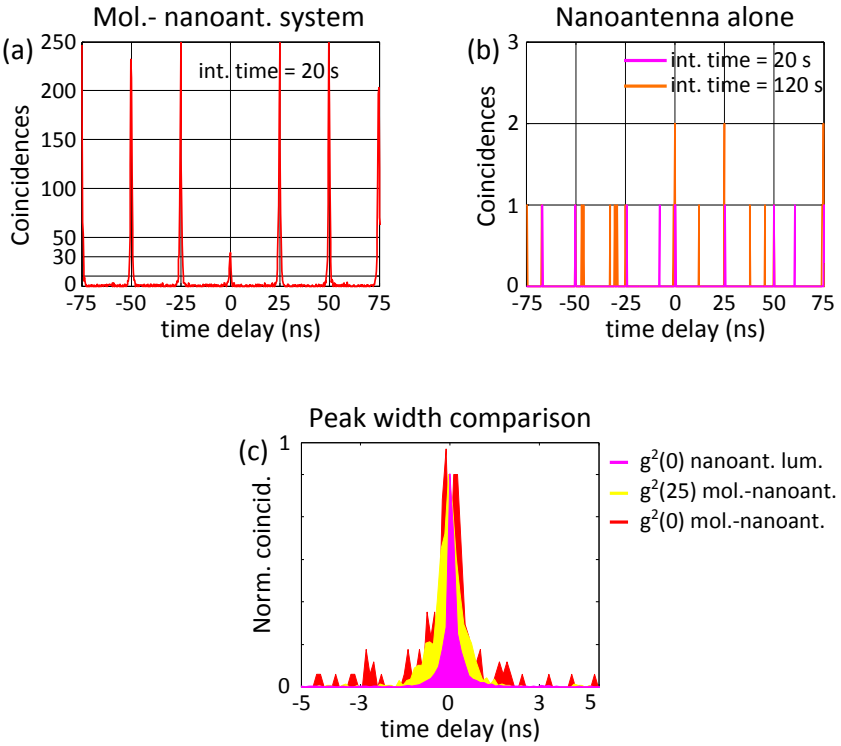

Figure 5.7: Intensity correlation comparison of the nanoantenna luminescence with the molecule-nanoantenna system. Coincidence histograms for (a) the molecule-nanoantenna system shows ≈30 coincidence at zero delay for 20 seconds integration time, however (b) the nanoantenna only has negligible coincidences for integration times of 20 and 120 seconds. Both the curves are obtained for the same experimental conditions (λ = 633 nm at 3.2 μW), and we use the same bin size of 256 ps. (c) Peak width comparison of $g^2(0)$ for obtained luminescence at 100x more power at 532 nm with the $g^2(0)$ and $g^2(25)$ of (a). It shows that the luminescence has a much narrower peak (magenta curve), in contrast with the molecule-nanoantenna system (red or yellow curve), while the small peak at zero delay (red curve) has the same decay dynamics as other time delays (T = 25 ns, yellow curve).

Similar behavior has been observed with single quantum dots coupled to a microcavitiy [130, 131] and metal nanoparticles [132], where the effect is either attributed to radiative recombination of biexcitions, capturing of a second electron-hole pair from the substrate, or multiple excitations of the quantum dot within a single excitation pulse.

Since we are using single molecules in our experiments, the possibility of biexcition recombination and other related mechanisms can be ruled out. However, we cannot completely preclude the multiple excitation-emission events within a pulse as we use a laser with the pulse width of few tens of picoseconds. Furthermore, this process will give a central peak dynamics similar to the molecule decay. The lifetime distribution of a molecule has a high probability of photons arriving at very short times just after the excitation within few ps (Figure 5.3b). This probability increases further upon

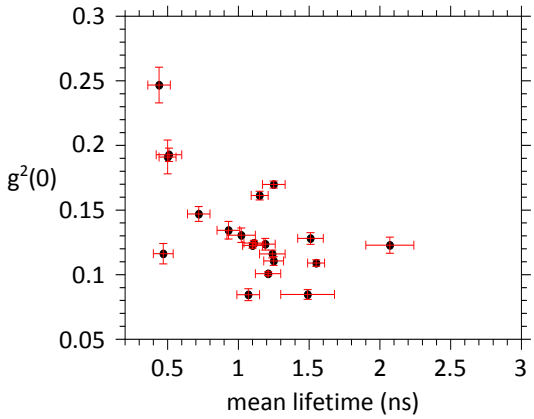

Figure 5.8: Lifetime dependence of the central peak. The values of $g^2(0)$ increase as the mean lifetime values of molecules decreases on coupling to the nanoantenna.

coupling to the resonant nanoantenna, which enhances the excitation and emission rate of the molecule manyfold. Thus, the probability of more than one excitation and emission events per pulse goes up. Due to the finite time resolution of the detection system the two photons produce a coincidence, which can artificially add to the impurity of the single photons.

THEORETICAL

To further investigate and quantify the re-pumping mechanism, we performed numerical simulations to obtain the normalized second-order intensity correlation function $g^2(T)$ as a function of delay T. The $g^2(T)$ is proportional to probability density $P(T)$, the probability of detecting a (stop) photon at time $t+T$ given that there was a (start) photon at time t. For a cw (stationary) excitation, an analytical solution of $P(T)$ can be obtained directly from the rate equations, which gives the probability of finding the molecule in the ground or excited state [121]. However, for a time dependent pulse excitation, the probability of both the start and stop photons becomes a function of time and no analytical solution can be obtained. Therefore, the rate equations are numerically solved to first find the time dependent probability of having a start photon. Then, by considering a specific start photon at time t, the delay dependent probability of finding the next photons is calculated using the rate equations. In this case, the $P(T)$ is obtained by multiplying both the probabilities and integrating over all the start photon possibilities. In the calculations, we use a time dependent pulse excitation with a Gaussian temporal profile (FWHM = 40 ps) and repetition rate of 40 MHz same as the experiment. All the other parameters used in the simulations are similar to the ones used during the experiments

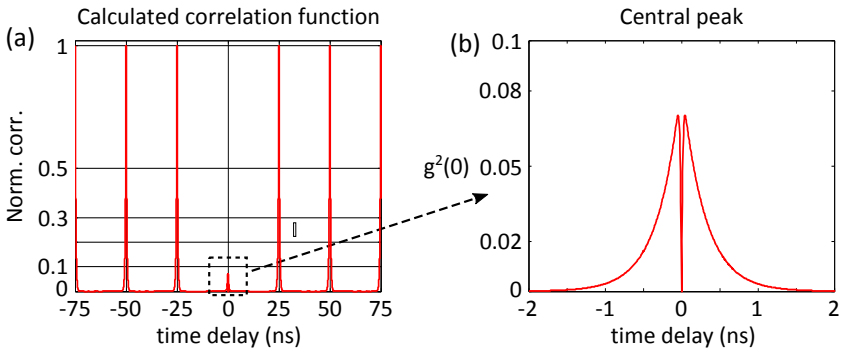

Figure 5.9: Numerical simulation for second-order correlation function. (a) Normalized correlation function for a Gaussian excitation pulse width of 40 ps, a peak excitation rate of 10 GHz and lifetime of 300 ps. The correlation function shows a small peak at zero delay which is <10 % of the side peaks, similar to the experiment. (b) The zoom of the central peak, showing a clear antibunching behavior with $g^2(0) = 0$ as we have enough time resolution (5 ps) in the calculation.

giving a peak excitation rate around 10 GHz, which includes the excitation enhancement by the nanoantenna.

Figure Figure 5.9a shows $g^2(T)$ for a lifetime value of 300 ps (similar to the values in the experiments). The plot shows a small peak at zero delay with a magnitude of <10 % relative to the side peaks, similar to the measured value of $g^2(0)$. However, a clear antibunching behavior i.e. $g^2(0) = 0$ can be seen when zooming in on the central peak (Figure 5.9b). The time resolution of 5 ps allows us to just barely see the true antibunching behavior, which is not possible to observe in the experiments due the limited time response of the APDs and TCSPC. The symmetric rising of $g^2(T)$ close to the zero delay is similar to the one observed in cw antibunching experiments, dependent on the excitation and emission rate. Here, the excitation rate becomes very high within the pulse and causes the fast rising whereas the falling edge is governed by the emission rate.

We also study the dependence of $g^2(0)$ on other parameters such as lifetime, pulse width, and peak excitation rate. The results are shown in Figure 5.10. The lifetime values are varied between 100 and 700 ps while keeping the pulse width of 40 ps and the peak excitation rate of 10 GHz (Figure 5.10a). A trend similar to the measured values (Figure 5.8) is observed where a decrease in the lifetimes results in a sharp increase in $g^2(0)$ values (Figure 5.10a). Moreover, we see an increase in the $g^2(0)$ as the pulse becomes broader with a fixed lifetime (Figure 5.10b). This trend directly hints towards the possibility of multiple excitation-emission events within the same pulse. To take into consideration any eventual uncertainty in our estimation of the excitation rate, we vary the peak excitation rate from 2-20 GHz while keeping the pulse width of 40 ps and lifetime of 300 ps. As we

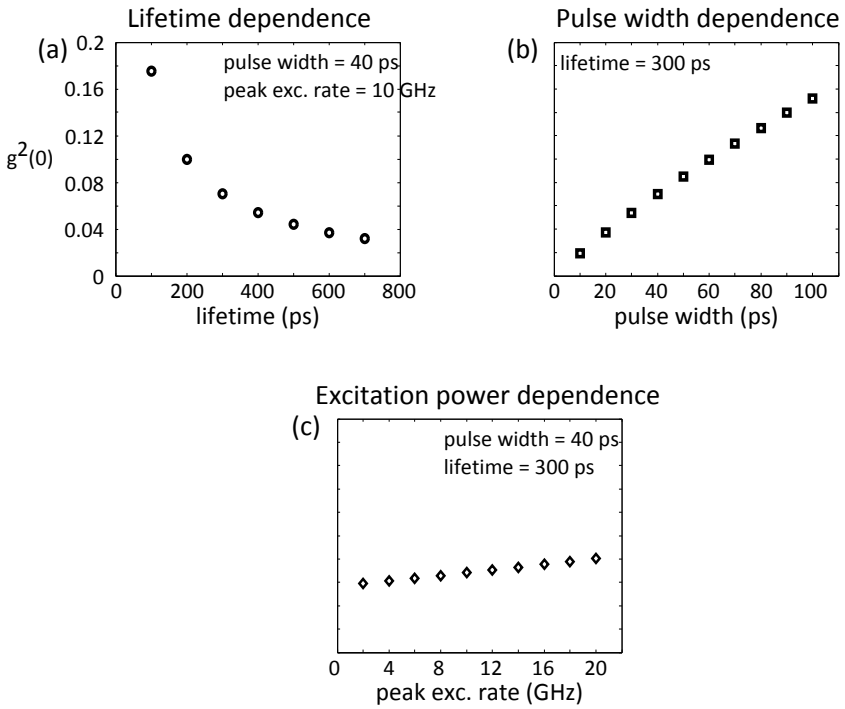

Figure 5.10: The dependence of $g^2(0)$ on (a) the emitter's lifetime, (b) the laser's pulse width, and (c) the excitation power. A decrease in the lifetime causes a sharp increase in the $g^2(0)$, as was observed experimentally. Increases in the pulse width also show an increase in $g^2(0)$, which is expected as wider pulse widths increase the likelihood of multiple excitation-emission events within the same pulse. Only a very small increase is observed in $g^2(0)$ with 10x increase in the power. All the curves has the same y-axis (extreme left).

see in Figure 5.10c, $g^2(0)$ increases very slowly with the peak excitation rate, confirming our calculations. Based on the measurements and calculations of the photon antibunching, the re-pumping mechanism seems to be the most probable cause of the appearance of the central peak. It can be considered as an artifact of the detection system, which does not inherently reduce the purity of the single photon source.

5.5 CONCLUSION

To summarize, we map the coupling strength g between a sub-wavelength sized lossy nanocavity and single molecules of different orientations with nanometer precision to characterize the full vectorial nature of the coupling strength. The coupling strength maps reveal information not available in traditional intensity maps and precise details not available from calculations. The measured QED parameters for our nanoantenna cavity are $(2g, \kappa, \Gamma_0) = (4.1\text{x}10^{11}, 880\text{x}10^{11}, 2.1\text{x}10^{8})$ Hz. We show that plasmonic nanoantenna cav-

ities coupled to single photon emitters are optimal for use as super-bright and pure single photon sources. We highlight the importance of precise emitter positioning and orientation to maximize coupling to the nanocavity, and thus photon emission rate, while remaining in the bad-cavity regime. Such ultra-compact and directional single photon sources are compatible with integrated photonic devices, thus providing new opportunities for all-optical quantum computing.

CONCLUSION AND OUTLOOK

In all the experiments in this thesis, resonant dipole nanoantennas were fabricated at the end of a fiber tip and brought in to the close vicinity of molecules using a near-field microscope. This allowed us to form single molecule-nanoantenna system with the full nanopositioning and orientation control.

Using this system, we have shown the full characterization of the vectorial near-field of the nanoantenna by choosing specific molecule's orientations. Using these molecules, we were able to quantify the relative strength of the different field components of the nanoantenna and their spatial structure at nanometer resolution. We showed that the nanoantenna has the strongest enhancement for out-of-plane molecules while in-plane molecules are weaker in strength. Using the dipole nanoantenna, we showed the emission control of the single molecule polarizations through degree of linear polarization maps.

The correct knowledge of the vectorial near-field of a nanoantenna is essential to fully understand important concepts such as the local interference they, which can unveil interesting applications. We experimentally demonstrated and explained for the first time this local interference effect. The local interference allows external control over the near-field distribution of the nanoantennas, and can be exploited to shape the nanoantenna field as desired. We have shown an example where the position of the hotspots can be moved at the nanoantenna by changing the polarization state of the excitation field.

We have shown unprecedented nanoprecision control and understanding of the interaction between plasmonic nanoantenna cavities and single photon emitters. We mapped the coupling strength g with nanometer precision, and showed remarkable control over the coupling strength g as a function of position of a single molecule within the nanoscale mode volume of a nanoantenna. By mapping and optimizing the three-dimensional position and orientation of a single molecule relative to the nanoantenna, we maximized this coupling strength ($g_{max} = 206$ GHz) to enhance the molecule's spontaneous emission rate, to create super-bright and pure single photon sources with repetition rates> 1 GHz.

The work presented in this thesis has important implications in the field of nanophotonics, where a lot of emphasis is on developing ultra-compact

photonics devices. Plasmonic nanoantennas are certainly the ideal candidate for such devices due to their sub-wavelength size and ability to control light at nanoscale. The full vectorial near-field characterization improves our understanding of nanoantennas functionality, thus facilitate their use in applications. The local interference gives us another exciting possibilities to externally control the local field at the nanoantennas with applications such as directional switching and selective excitation of single emitters.

The high losses (mainly radiative) of plasmonic nanoantennas have restricted their use in cavity QED experiments, which rely on high Q factors cavities to attain large coupling strengths. However, in this thesis, we showed that plasmonic nanocavities with deeply sub-wavelength mode volumes, can create high coupling strengths, at strengths far higher than the spontaneous emission rate of single molecules. A further reduction in the mode volume, using different nanoantenna designs, can allows us to reach even higher g values, which can lead eventually into the strong-coupling regime. As we pointed out in this thesis, the optimal positioning of an emitter into this mode volume is crucial to profit from this large g and necessary to maintain high photon output. Entering into the strong coupling regime with plasmonic resonators will produce the photon decay rate of tens of femtoseconds, which could allow us to study interesting quantum processes such as dephasing of single photon emitters at room-temperature.

APPENDIX

DERIVATION OF THE COUPLING STRENGTH

Here we derive coupling strength g between an optical resonator such as nanoantenna cavities and a single photon emitter such as single molecules. We only show the equations relevant to extract g using the measured decay rate of the molecule in both uncoupled and coupled cases. We follow the formalism from reference [115], a standard text-book in the field of quantum-optics.

The coupling strength g quantifies the rate of energy transfer between an emitter and a cavity. Under the dipole approximation, we can express the coupling strength as a projection of the emitter's dipole $\mathbf{p}$ over the local electromagnetic (EM) field $\mathbf{E}_s$ [16, 22]:

$$g(\mathbf{r}, \omega_a) = -\frac{\mathbf{p}.\mathbf{E}_s(\mathbf{r}, \omega_a)}{\hbar} = -\frac{|\mathbf{p}.\widehat{\mathbf{E}}_s|}{\hbar}\sqrt{\frac{\hbar\omega_a}{2\epsilon_0 V_m(\mathbf{r})}}, \tag{A.1}$$

where ω_a is the central frequency of the cavity, V_m is the cavity mode volume, $\mathbf{r}$ is the position of the emitter, and $\mathbf{E}_s$ is the sum of all the EM modes available for the molecule to decay through. ϵ_0 and $\hbar$ are the vacuum permittivity and reduced Planck's constant, respectively.

We want to compare g with other decay mechanisms of the system. The two main additional decay mechanisms are: (1) Direct emission of the molecule into free-space (Γ_0) and (2) Irreversible damping of the cavity mode to the environment (κ_0), which is a consequence of the plasmon decay due to both ohmic losses as well as radiation losses. Thus, the total decay rate of an emitter coupled to the resonator (Γ_{tot}) has contribution from both Γ_0 and the nanoantenna (Γ_{ant}) decay channels:

$$\Gamma_{tot} = \Gamma_0 + \Gamma_{ant}. \tag{A.2}$$

In the weak coupling regime ($g \ll \kappa, \Gamma_0$), the contribution of the nanoantenna cavity to the total decay rate can be expressed as [14, 115]:

$$\Gamma_{ant} = \left(\frac{4g^2}{\kappa}\right) \frac{1}{1 + (2\delta/\kappa)^2}, \tag{A.3}$$

where $\delta = \omega_a - \omega_f$ is the detuning between the resonance frequencies of the nanoantenna and molecule (ω_f). At resonance ($\delta = 0$) Equation A.3 reduces to:

$$\Gamma_{ant} = \frac{4g^2}{\kappa}, \tag{A.4}$$

representing the relation between the coupling strength g and decay rate of the molecule through the nanoantenna mode. Using Equation A.2, we can rearrange Equation A.3 as:

$$\frac{\Gamma_{tot}}{\Gamma_0} = \frac{4g^2}{\kappa\Gamma_0} + 1 = F_p. \tag{A.5}$$

which is equivalent to Purcell factor (F_p). Thus, the coupling strength in terms of the measured rates is given by:

$$g(\mathbf{r}, \omega_a) = \sqrt{\frac{(\Gamma_{tot} - \Gamma_0)\kappa}{4}}. \tag{A.6}$$

For the nanoantenna, we have estimated the quality factor Q of the resonance, from which we can obtain the cavity losses κ using $Q = \omega_a/\kappa$. In our experiments, we measure the excited state lifetime of single molecules while scanning the nanoantenna over it. Having direct access to Γ_0 (uncoupled part) and Γ_{tot} when coupled to the nanoantenna as a function of the relative position $\mathbf{r}$, for one and the same molecule, it is straightforward to calculate the coupling strength g from Equation A.6.

PUBLICATIONS

The chapters of this thesis are based on the following publications:

- A. Singh, G. Calbris, J. T. Hugall, and N. F. van Hulst, *Shaping the near-field of a nanoantenna using interference*. In preparation, 2016.
- A. Singh, P. de Roque, G. Calbris, J. T. Hugall, and N. F. van Hulst, *Nanoantennas for cavity QED: Nanoscale control of coupling strength* g *for bright single photon sources*. Submitted, 2016.
- A. Singh, J. T. Hugall, G. Calbris, and N. F. van Hulst, *Fiber-based Optical Nanoantennas for Single Molecule Imaging and Sensing*. J. Lightwave Technol. 33, 2371, 2015.
- A. Singh, G. Calbris, and N. F. van Hulst, *Vectorial Nanoscale Mapping of Optical Antenna Fields by Single Molecule Dipoles*. Nano Lett. 14, 4715, 2014.

BIBLIOGRAPHY

1. Knill, E, Laflamme, R & Milburn, G. J. A scheme for efficient quantum computation with linear optics. *Nature* **409,** 46–52 (2001).
2. Lounis, B & Moerner, W. E. Single photons on demand from a single molecule at room temperature. *Nature* **407,** 491–493 (2000).
3. Gisin, N., Ribordy, G., Tittel, W. & Zbinden, H. Quantum cryptography. *Rev. Mod. Phys.* **74,** 145–195 (2002).
4. Lounis, B. & Orrit, M. Single-photon sources. *Reports Prog. Phys.* **68,** 1129–1179 (2005).
5. Ates, S., Agha, I., Gulinatti, A., Rech, I., Rakher, M. T., Badolato, A. & Srinivasan, K. Two-photon interference using background-free quantum frequency conversion of single photons emitted by an InAs quantum dot. *Phys. Rev. Lett.* **109,** 147405 (2012).
6. Schulte, C. H. H., Hansom, J., Jones, A. E., Matthiesen, C., Le Gall, C. & Atatüre, M. Quadrature squeezed photons from a two-level system. *Nature* **525,** 222–225 (2015).
7. Buttler, W. T., Hughes, R. J., Kwiat, P. G., Luther, G. G., Morgan, G. L., Nordholt, J. E., Peterson, C. G. & Simmons, C. M. Free-space quantum-key distribution. *Phys. Rev. A* **57,** 2379–2382 (1998).
8. Kwiat, P. G., Waks, E., White, A. G., Appelbaum, I. & Eberhard, P. H. Ultrabright source of polarization-entangled photons. *Phys. Rev. A* **60,** R773 (1999).
9. Michler, P, Imamoglu, A, Mason, M., Carson, P., Strouse, G. & Buratto, S. Quantum correlation among photons from a single quantum dot at room temperature. *Nature* **406,** 968–970 (2000).
10. Kimble, H. J. and Dagenais, M. and Mandel, L. Photon antibunching in resonance fluorescence. *Phys. Rev. Lett.* **39,** 691–695 (1977).
11. Kurtsiefer, C., Mayer, S., Zarda, P. & Weinfurter, H. Stable Solid-State Source of Single Photons. *Phys. Rev. Lett.* **85,** 290–293 (2000).
12. Purcell, E. M. Spontaneous emission probabilities at radio frequencies. *Phys. Rev.* **69,** 681 (1946).
13. Goy, P., Raimond, J. M., Gross, M. & Haroche, S. Observation of cavity-enhanced single-atom spontaneous emission. *Phys. Rev. Lett.* **50,** 1903–1906 (1983).

14. Kimble, H. J. Strong Interactions of Single Atoms and Photons in Cavity QED. *Phys. Scr.* **T76,** 127–137 (1998).

15. Vahala, K. J. Optical microcavities. *Nature* **424,** 839–846 (2003).

16. Miller, R, Northup, T. E., Birnbaum, K. M., Boca, a, Boozer, a. D. & Kimble, H. J. Trapped atoms in cavity QED: coupling quantized light and matter. *J. Phys. B At. Mol. Opt. Phys.* **38,** S551–S565 (2005).

17. McKeever, J., Boca, A., Boozer, A. D., Miller, R., Buck, J. R., Kuzmich, A. & Kimble, H. J. Deterministic Generation of Single Photons from One Atom Trapped in a Cavity. *Science (80-.).* **303,** 1992 (2004).

18. Agio, M. Optical antennas as nanoscale resonators. *Nanoscale* **4,** 692–706 (2012).

19. Schuller, J. A., Barnard, E. S., Cai, W., Jun, Y. C., White, J. S. & Brongersma, M. L. Plasmonics for extreme light concentration and manipulation. *Nat. Mater.* **9,** 193–204 (2010).

20. Chikkaraddy, R., Nijs, B. D., Benz, F., Barrow, S. J., Scherman, O. A. & Fox, P. Single-molecule strong coupling at room temperature in plasmonic nanocavities. *Nature* **535,** 127–130 (2016).

21. Pelton, M. Modified spontaneous emission in nanophotonic structures. *Nat. Photonics* **9,** 427–435 (2015).

22. Tame, M. S., McEnery, K. R., Ozdemir, S. K., Lee, J, Maier, S. a. & Kim, M. S. Quantum plasmonics. *Nat. Phys.* **9,** 329–340 (2013).

23. Anger, P., Bharadwaj, P. & Novotny, L. Enhancement and Quenching of Single-Molecule Fluorescence. *Phys. Rev. Lett.* **96,** 113002 (2006).

24. Mertens, H., Koenderink, A. F. & Polman, A. Plasmon-enhanced luminescence near noble-metal nanospheres: Comparison of exact theory and an improved Gersten and Nitzan model. *Phys. Rev. B - Condens. Matter Mater. Phys.* **76,** 115123 (2007).

25. Castanié, E, Boffety, M & Carminati, R. Fluorescence quenching by a metal nanoparticle in the extreme near-field regime. *Opt. Lett.* **35,** 291–293 (2010).

26. Moerner, W. E. Microscopy beyond the diffraction limit using actively controlled single molecules. *J. Microsc.* **246,** 213–220 (2012).

27. Balanis, C. A. *Antenna Theory: Analysis and Design* 3rd, 1136 (John Wiley & Sons, 2012).

28. Novotny, L. Effective Wavelength Scaling for Optical Antennas. *Phys. Rev. Lett.* **98,** 266802 (2007).

29. Mühlschlegel, P, Eisler, H.-J., Martin, O. J. F., Hecht, B & Pohl, D. W. Resonant optical antennas. *Science (80-.).* **308,** 1607–1609 (2005).

30. Greffet, J.-J. Applied physics. Nanoantennas for light emission. *Science* **308,** 1561–1563 (2005).

31. Novotny, L. & van Hulst, N. Antennas for light. *Nat. Photonics* **5,** 83–90 (2011).

32. Biagioni, P., Huang, J.-S. & Hecht, B. Nanoantennas for visible and infrared radiation. *Reports Prog. Phys.* **75,** 024402 (2012).

33. Betzig, E & Chichester, R. J. Single molecules observed by near-field scanning optical microscopy. *Science (80-.).* **262,** 1422–1425 (1993).

34. Veerman, J. A., Garcia-Parajo, M. F., Kuipers, L & van Hulst, N. F. Single molecule mapping of the optical field distribution of probes for near-field microscopy. *J. Microsc.* **194,** 477–482 (1999).

35. Ma, Z., Gerton, J. M., Wade, L. A. & Quake, S. R. Fluorescence near-field microscopy of DNA at Sub-10A nm resolution. *Phys. Rev. Lett.* **97,** 260801 (2006).

36. Höppener, C. & Novotny, L. Antenna-based optical imaging of single Ca2+ transmembrane proteins in liquids. *Nano Lett.* **8,** 642–646 (2008).

37. Van Zanten, T. S., Cambi, A., Koopman, M., Joosten, B., Figdor, C. G. & Garcia-Parajo, M. F. Hotspots of GPI-anchored proteins and integrin nanoclusters function as nucleation sites for cell adhesion. *Proc. Natl. Acad. Sci. U. S. A.* **106,** 18557–18562 (2009).

38. Mivelle, M., van Zanten, T. S. & Garcia-Parajo, M. F. Hybrid photonic antennas for subnanometer multicolor localization and nanoimaging of single molecules. *Nano Lett.* **14,** 4895–4900 (2014).

39. Singh, A., Hugall, J. T., Calbris, G & van Hulst, N. F. Fiber-based Optical Nanoantennas for Single Molecule Imaging and Sensing. *J. Light. Technol.* **33,** 2371–2377 (2015).

40. Nie, S & Emory, S. R. Probing single molecules and single nanoparticles by surface-enhanced Raman scattering. *Science (80-.).* **275,** 1102–1106 (1997).

41. Hugall, J. T., Baumberg, J. J. & Mahajan, S. Surface-enhanced Raman spectroscopy of CdSe quantum dots on nanostructured plasmonic surfaces. *Appl. Phys. Lett.* **95,** 141111 (2009).

42. Kawata, S., Inouye, Y. & Verma, P. Plasmonics for near-field nano-imaging and superlensing. *Nat. Photonics* **3,** 388–394 (2009).

43. Schuck, P. J., Fromm, D. P., Sundaramurthy, A., Kino, G. S. & Moerner, W. E. Improving the Mismatch between Light and Nanoscale Objects with Gold Bowtie Nanoantennas. *Phys. Rev. Lett.* **94,** 017402 (2005).

44. Castro-Lopez, M., Brinks, D., Sapienza, R. & van Hulst, N. F. Aluminum for nonlinear plasmonics: resonance-driven polarized luminescence of Al, Ag, and Au nanoantennas. *Nano Lett.* **11,** 4674–8 (2011).

45. Thyagarajan, K., Rivier, S., Lovera, A. & Martin, O. J. Enhanced second-harmonic generation from double resonant plasmonic antennae. *Opt. Express* **20,** 12860 (2012).

46. Tang, L., Kocabas, S. E., Latif, S., Okyay, A. K., Ly-Gagnon, D.-S., Saraswat, K. C. & Miller, D. A. B. Nanometre-scale germanium photodetector enhanced by a near-infrared dipole antenna. *Nat. Photonics* **2,** 226–229 (2008).

47. Bharadwaj, P., Anger, P. & Novotny, L. Nanoplasmonic enhancement of single-molecule fluorescence. *Nanotechnology* **18,** 044017 (2006).

48. Yi Fu and Joseph R. Lakowicz. Modification of single molecule fluorescence near metallic nanostructures. *Laser Photon. Rev.* **3,** 221–232 (2009).

49. Jain, P. K., Huang, X., El-Sayed, I. H. & El-Sayed, M. A. Noble metals on the nanoscale: Optical and photothermal properties and some applications in imaging, sensing, biology, and medicine. *Acc. Chem. Res.* **41,** 1578–1586 (2008).

50. Anker, J., Hall, W., Lyandres, O & Shah, N. Biosensing with plasmonic nanosensors. *Nat. Mater.* **7,** 442 –453 (2008).

51. Quidant, R. & Kreuzer, M. Biosensing: plasmons offer a helping hand. *Nat. Nanotechnol.* **5,** 762–763 (2010).

52. Novotny, L. & Hecht, B. *Principles of Nano-Optics* 1st, 539 (Cambridge University Press, 2006).

53. Dorfmüller, J, Vogelgesang, R & Weitz, R. Fabry-Pérot resonances in one-dimensional plasmonic nanostructures. *Nano Lett.* **9,** 2372–2377 (2009).

54. Kollmann, H., Piao, X., Esmann, M. & Becker, S. Toward Plasmonics with Nanometer Precision: Nonlinear Optics of Helium-Ion Milled Gold Nanoantennas. *Nano Lett.* **14,** 4778–4784 (2014).

55. Kinkhabwala, A., Yu, Z., Fan, S., Avlasevich, Y., Müllen, K. & Moerner, W. E. Large single-molecule fluorescence enhancements produced by a bowtie nanoantenna. *Nat. Photonics* **3,** 654–657 (2009).

56. Wientjes, E., Renger, J., Curto, A. G., Cogdell, R. & van Hulst, N. F. Strong antenna-enhanced fluorescence of a single light-harvesting complex shows photon antibunching. *Nat. Commun.* **5,** 4236 (2014).

57. Akselrod, G. M., Argyropoulos, C., Hoang, T. B., Ciracì, C., Fang, C., Huang, J., Smith, D. R. & Mikkelsen, M. H. Probing the mechanisms of large Purcell enhancement in plasmonic nanoantennas. *Nat. Photonics* **8,** 835–840 (2014).

58. Curto, A. G., Volpe, G., Taminiau, T. H., Kreuzer, M. P., Quidant, R. & van Hulst, N. F. Unidirectional emission of a quantum dot coupled to a nanoantenna. *Science (80-.).* **329,** 930–933 (2010).

59. Sapienza, L., Davanço, M., Badolato, A. & Srinivasan, K. Nanoscale optical positioning of single quantum dots for bright and pure single-photon emission. *Nat. Commun.* **6,** 7833 (2015).

60. Curto, A. G., Taminiau, T. H., Volpe, G., Kreuzer, M. P., Quidant, R. & van Hulst, N. F. Multipolar radiation of quantum emitters with nanowire optical antennas. *Nat. Commun.* **4,** 1750 (2013).

61. Punj, D., Mivelle, M., Moparthi, S. B., van Zanten, T. S., Rigneault, H., van Hulst, N. F., García-Parajó, M. F. & Wenger, J. A plasmonic 'antenna-in-box' platform for enhanced single-molecule analysis at micromolar concentrations. *Nat. Nanotechnol.* **8,** 512–516 (2013).

62. Sandoghdar, V & Mlynek, J. Prospects of apertureless SNOM with active probes. *J. Opt. A Pure Appl. Opt.* **1,** 523–530 (1999).

63. Kühn, S., Hakanson, U., Rogobete, L. & Sandoghdar, V. Enhancement of Single-Molecule Fluorescence Using a Gold Nanoparticle as an Optical Nanoantenna. *Phys. Rev. Lett.* **97,** 017402 (2006).

64. Taminiau, T. H., Stefani, F. D., Segerink, F. B. & van Hulst, N. F. Optical antennas direct single-molecule emission. *Nat. Photonics* **2,** 234–237 (2008).

65. Novotny, L. From near-field optics to optical antennas. *Phys. Today* **64,** 47–52 (2011).

66. Michaelis, J, Hettich, C, Mlynek, J & Sandoghdar, V. Optical microscopy using a single-molecule light source. *Nature* **405,** 325–8 (2000).

67. Frimmer, M., Chen, Y. & Koenderink, A. Scanning Emitter Lifetime Imaging Microscopy for Spontaneous Emission Control. *Phys. Rev. Lett.* **107,** 123602 (2011).

68. Ghenuche, P., Cherukulappurath, S., Taminiau, T. H., van Hulst, N. F. & Quidant, R. Spectroscopic Mode Mapping of Resonant Plasmon Nanoantennas. *Phys. Rev. Lett.* **101,** 116805 (2008).

69. Knight, M. W., Liu, L., Wang, Y., Brown, L., Mukherjee, S., King, N. S., Everitt, H. O., Nordlander, P. & Halas, N. J. Aluminum plasmonic nanoantennas. *Nano Lett.* **12,** 6000–6004 (2012).

70. Langhammer, C., Schwind, M., Kasemo, B. & Zoric, I. Localized surface plasmon resonances in aluminum nanodisks. *Nano Lett.* **8,** 1461–1471 (2008).

71. Tseng, A. A. Recent developments in nanofabrication using focused ion beams. *Small* **1,** 924–939 (2005).

72. Taminiau, T. H., Moerland, R. J., Segerink, F. B., Kuipers, L. & van Hulst, N. F. Lambda/4 resonance of an optical monopole antenna probed by single molecule fluorescence. *Nano Lett.* **7,** 28–33 (2007).

73. Mivelle, M., van Zanten, T. S., Neumann, L., van Hulst, N. F. & Garcia-Parajo, M. F. Ultrabright Bowtie Nanoaperture Antenna Probes Studied by Single Molecule Fluorescence. *Nano Lett.* **12,** 5972–5978 (2012).

74. Fromm, D. P., Sundaramurthy, A., Kinkhabwala, A., Schuck, P. J., Kino, G. S. & Moerner, W. E. Exploring the chemical enhancement for surface-enhanced Raman scattering with Au bowtie nanoantennas. *J. Chem. Phys.* **124,** 61101 (2006).

75. Hein, S. M. & Giessen, H. Tailoring Magnetic Dipole Emission with Plasmonic Split-Ring Resonators. *Phys. Rev. Lett.* **111,** 026803 (2013).

76. Hancu, I. M., Curto, A. G., Castro-López, M., Kuttge, M. & van Hulst, N. F. Multipolar interference for directed light emission. *Nano Lett.* **14,** 166–171 (2014).

77. Huttunen, M. & Andriano, D. Three-dimensional winged nanocone optical antennas. *Opt. Lett.* **39,** 3686–3689 (2014).

78. Neumann, L., van 't Oever, J. & van Hulst, N. F. A resonant scanning dipole-antenna probe for enhanced nanoscale imaging. *Nano Lett.* **13,** 5070–5074 (2013).

79. Holtrup, F. O., Müller, G. R. J., Quante, H., De Feyter, S., De Schryver, F. C. & Müllen, K. Terrylenimides: new NIR fluorescent dyes. *Chem. - A Eur. J.* **3,** 219–225 (1997).

80. Mais, S, Tittel, J, Basche, T., Mu, G & Mu, K. Terrylenediimide: a novel fluorophore for single-molecule spectroscopy and microscopy from 1.4 K to room temperature. *J. Phys. Chem. A* **101,** 8435–8440 (1997).

81. Zayats, A. V. & Smolyaninov, I. I. Near-field photonics : surface plasmon polaritons and localized surface plasmons. *J. Opt. A Pure Appl. Opt.* **5,** S1–S35 (2003).

82. Ruiter, A. G., van der Werf, K. O., Veerman, J. A., Garcia-Parajo, M. F., Rensen, W. H. & van Hulst, N. F. Tuning fork shear-force feedback. *Ultramicroscopy* **71,** 149–157 (1998).

83. Esteban, R, Vogelgesang, R, Dorfmüller, J, Dmitriev, A, Rockstuhl, C, Etrich, C & Kern, K. Direct near-field optical imaging of higher order plasmonic resonances. *Nano Lett.* **8,** 3155–3159 (2008).

84. Schnell, M, Garcia-Etxarri, A & Huber, A. Controlling the near-field oscillations of loaded plasmonic nanoantennas. *Nat. Photonics* **3,** 287–291 (2009).

85. Schnell, M., Garcia-Etxarri, A., Huber, A. J., Crozier, K. B., Borisov, A., Aizpurua, J. & Hillenbrand, R. Amplitude- and Phase-Resolved Near-Field Mapping of Infrared Antenna Modes by Transmission-Mode Scattering-Type Near-Field Microscopy. *J. Phys. Chem. C* **114,** 7341–7345 (2010).

86. Coenen, T., Vesseur, E. J. R. & Polman, A. Deep subwavelength spatial characterization of angular emission from single-crystal Au plasmonic ridge nanoantennas. *ACS Nano* **6,** 1742–1750 (2012).

87. Nelayah, J., Kociak, M., Stéphan, O., García de Abajo, F. J., Tencé, M., Henrard, L., Taverna, D., Pastoriza-Santos, I., Liz-Marzán, L. M. & Colliex, C. Mapping surface plasmons on a single metallic nanoparticle. *Nat. Phys.* **3,** 348–353 (2007).

88. Sick, B, Hecht, B & Novotny, L. Orientational imaging of single molecules by annular illumination. *Phys. Rev. Lett.* **85,** 4482 (2000).

89. Novotny, L., Beversluis, M., Youngworth, K. & Brown, T. Longitudinal Field Modes Probed by Single Molecules. *Phys. Rev. Lett.* **86,** 5251 (2001).

90. Cuche, A, Drezet, A, Sonnefraud, Y, Faklaris, O, Treussart, F, Roch, J.-F. & Huant, S. Near-field optical microscopy with a nanodiamond-based single-photon tip. *Opt. Express* **17,** 19969–19980 (2009).

91. Beams, R., Smith, D., Johnson, T. W., Oh, S. H., Novotny, L. & Vamivakas, a. N. Nanoscale fluorescence lifetime imaging of an optical antenna with a single diamond NV center. *Nano Lett.* **13,** 3807–3811 (2013).

92. Krachmalnicoff, V., Cao, D., Cazé, A., Castanié, E., Pierrat, R., Bardou, N., Collin, S., Carminati, R. & De Wilde, Y. Towards a full characterization of a plasmonic nanostructure with a fluorescent near-field probe. *Opt. Express* **21,** 11536–11545 (2013).

93. Hecht, B., Bielefeldt, H., Novotny, L., Inouye, Y. & Pohl, D. Local Excitation, Scattering, and Interference of Surface Plasmons. *Phys. Rev. Lett.* **77,** 1889–1892 (1996).

94. Zia, R. & Brongersma, M. L. Surface plasmon polariton analogue to Young's double-slit experiment. *Nat. Nanotechnol.* **2,** 426–429 (2007).

95. Kramer, A., Trabesinger, W., Hecht, B. & Wild, U. P. Optical near-field enhancement at a metal tip probed by a single fluorophore. *Appl. Phys. Lett.* **80,** 1652–1654 (2002).

96. Protasenko, V. V. & Gallagher, A. C. Apertureless near-field scanning optical microscopy of single molecules. *Nano Lett.* **4,** 1329–1332 (2004).

97. Kühn, S. & Sandoghdar, V. Modification of single molecule fluorescence by a scanning probe. *Appl. Phys. B* **84,** 211–217 (2006).

98. Schnell, M, Garcia-Etxarri, A, Alkorta, J, Aizpurua, J & Hillenbrand, R. Phase-resolved mapping of the near-field vector and polarization state in nanoscale antenna gaps. *Nano Lett.* **10,** 3524–3528 (2010).

99. Singh, A, Calbris, G & van Hulst, N. F. Vectorial Nanoscale Mapping of Optical Antenna Fields by Single Molecule Dipoles. *Nano Lett.* **14,** 4715–4723 (2014).

100. Dorfmüller, J., Vogelgesang, R., Khunsin, W., Rockstuhl, C., Etrich, C. & Kern, K. Plasmonic nanowire antennas: experiment, simulation, and theory. *Nano Lett.* **10,** 3596–3603 (2010).

101. Rodríguez-Fortuño, F. J., Marino, G., Ginzburg, P., O'Connor, D., Martínez, A., Wurtz, G. A. & Zayats, A. V. Near-field interference for the unidirectional excitation of electromagnetic guided modes. *Science (80-.).* **340,** 328–330 (2013).

102. Le Feber, B., Rotenberg, N. & Kuipers, L. Nanophotonic control of circular dipole emission. *Nat. Commun.* **6,** 6695 (2015).

103. Ebbesen, T. W., Genet, C. & Bozhevolnyi, S. I. Surface-plasmon circuitry. *Phys. Today* **61,** 44–50 (2008).

104. Sorger, V. J., Oulton, R. F., Ma, R.-M. & Zhang, X. Toward integrated plasmonic circuits. *MRS Bull.* **37,** 728–738 (2012).

105. Yoshie, T., Tang, L. & Su, S.-Y. Optical Microcavity: Sensing down to Single Molecules and Atoms. *Sensors* **11,** 1972–1991 (2011).

106. Kimble, H. J. The quantum internet. *Nature* **453,** 1023–1030 (2008).

107. Scully, M. O. Quantum photocell: Using quantum coherence to reduce radiative recombination and increase efficiency. *Phys. Rev. Lett.* **104,** 207701 (2010).

108. Khitrova, G., Gibbs, H. M., Kira, M., Koch, S. W. & Scherer, a. Vacuum Rabi splitting in semiconductors. *Nat. Phys.* **2,** 81–90 (2006).

109. Yao, N. Y., Jiang, L., Gorshkov, A. V., Maurer, P. C., Giedke, G., Cirac, J. I. & Lukin, M. D. Scalable architecture for a room temperature solid-state quantum information processor. *Nat. Commun.* **3,** 800:1–8 (2012).

110. Cabrillo, C., Cirac, J. I., Garcia-Fernandez, P. & Zoller, P. Creation of entangled states of distant atoms by interference. *Phys. Rev. A* **59,** 10 (1998).

111. Delteil, A., Sun, Z., Gao, W.-b., Togan, E., Faelt, S. & Imamoglu, A. Generation of heralded entanglement between distant hole spins. *Nat. Phys.* **12,** 218–223 (2015).

112. Gao, W. B., Imamoglu, A., Bernien, H. & Hanson, R. Coherent manipulation, measurement and entanglement of individual solid-state spins using optical fields. *Nat. Photonics* **9,** 363–373 (2015).

113. Kok, P., Munro, W. J., Nemoto, K., Ralph, T. C., Dowling, J. P. & Milburn, G. J. Linear optical quantum computing with photonic qubits. *Rev. Mod. Phys.* **79,** 135–174 (2007).

114. Ding, X. *et al.* On-Demand Single Photons with High Extraction Efficiency and Near-Unity Indistinguishability from a Resonantly Driven Quantum Dot in a Micropillar. *Phys. Rev. Lett.* **116,** 020401 (2016).

115. Meystre, M. & P. Sargent. *Elements of quantum optics* 4th, 507 (Springer, 2007).

116. Yoshie, T, Scherer, A, Hendrickson, J, Khitrova, G, Gibbs, H. M., Rupper, G, Ell, C, Shchekin, O. B. & Deppe, D. G. Vacuum Rabi splitting with a single quantum dot in a photonic crystal nanocavity. *Nature* **432,** 200–203 (2004).

117. Hennessy, K., Badolato, A., Winger, M., Gerace, D., Atatüre, M., Gulde, S., Fält, S., Hu, E. L. & Imamoğlu, A. Quantum nature of a strongly coupled single quantum dot–cavity system. *Nature* **445,** 896–899 (2007).

118. Waks, E. & Sridharan, D. Cavity QED treatment of interactions between a metal nanoparticle and a dipole emitter. *Phys. Rev. A - At. Mol. Opt. Phys.* **82,** 043845 (2010).

119. Hümmer, T., García-Vidal, F. J., Martín-Moreno, L. & Zueco, D. Weak and strong coupling regimes in plasmonic QED. *Phys. Rev. B - Condens. Matter Mater. Phys.* **87,** 115419 (2013).

120. Ladd, T. D., Jelezko, F, Laflamme, R, Nakamura, Y, Monroe, C & O'Brien, J. L. Quantum computers. *Nature* **464,** 45–53 (2010).

121. Lounis, B., Bechtel, H., Gerion, D., Alivisatos, P. & Moerner, W. Photon antibunching in single CdSe/ZnS quantum dot fluorescence. *Chem. Phys. Lett.* **329,** 399–404 (2000).

122. Frimmer, M. & Koenderink, a. F. Spontaneous emission control in a tunable hybrid photonic system. *Phys. Rev. Lett.* **110,** 1–5 (2013).

123. Kreiter, M., Prummer, M., Hecht, B. & Wild, U. P. Orientation dependence of fluorescence lifetimes near an interface. *J. Chem. Phys.* **117,** 9430–9433 (2002).

124. Farahani, J. N., Pohl, D. W., Eisler, H.-J. & Hecht, B. Single Quantum Dot Coupled to a Scanning Optical Antenna: A Tunable Superemitter. *Phys. Rev. Lett.* **95,** 017402 (2005).

125. Schell, A. W., Engel, P., Werra, J. F. M., Wolff, C., Busch, K. & Benson, O. Scanning single quantum emitter fluorescence lifetime imaging: quantitative analysis of the local density of photonic States. *Nano Lett.* **14,** 2623–2627 (2014).

126. Cao, D., Cazé, A., Calabrese, M., Pierrat, R., Bardou, N., Collin, S., Carminati, R., Krachmalnicoff, V. & De Wilde, Y. Mapping the Radiative and the Apparent Nonradiative Local Density of States in the Near Field of a Metallic Nanoantenna. *ACS Photonics* **2,** 189–193 (2015).

127. Karaveli, S., Weinstein, A. J. & Zia, R. Direct modulation of lanthanide emission at sub-lifetime scales. *Nano Lett.* **13,** 2264–2269 (2013).

128. Barnes, W. Fluorescence near interfaces: the role of photonic mode density. *J. Mod. Opt.* **45,** 661–699 (1998).

129. Varnavski, O. P., Goodson, T., Mohamed, M. B. & El-Sayed, M. A. Femtosecond excitation dynamics in gold nanospheres and nanorods. *Phys. Rev. B - Condens. Matter Mater. Phys.* **72,** 235405 (2005).

130. P. Michler, A. Kiraz, C. Becher, W. V. Schoenfeld, P. M. Petroff, L. Zhang, E. Hu & A. Imamo\uglu. A quantum dot single photon turnstile device. *Science (80-.).* **290,** 2282–2285 (2000).

131. Pelton, M., Santori, C., Vucković, J., Zhang, B., Solomon, G. S., Plant, J. & Yamamoto, Y. Efficient Source of Single Photons: A Single Quantum Dot in a Micropost Microcavity. *Phys. Rev. Lett.* **89,** 233602 (2002).

132. Masuo, S., Naiki, H., Machida, S. & Itaya, A. Photon statistics in enhanced fluorescence from a single CdSe/ZnS quantum dot in the vicinity of silver nanoparticles. *Appl. Phys. Lett.* **95,** 193106 (2009).

ACKNOWLEDGEMENTS

Although on papers I will be the one who earns the PhD degree, in reality this would not have possible without the support and guidance of many people. First and foremost, I would like to sincerely thanks Niek for giving me the opportunity to work in his group, for his patience and motivation. As a supervisor he extended full support to do research in my own way, which in a way helped me a lot to think deeply about my work and learn to become independent on research. His passion for science and way of tackling problem always inspired me. I really appreciate the wonderful atmosphere he created in the group, encouraging us to discuss and collaborate on scientific issues. I am very fortunate to have him as my scientific Guru.

I am very grateful to Gaëtan for his consistent help from the beginning of my PhD. He was always there whenever I needed assistance in the lab with the setup and in the office discussing physics. He has always been very patient with me even after me asking same thing over and over. I troubled him a lot with my questions, lot of late night discussions, over skype several times even when we are out, and he never ever said no. If it weren't for him, my understanding about the subject would not have improved. Thanks a lot for your help and friendship.

I am very thankful to James, who taught me many things in the lab, the most important among them is never be afraid of taking things apart, best way to learn. I too bothered him a lot but he always tried to help me in a best way he can. His attitude of never afraid of trying new and different things always inspired me. He is an amazing person in many ways. I have really enjoyed his company and the good times we had outside of the work.

I have a special thanks to Pablo, a person with special skills and attitude. Thanks for all the help in the lab and ideas you brought to the table. His unconventional approach to problems is always been a great inspiration for me, I wish I had that in me.

Thanks Nicolò for being a good friend and always giving a helpful advice and more importantly taking us to good veggie places in Bcn. Thanks to Mathieu and Thomas for helping me out in the beginning of my PhD. I would like to thank all the present and past members of the MolNanoPhot family for making my life easy and enjoyable in and out of the work. Thanks to Ion, Lukasz, Klaas, Richard, Matz, Alex B, Vikas, Lisa, Nicola, Esther, Sylwester, Alex D, Lars, Jan, and Marta.

I would like to extend my gratitude to all units of ICFO from HR Manuela, Anne and colleagues for making our life easy at ICFO. Thanks to our director for creating such a wonderful and diverse place to do research. Thanks to Johann, Luis and Javier for taking care of all small and big problems in

the cleanroom. Thanks to Carlos, Arian, and Jonas for finding quick solution for maintenance and logistics issues.

A special thanks to the ever growing Indian community at ICFO with whom I shared a very special relationship. Thanks to Dhriti, Kavita, Chaitanya and Arup for amazing lunch session and discussions in the beginning. Many thanks to Ramaiah, first for being a wonderful flatmate, and bearing me all those years. You are a special friend. Thanks to Hari and Nitin to accompany me for all Indian food hunting trips to Barcelona. For all your encouragement and motivation. I really enjoyed my time with you guys.

Many thanks to Daniels and Pau for being very accommodating and wonderful flatmates. Claude and Andrea for being a fantastic company on weekends in Castelldefels. I greatly enjoyed my time with you guys and will always cherish and miss those moments. Thanks for your friendship.

Many many thanks to Janis, Pal and Karan for serving great food at odd times and even showing greater hospitality. I will cherish the wonderful time I had with you guys in Castelldefels and friendship for rest of my life.

I would like to mention my good friends from Jena: Kemal, Rosa, Nicole and Charan. Some very good friends from India: Mayank, Kuldeep, Tarun, Ayush, Ankit, and Annissa.

This acknowledgment would not be complete without mentioning a very special person and my best friend, Avichal. I can not describe his friendship in words and whatever I write would not be enough. So the least I can say thank you from the bottom of my heart.

Lastly, I would like to acknowledge my family and their consistent support and encouragement. My mother and father, my brother Rahulendra and sister Richa. This thesis is entirely dedicating to them. Getting the PhD is a dream for me and this dream becomes a reality only because of my family.